

**USGS Award Number G16AP00118**

**LIQUEFACTION PROBABILITY ANALYSIS OF PLEISTOCENE DEPOSITS  
IN THE GREATER CHARLESTON, SOUTH CAROLINA AREA**

**Final Technical Report to the  
United States Geological Survey**

**By:**

**Joshua D. Gathro, Barnabas Bwambale, and Ronald D. Andrus**

**Glenn Department of Civil Engineering  
Clemson University  
Lowry Hall, Box 340911  
Clemson, South Carolina 29634-0911 USA  
Telephone: (864) 656-0488  
Fax: (864) 656-2670  
E-mail: randrus@clemson.edu**

**May 1, 2016 – April 30, 2018**

This research was supported, in part, by the United States Geological Survey (USGS), Department of the Interior, under Grant No. G16AP00118, and the Aniket Shrikhande Memorial Graduate Assistantship. The views and conclusions contained in this document are those of the authors, and should not be interpreted as necessarily representing the opinions or policies, either expressed or implied, of the United States Government. Mention of trade names or commercial products does not constitute their endorsement by the U.S. Geological Survey.

**USGS Award Number G16AP00118**

**LIQUEFACTION PROBABILITY ANALYSIS OF PLEISTOCENE DEPOSITS  
IN THE GREATER CHARLESTON, SOUTH CAROLINA AREA**

**Final Technical Report to the United States Geological Survey by  
Joshua D. Gathro, Barnabas Bwambale, and Ronald D. Andrus**

**Glenn Department of Civil Engineering  
Clemson University  
Lowry Hall, Box 340911  
Clemson, South Carolina 29634-0911 USA  
Telephone: (864) 656-0488  
Fax: (864) 656-2670  
E-mail: randrus@clemson.edu**

**ABSTRACT**

This report investigates the liquefaction probability of six Quaternary sand deposits and five Quaternary clayey deposits within the greater Charleston, South Carolina area. The investigation is based on an analysis of seismic cone penetration test profiles for 228 sites in the sand deposits, and 90 sites in the clayey deposits. A review of major mapped ground failures and observed disturbances along rail lines following the 1886 Charleston earthquake ( $M_w \sim 7.0$ ) is also presented. Liquefaction susceptibility and liquefaction potential are expressed in terms of the liquefaction potential index ( $LPI$ ).  $LPI$  is used because 1) it offers a single value for a site, 2) it is one of the best single-value approaches currently available, and 3) it can be compared with results of other researchers. The effect of aging processes or diagenesis is considered through a correction factor ( $K_{DR}$ ) that is based on the ratio of measured shear-wave velocity ( $V_S$ ) to estimated  $V_S$ . Results of the liquefaction susceptibility assessment indicate there is little to no significant relationship between  $LPI$  and distance to the 1886 seismic source, or with distance to nearest perennial stream for the clayey deposits.

Liquefaction probability curves are expressed as functions of peak ground acceleration, earthquake magnitude, and probability that  $LPI$  is greater than or equal to a threshold value for surface manifestation of liquefaction at level ground sites. The results indicate that among the six sand deposits, the three youngest exhibit the highest probability for a given level of ground shaking. Likewise among the five clayey deposits, the youngest is shown to have the highest probability for a given earthquake load, while the four older clayey units display lower probabilities similar to each other. The liquefaction probability curves developed for all deposits generally agree well with the recorded observations of ground failure following the 1886 earthquake. Model probability curves are also generated for the clayey deposits assuming relevant combinations of depth to groundwater and depth to top of Cooper Marl. The liquefaction probability curves may be used to create regional hazard maps, but should not replace site-specific evaluations.

## ACKNOWLEDGMENTS

This research was supported by the United States Geological Survey (USGS), Department of the Interior under USGS Award No. G16AP00118, with Ronald D. Andrus as Principal Investigator. The support of the USGS is greatly appreciated. This research is based on field data compiled from research and consulting reports obtained for the greater Charleston area. The authors sincerely thank William Camp and Kyle Murrell of S&ME, Inc., Matthew Silveston and Jonathan Ard of Terracon Consultants, Michael Cox of Palmetto In-Situ, and Michael Hasek of WECTEC, LLC for their generous assistance with data collection. The authors also express gratitude to Thomas Holzer, Thomas Noce, and their colleagues of the USGS for sharing their field test data. Without the data contributed by these many individuals, the work contained in this report would remain impossible. The authors additionally thank Mahdiah Heidari for her initial research, which has paved the way for this work.

Acknowledgement is given to Edward West of the Summerville-Dorchester Museum for sharing documents on field observations following the 1886 Charleston earthquake. Chris Cramer of the University of Memphis provided estimates of peak horizontal ground acceleration for Qts sites. Finally, the authors express their gratitude to Eleanor L. Huggins and Kenneth T. Wicks who assisted Ronald Andrus with the latitude and longitude determination of ground deformation observations along the railroads, discussed in Chapters 2 and 3.

# TABLE OF CONTENTS

	Page
TITLE PAGE .....	i
ABSTRACT.....	iii
ACKNOWLEDGMENTS .....	iv
CHAPTER	
1. INTRODUCTION .....	1
1.1 Background .....	1
1.2 Objectives .....	2
1.3 Organization.....	3
2. LIQUEFACTION PROBABILITY OF SURFICIAL SAND UNITS IN THE CHARLESTON AREA .....	4
2.1 Introduction.....	4
2.2 Geology.....	4
2.3 1886 Earthquake and Ground Behavior.....	7
2.4 Seismic Cone Penetration Test Data.....	13
2.5 Measured to Estimated Shear Wave Velocity .....	17
2.6 Liquefaction Potential Index.....	18
2.7 Liquefaction Susceptibility Assessment .....	20
2.8 Liquefaction Probability Curves for Regional Hazard Mapping .....	26
2.9 Conclusion .....	29
3. LIQUEFACTION PROBABILITY OF SURFICIAL CLAYEY UNITS IN THE CHARLESTON AREA .....	30
3.1 Introduction.....	30
3.2 Geology.....	30
3.3 1886 Earthquake and Ground Behavior.....	33
3.4 Seismic Cone Penetration Test Data.....	38
3.5 Liquefaction Potential Index.....	39
3.6 Liquefaction Susceptibility Assessment .....	39
3.7 Liquefaction Probability Curves for Regional Hazard Mapping .....	48

## Table of Contents (Continued)

	Page
3.8 Conclusion .....	55
4. SUMMARY, CONCLUSIONS, AND RECOMMENDATIONS.....	56
4.1 Summary and Conclusions .....	56
4.1.1 Surficial Sand Deposits.....	56
4.1.2 Surficial Clayey Deposits .....	56
4.1.3 Relative Liquefaction Potential of Quaternary Deposits .....	57
4.2 Recommendations .....	50
REFERENCES .....	60
APPENDICES .....	68
A: Summary of SCPT Database for Sand and Clayey Units .....	69
B: Summary of Observations along Railroad Lines .....	77
C: Liquefaction Probability Curves for Model of Clayey Deposits .....	84
D: Summary of Shear Wave Velocity Data for Sand and Clayey Units .....	91
E: Liquefaction Characterization of a 200,000-year-old Beach Deposit near Charleston, South Carolina .....	114
F: Liquefaction Probability Curves for Three Surficial Sand Deposits near Charleston, South Carolina .....	136
G: Data Supplement .....	148

# CHAPTER ONE

## INTRODUCTION

### **1.1 Background**

On the night of August 31, 1886, the largest historic earthquake (moment magnitude,  $M_w$  ~7.0) to have occurred in the eastern United States struck near Charleston, South Carolina (Bollinger 1977). This seismic event caused 124 deaths, and damage to infrastructure and homes was equivalent to \$460 million (2006 dollars, Côté 2006). Ground shaking was felt over 800 miles away. Over 400 aftershocks occurred in the Charleston area within the 30 years that followed (Nuttli et al. 1986). Referring to the city of Charleston, Dutton (1889) reported that, “there was not a building in the city which had wholly escaped injury.”

Durá-Gómez and Talwani (2009) discussed original reports of the 1886 Charleston earthquake and recent studies to identify the locations of faults near Charleston. Despite the absence of a surface fault rupture, observations following the earthquake inferred a NE-SW trending fault zone in the areas of Woodstock, Middleton Place, and Rantowles (Dutton 1889). Since then, instrumentally recorded seismicity and additional modern efforts have led to the conclusion that the mainshock of the 1886 earthquake was likely from the Woodstock fault (Durá-Gómez and Talwani 2009). Durá-Gómez and Talwani (2009) characterize this fault as a right-lateral strike-slip fault oriented N30°E, dipping  $\geq 50^\circ$  northwest. The northern and southern segments of the Woodstock fault are separated at the surface by an antidualational compressional left step near Middleton Place, but converge at depth. Focal depths for seismic activity range between 3 and 12 km. Talwani and Schaeffer (2001) estimated a recurrence interval for earthquakes of similar magnitude as the 1886 event to be between 500 and 600 years in the Charleston area. As estimated by Wong et al. (2005), a repeat of the 1886 earthquake today could cause up to 900 deaths and have a debilitating economic impact to South Carolina of up to \$20 billion dollars. Thus, understanding and mitigating potential seismic hazards in the coastal region of South Carolina remains a high priority.

Seismic hazards include a number of earthquake-induced ground failures. Types of ground failures may include ground oscillation, lateral spreading, flow failure, and loss of bearing capacity. Liquefaction-induced ground failure was a significant portion of the damage that occurred within the Charleston area in 1886 (Dutton 1889). Liquefaction refers to the generation of excess pore-water pressure as soil structure collapses in response to cyclic loading from an earthquake. This increase in pore-water pressure decreases the effective stress within the soil, and leads to a subsequent loss of shear strength.

Liquefaction potential has traditionally been calculated using a stress-based approach proposed by Whitman (1971) and Seed and Idriss (1971). This procedure takes into account the earthquake loading acting on a soil mass, referred to as the cyclic stress ratio (*CSR*), as well as the ability of the soil to resist structure collapse and reduction in shear strength. The ability to resist structure collapse and reduction in shear strength is represented by a variable called the cyclic resistance ratio (*CRR*). The factor of safety against liquefaction triggering is defined as the ratio of *CRR* to *CSR*.

Due to the greater number of cases of liquefaction occurring in geologically young sediments or artificial fill (Robertson and Wride 1998; Youd et al. 2001), the methods for determining *CRR* are based on relationships derived from young soils. The effect of aging on the liquefaction resistance of older soils remains a topic of current research (Leon et al. 2006; Hayati and Andrus 2009; Kiyota et al. 2009; Kokusho et al. 2012; Amoly et al. 2015; Bwambale et al. 2017; Bwambale and Andrus 2018). Aging or diagenetic processes tend to have the effect of greater resistance to liquefaction over time. Difficulty in capturing this increase in *CRR* is due in part to the fact that diagenesis affects mainly the small- to medium-strain dynamic properties of soil, soil penetration resistance is often measured by in-situ field tests that induce large strains, and liquefaction is a medium- to large-strain event.

Small-strain shear wave velocity ( $V_s$ ) is related to the small-strain modulus by  $G_{max} = \rho V_s^2$ , where  $\rho$  is the mass density of the soil. Because  $V_s$  is more sensitive to the effects of diagenesis than penetration resistance, Andrus et al. (2009) suggested that a ratio of measured  $V_s$  to estimated  $V_s$  be used to quantify the effect of diagenesis on soil resistance. This ratio is known as *MEVR*, and can be used as the predictor variable for the *CRR* adjustment factor  $K_{DR}$ . The use of *MEVR* within the liquefaction triggering procedure has been shown by multiple investigations to be a more robust predictor of degree of diagenesis and its effects on *CRR* than age (Hayati and Andrus 2009; Heidari and Andrus 2010; Bwambale and Andrus 2018).

This study builds on the work of many researchers who have previously conducted efforts to map liquefaction potential in the Charleston region (Elton and Hady-Hamou 1990; Balon and Andrus 2006; Juang and Li 2007; Hayati and Andrus 2008a; Heidari 2011; Heidari and Andrus 2010, 2012; Simonson 2012). With an expanded database of 318 seismic cone penetration test (SCPT) profiles, the uncertainty associated with liquefaction probabilities calculated in previous studies is reduced in this study. In addition, the results of the SCPT analyses are compared with observations of ground failures following the 1886 earthquake in an effort to validate findings.

The outcomes of this report may be used to develop liquefaction probability hazard maps. Liquefaction potential maps are a useful tool for engineers, scientists, and planners, but should not replace site-specific liquefaction hazard assessments (Franke et al. 2016).

## **1.2 Objectives**

The main purpose behind this work is to quantify the probability of liquefaction occurrence within several aged, surficial soil deposits present in the greater Charleston area. This purpose is accomplished upon addressing the specific objectives given below:

1. Compile an expanded database of several hundred SCPT profiles for the greater Charleston area, including sufficient metadata.
2. Apply procedures for calculating liquefaction potential index (*LPI*) to the updated SCPT database in order to assess liquefaction susceptibility of major surface geologic units.
3. Develop updated liquefaction probability curves for major surface geologies in the Charleston region based on the expanded SCPT database.
4. Compare results from the liquefaction susceptibility assessment and the liquefaction potential analysis with ground behavior observations following the 1886 Charleston earthquake.



The results of this work may be of significant use in developing quality, updated liquefaction hazard maps of the greater Charleston area. This study may also improve the accuracy of site-specific liquefaction hazard evaluations in Charleston. For regions in the U.S. with common intraplate seismicity, the results and procedures may also be used to improve liquefaction evaluations in aged soils and paleoliquefaction characterization efforts.

### **1.3 Organization**

This report is organized into four separate chapters. The current chapter, Chapter 1, provides relevant background information on the topics of soil liquefaction and Charleston geology and seismology. Chapter 2 presents the research approach and findings for the liquefaction susceptibility and probability of surficial sand deposits within the Charleston region. Chapter 3 continues the study of liquefaction susceptibility and probability as applied to clayey soil deposits in the region. This chapter also furthers the investigation by providing probability curves generated as a function of depth to groundwater and depth to Cooper Marl. Both Chapters 2 and 3 also present a discussion of ground behavior within the major surficial geologic units following the 1886 earthquake. Chapter 4 concludes this report by summarizing the work contained herein and offering recommendations for future study.

The body of this report and select appendices represent a modified version of the master's thesis produced by Gathro (2018). Appendix E is taken from Chapter 6 of the PhD dissertation by Bwambale (2018). A publication stemming from early results of this work is included in Appendix F (Gathro et al. 2018).

## CHAPTER TWO

### LIQUEFACTION PROBABILITY OF SURFICIAL SAND UNITS IN THE CHARLESTON AREA<sup>1</sup>

#### 2.1 Introduction

The liquefaction probability of six surficial sand deposits in the greater Charleston area is characterized in this chapter. The characterization begins with a discussion of their ground behavior following the 1886 Charleston earthquake. Next, an overview of procedures and issues surrounding the analysis of downhole seismic data is provided, as it applies to this study. Liquefaction susceptibility is then assessed, with consideration for geologic age and distance to inferred Woodstock fault zone. Finally, liquefaction probability curves are developed, assuming various earthquake loading conditions.

A map of the Charleston area is presented in Figure 2.1. Included on the map are: 1) the likely source of the 1886 earthquake (Woodstock fault zone), 2) spatial distributions of seven Quaternary beach to barrier-island sand deposits, 3) locations of selected 1886 earthquake observed ground behavior in four surficial sand deposits, and 4) locations of 228 seismic cone penetration tests (designated as SCPT, or as SCPTu if pore pressure measurements were made) conducted in six sand deposits. This database contains over three times the number of SCPT's/SCPTu's that Heidari and Andrus (2012) used to characterize the liquefaction probability of the five youngest sand units. The purpose of this work is to update and reduce the uncertainty of the liquefaction probability curves for the six deposits using the expanded database.

#### 2.2 Geology

The Charleston area lies within the lower Coastal Plain physiographic province. Thick Quaternary sediments atop older, Neogene to Paleogene (2.6–66 Ma) stratigraphic units generally blanket the region (Cooke 1936; Weems et al. 2014). These Quaternary deposits formed as a result of sea level transgressions during interglacial periods. Within each Pleistocene formation, three distinct facies have been identified which correspond to fluvial-estuary-backbarrier, barrier-island, and open-marine shelf depositional environments (Weems and Lemon 1988). A dominant Paleogene unit in the subsurface is the Ashley Formation of the Cooper Group, a phosphatic and quartzose calcarenite locally known as the Cooper Marl. The Cooper Marl is generally considered nonsusceptible to liquefaction (Li et al. 2007; Hayati and Andrus 2008b). The unconsolidated sedimentary sequences rest on crystalline basement rock, known to be ~800 m below ground surface (Chapman and Talwani 2002).

---

<sup>1</sup>Part of this chapter has been published in the proceedings of the 5<sup>th</sup> *Geotechnical Earthquake Engineering and Soil Dynamics Conference* and is reproduced for this report in Appendix F; Gathro, J. D., Bwambale, B., Andrus, R. D., Heidari, T. (2018). "Liquefaction probability curves for three surficial sand deposits near Charleston, South Carolina."

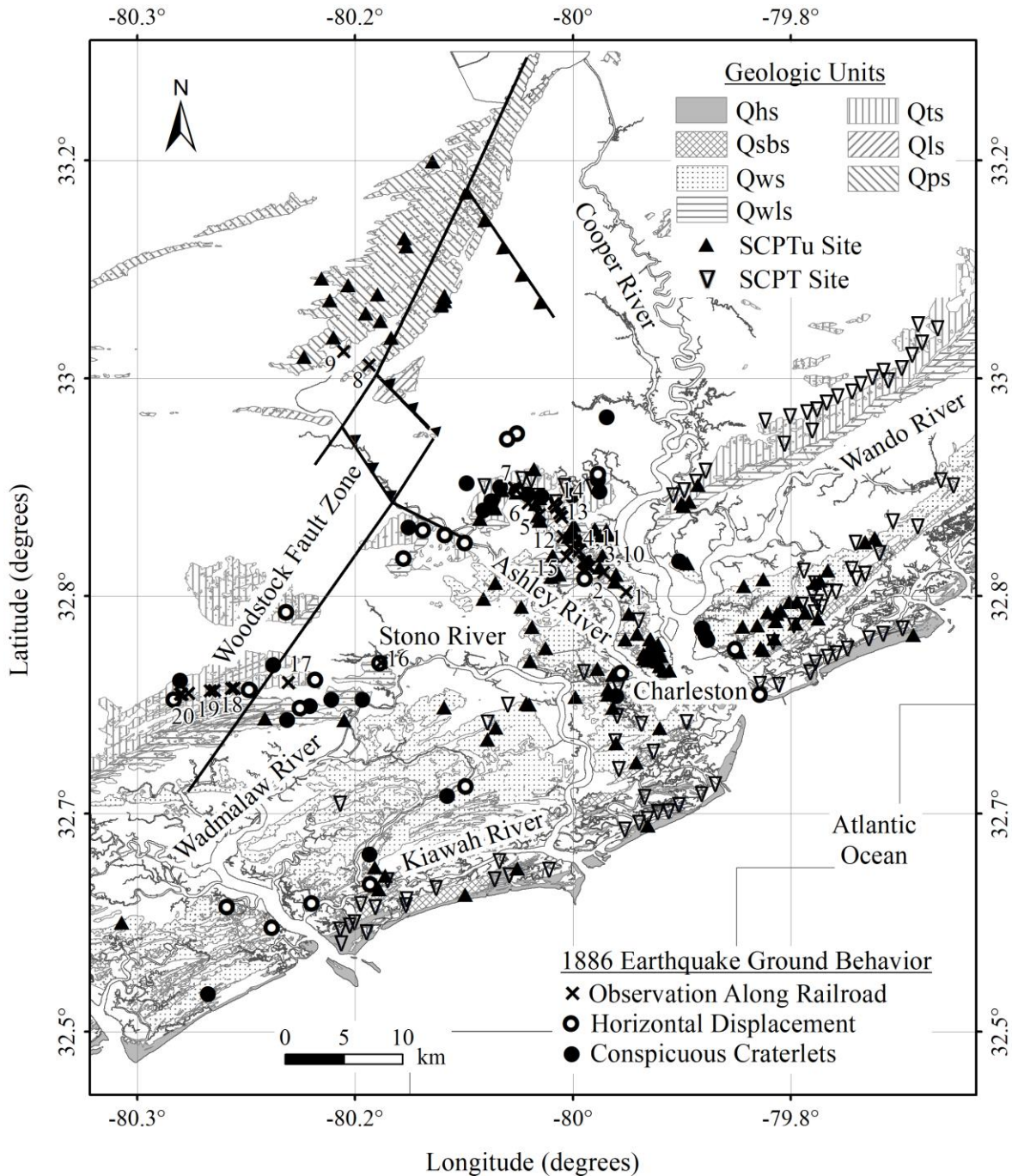


Figure 2.1 Geologic map of the Charleston area showing surficial sand deposits (modified from Heidari and Andrus 2012; Weems et al. 2014), the Woodstock fault zone (Durá-Gómez and Talwani 2009), seismic cone penetration test sites within Qhs, Qsbs, Qws, Qwls, Qts, and Qps, and mapped sites of ground failures within these units (Dutton 1889, PLs. XXVII & XXVIII; Peters and Hermann 1986).

The six natural sand deposits considered in this study are Qhs, Qsbs, Qws, Qwls, Qts, and Qps. Qhs is a deposit of Holocene (< 10 ka) beach to barrier-island quartz sand, located in the low-lying region parallel to the coast. Qsbs (33–85 ka) is a beach to barrier-island quartz sand known as the Silver Bluff terrace, often deposited adjacent to Qws. Qws and Qwls (70–130 ka) are barrier-island quartz sand facies of the Wando Formation, Qws being younger than Qwls and a dominant surface unit on the Charleston peninsula. Qts (200–240 ka) is a barrier-island quartz sand from the Ten Mile Hill Formation located farther inland and parallel to the coast. Qps (730–970 ka) is a barrier-island quartz sand of the Penholoway Formation. A large region of Qps is located in an area surrounding the northern half of the Woodstock fault zone. Due to sequences of sea level transgression and regression, the older deposits are generally located farther from the coast and at higher elevations than each successively younger unit.

Table 2.1 presents the average values of reported depths to groundwater table at SCPT/SCPTu sites for each of the six units. SCPT data reported by the USGS included no water table measurements. For these sites, an average water table depth from the other SCPT/SCPTu profiles within the unit was determined, and applied to these profiles during the *LPI* analyses. Though depth values were reported for all other sites, limitations of the water table values may include: different times during the year at which the measurement was made and following testing, different methods of determining depth to water (electric sounder, tape measure with or without chalk, etc.), and the possibility of cone hole cave-ins that mask the true depth to water.

Also included is the approximate range of depth below ground surface at which the Cooper Marl may be encountered. The depth ranges for the Cooper Marl are based on data presented in the geologic maps by Weems and Lemon (1993) and Weems et al. (1997), which generally agree well with profiles interpreted from the SCPT/SCPTu database and depths reported in consulting reports.

Table 2.1 Average depths below ground surface to the groundwater table and the Cooper Marl for six surficial sand deposits.

Surface Geology	Average Depth to Water Table (m)	Approximate Range of Depths to Cooper Marl (m)
Qhs	1.80	14 to 24
Qsbs	1.53	9 to 26
Qws	1.69	8 to 29
Qwls	1.97	7 to 30
Qts	2.20	6 to 32
Qps	1.26	9 to 16

### **2.3 1886 Earthquake and Ground Behavior**

Dutton (1889) reported several cases of ground failure that occurred during the 1886 earthquake, including 113 cases of horizontal ground displacement and 55 cases of conspicuous craterlets. Heidari (2011) estimated coordinates for these sites and noted that these areas include only major occurrences mapped by Earle Sloan. However, additional cases of lesser severity occurred at many other locations throughout the region (Hayati and Andrus 2008a; Heidari and Andrus 2010).

Within Qhs, Qsbs, Qws, Qwls, Qts, and Qps, the number of mapped occurrences of horizontal ground displacement in the Dutton (1889) report are 1, 7, 3, 4, 9, and 0, respectively; and the number of mapped areas of conspicuous craterlets were 0, 5, 2, 4, 14, and 0, respectively. Due to limited information regarding the exact location of these ground failures in Dutton (1889) and limitations of geologic maps, it is possible that some of these mapped failures actually occurred in adjacent units, despite careful efforts by Heidari (2011) to determine accurate coordinates. Sloping ground and the presence of other underlying units in the shallow subsurface may have also affected these observed ground behaviors. Yet these observations generally agree with the newspaper and other accounts compiled by Hayati and Andrus (2008a) from the peninsula of Charleston and by Heidari and Andrus (2010) from Mount Pleasant (located east of the peninsula), as well as the field notes by Earle Sloan and W. J. McGee along the railway lines summarized in Appendix B and Table 2.2.

Assuming that the detailed field notes by Sloan and McGee accurately describe all significant ground behavior (see Table 2.2), about 6.4% of the area along the railway lines through Qws experienced moderate to severe surface manifestations of liquefaction, 1.6% experienced minor manifestations, and 92% experienced none. For Qwls, approximately 3% of the total railway line distance within the unit experienced moderate to severe surface manifestations of liquefaction, 15% experienced minor surface manifestations, and the remaining 82% exhibited no surface evidence of liquefaction. Approximately 9 – 11% of the area covered by Qts along the railway lines experienced moderate to severe surface manifestations of liquefaction, 5 – 8% experienced minor, and 83 – 84% did not show any. For the distance of the railway lines through Qps, about 7% experienced moderate to severe surface manifestations of liquefaction, 7% experienced minor, and 86% experienced none. Areas within a radius of 80 meters (0.05 mile) from observed craterlets were classified as moderate to severe liquefaction. Areas were classified as minor liquefaction if fissures and depressions were present within a radius of 80 meters, and no liquefaction if there were no observed disturbances or craterlets along the railway lines. The field notes by Sloan and McGee summarized in Appendix B did not include any observations of surface manifestations of liquefaction within Qhs and Qsbs.

Table 2.2 Disturbances along railroads in Qws, Qwls, Qts, and Qps during the 1886 Charleston earthquake (adapted from field notes by Earle Sloan and W. J. McGee as cited by Dutton [1889, pp. 283-294, 303-306] and Peters and Hermann [1986, pp. 18-26, 51-55, 62-64]).

Site No.	Surface Geology	Mile Point	Latitude (degrees)	Longitude (degrees)	Elev. (m)	Description of Disturbance
South Carolina Railroad						
1	Qws	3.57	32.835994	-79.959171	4.42	Curve disturbed, several joints well opened; occasional craterlets to mile point 5.0
2	Qwls	5.0	32.851180	-79.976307	8.23	Fish-plate bolts sheared; 180 mm opening at joints on both sides; sand discharged around well
3	Qwls	5.85	32.856491	-79.989125	5.79	Joints strained open
		6.0	32.858214	-79.990685	5.33	Roadbed depressed 150 mm under short chord
		6.09	32.859506	-79.991907	5.23	Joints strained open; occasional slight depressions and transverse flexures to mile point 9.0
4	Qwls	7.0	32.869792	-80.001806	---	Seven Mile Station – fissures less common
5	Qts	9.23	32.895391	-80.025498	6.02	Kink in track; train derailed and wrecked to the east; craterlets increasing in size and number
6	Qts	10.0	32.904402	-80.033925	7.62	Superstructure jammed to the south; craterlets reach greatest development both in size and number
7	Qts	10.85	32.914101	-80.043026	6.05	Track severely distorted to the southeast
		11.01	32.915894	-80.044700	5.81	Roadbed depressed 460 mm under 18 m chord
		11.02	32.915990	-80.044793	5.82	180 mm gap at joint; craterlets
8	Qps	20.3	33.009953	-80.155869	---	Lincolntonville – “no fissures or craterlets”
9	Qps	21.47	33.019379	-80.173260	10.90	Track strained laterally and vertically
		21.61	33.020473	-80.175328	11.51	Summerville station – no disturbance to track; craterlets common in town and fields

Table 2.2 Continued.

Site No.	Surface Geology	Mile Point	Latitude (degrees)	Longitude (degrees)	Elev. (m)	Description of Disturbance
Northeastern Railroad						
10	Qwls	6.0	32.855197	-79.987178	---	Road depressed 560 mm under 120 m chord
		6.38	32.859903	-79.990394	---	Fish-plate bolts sheared; 360 mm opening of joints on both sides of track
11	Qws	7.0	32.867467	-79.995443	---	Slight depression within short space over culvert
		7.02	32.867750	-79.995464	7.62	Slight sinuous flexure
12	Qwls	7.85	32.878858	-80.007619	---	Slight sinuous flexure
13	Qts	8.97	32.893700	-80.008483	---	Superstructure shifted 100 mm to the east
		9.0	32.894086	-80.008689	---	Long flexure with 100 mm ordinate to the east
		9.19	32.896686	-80.010039	13.72	Borrow pit excavation 1.8 m deep with many craterlets; water/sand ejected to heights of 4 m
14	Qts	9.51	32.900867	-80.012331	---	Fish-plates broken; rails parted 220 mm
		9.57	32.901694	-80.012775	---	Sliding frog (switch) sheared and shifted 200 mm to the south; craterlets abundant
		9.76	32.904114	-80.014075	4.57	Superstructure deflected to the east
Charleston and Savannah Railroad						
15	Qwls	7.1	32.86308	-80.004900	---	Junction of the Charleston and Savannah Railroads; fissures less common
	Qwls	---	---	---	---	Occasional and slight transverse displacements between mile point 7.1 and the Ashley River
16	Qwls	18.57	32.782067	-80.146675	4.34	Roadbed displaced vertically and laterally to south; displacement to the south increasing; craterlets reappeared
17	Qts	22.7	32.766956	-80.217870	---	End of continuous sinuous flexures; higher and firmer ground
18	Qts	25.0	32.762518	-80.259181	---	North of track 460 m, a 600-m-long fissure occurred with series of craterlets trending S80°W
		25.11	32.762317	-80.261237	---	Road depressed 150 mm
19	Qts	25.85	32.760746	-80.274371	---	Road depressed 460 mm over 90 m length
		26.02	32.760491	-80.277544	---	Slight sinuous flexures
20	Qts	26.95	32.758675	-80.294186	---	Road undermined by craterlet (2.4 m x 1.8 m and 3 m deep); adjacent ditches blocked with expelled sand from craterlets
		27.23	32.758123	-80.299309	---	Slight strain southward
		27.28	32.758095	-80.300259	---	Slight depression of 100 mm
		---	---	---	---	Disturbances were rare between mile points 27.57 and 28.71

Figures 2.2 through 2.7 are histograms that present the relationship between inferred distance to Woodstock fault ( $d_f$ ) and the occurrence of ground failures reported by Dutton (1889) for each sand unit investigated in this study. Also included in these figures are data for the railroad disturbances presented in Table 2.2 above. As noted in Table 2.2, no observations of disturbances in Qhs and Qsbs were recorded in the field notes of Sloan and McGee. The distance to fault has been measured to the fault segments trending NE-SW, or to a linear projection of these segments. In each case, the occurrence of ground failures along the railroad and otherwise is well within the spatial extent of each deposit with respect to distance to fault. These figures indicate that surface evidence of liquefaction is constrained within certain distances from the Woodstock fault. Also evident is the relative number of occurrences of major craterlets and ground displacements in these units, as reported by Dutton (1889). As mentioned previously, these occurrences may actually have been located in adjacent units, or influenced by other soil types in the subsurface.

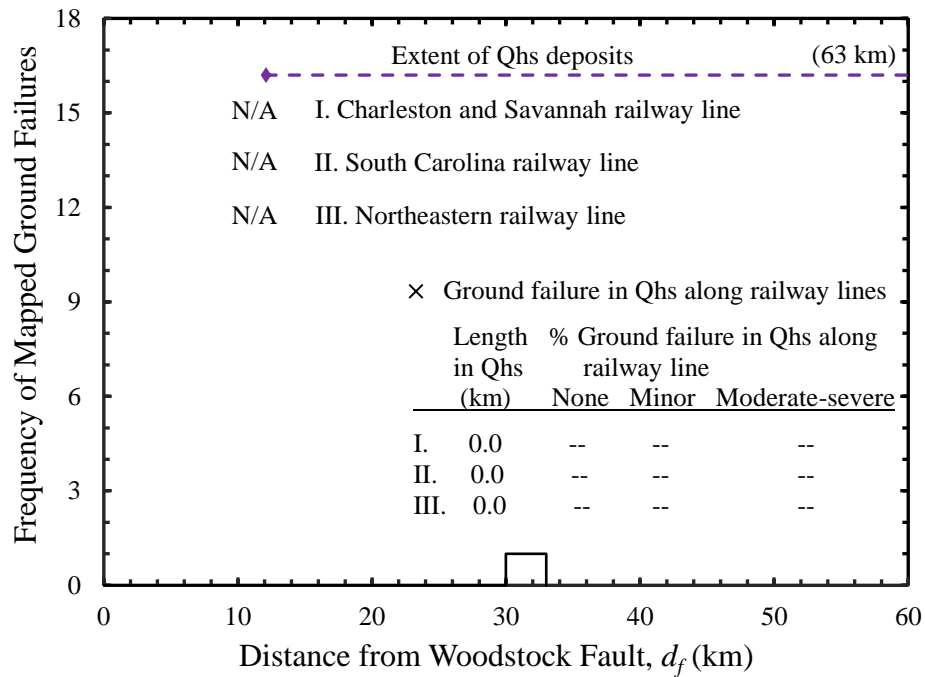


Figure 2.2. Histogram of ground failures reported by Dutton (1889) within Qhs and railroad observation data from field notes of Sloan and McGee.



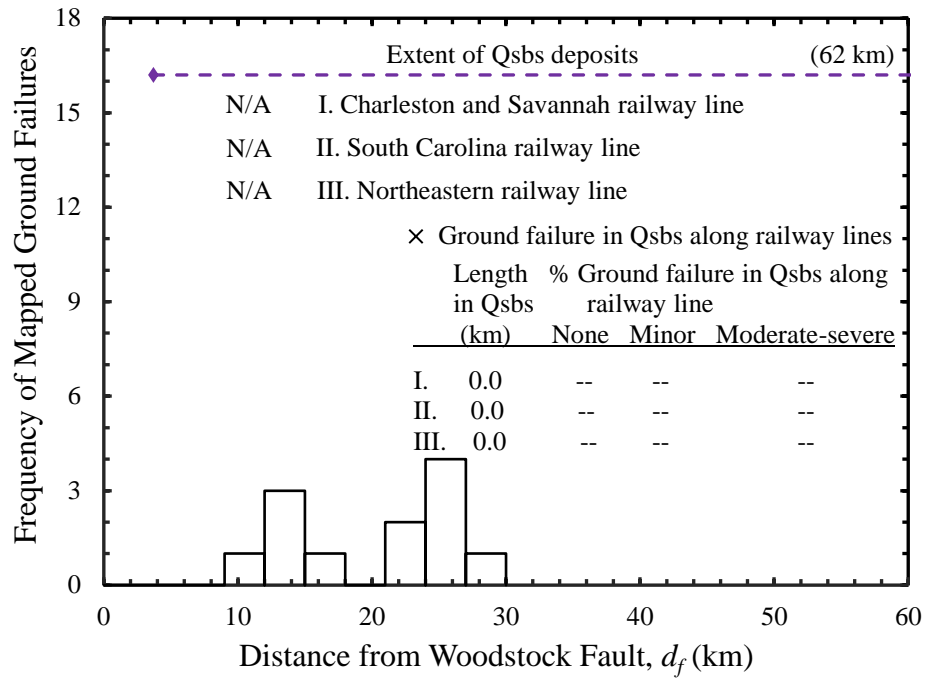


Figure 2.3. Histogram of ground failures reported by Dutton (1889) within Qsbs and railroad observation data from field notes of Sloan and McGee.

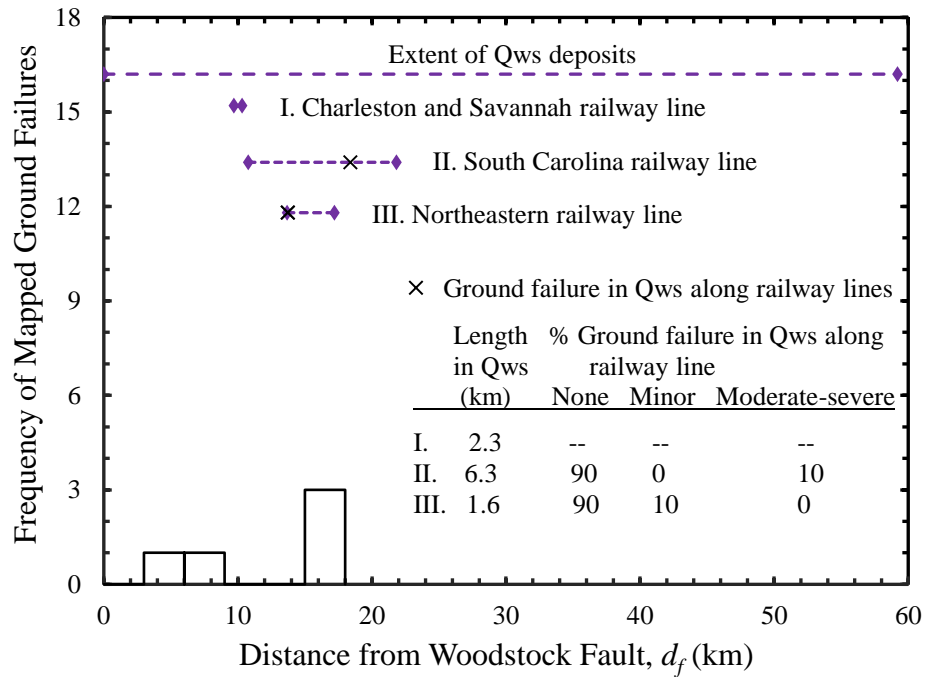


Figure 2.4. Histogram of ground failures reported by Dutton (1889) within Qws and railroad observation data from field notes of Sloan and McGee.

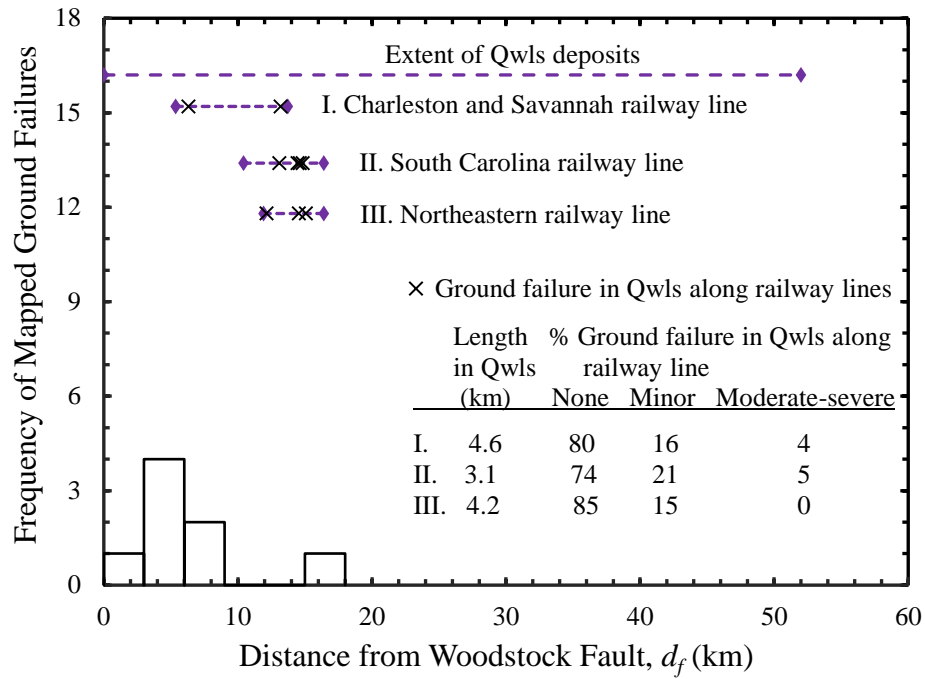


Figure 2.5. Histogram of ground failures reported by Dutton (1889) within Qwls and railroad observation data from field notes of Sloan and McGee.

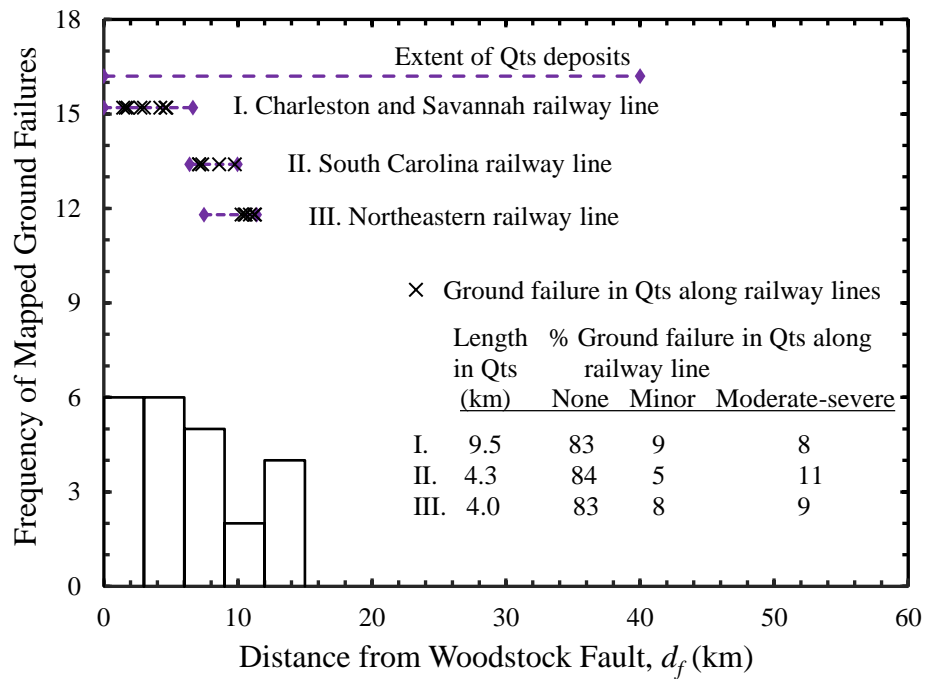


Figure 2.6. Histogram of ground failures reported by Dutton (1889) within Qts and railroad observation data from field notes of Sloan and McGee.

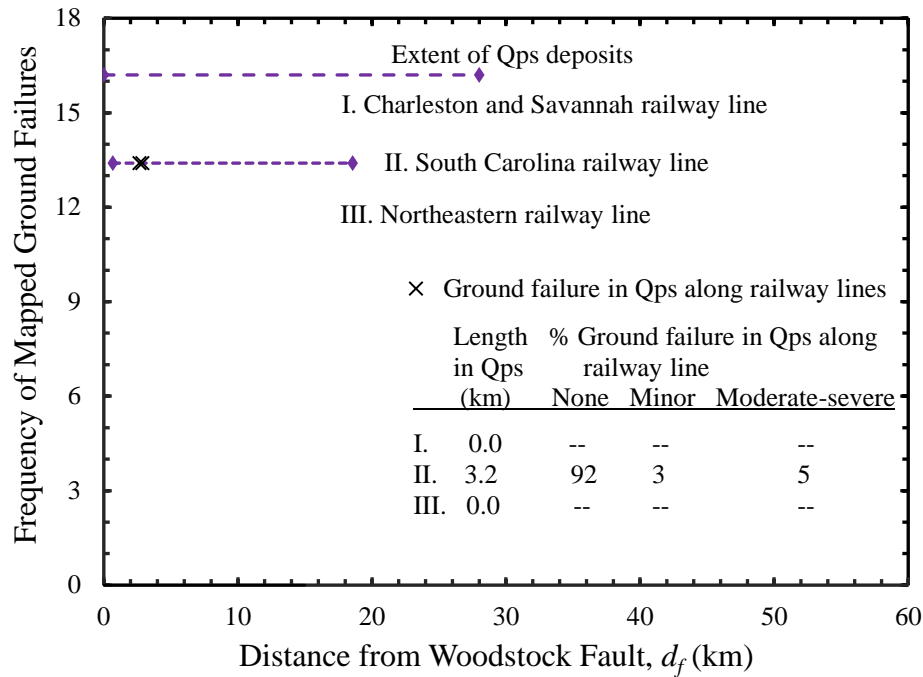


Figure 2.7. Histogram of ground failures reported by Dutton (1889) within Qps and railroad observation data from field notes of Sloan and McGee.

## 2.4 Seismic Cone Penetration Test Data

A compilation of 96 SCPT and 132 SCPTu profiles for the surficial sand deposits has been gathered from various available research and consulting reports. Table A-1 provides a summary of these sites, including references to identify source project. Of the 228 profiles, 33 plot in Qhs, 24 in Qsbs, 91 in Qws, 16 in Qwls, 47 in Qts, and 17 in Qps. Seventy of the sites are from the database compiled by Mohanan et al. (2006), as indicated in Table A-1. Heidari (2011) analyzed many of these sites, as well as an additional 9, which have likewise been included in this database. Heidari (2011) stated that the coordinate accuracy associated with these 79 SCPTu profiles is believed to be within 100 m. Of the remaining 149 profiles, 36 are from project reports by S&ME (2005-2013), 15 are from projects by Terracon (2013-2016), and 95 SCPT are from the U. S. Geological Survey online database compiled by Thomas Holzer and his colleagues ([earthquake.usgs.gov/research/cpt/data/charleston/](http://earthquake.usgs.gov/research/cpt/data/charleston/)). Three of the 149 sites are from the study by Hasek (2016), conducted at a test location near Hollywood, SC. Coordinates for the 149 sites were obtained either directly from the project data files, or by identifying the site address from the report and pinpointing the cone hole location in Google Earth Pro software based on the site layout map. The location accuracy of the latter profiles is believed to be within 60 m.

Displayed in Figure 2.8 is an example SCPTu profile for the site designated as Qws85, located on the Charleston Peninsula. The tip resistance ( $q_t$ ), friction ratio ( $FR$ ), and pore water pressure ( $u_2$ ) measurements are shown in Figures 2.8a, 2.8b and 2.8c, respectively. These measurements help distinguish soil behavior type. Typical behavior for sand-like soil includes high  $q_t$  and low  $FR$ , with  $u_2$  approximately equal to the hydrostatic pressure ( $u_0$ ). Clay-like soil

alternatively exhibits low  $q_t$  and high  $FR$ , with increased values of excess  $u_2$  as a result of soil remolding and undrained conditions. The increase in small-strain shear-wave velocity ( $V_s$ ) to over 300 m/s below 17 m in Figure 2.8d is typical of the Cooper Marl. The fairly uniform profiles of  $q_t$ , and  $FR$ , and  $u_2 > 1$  MPa are also typical of the Cooper Marl. The inferred geologic profile in Figure 2.8f is based on the SCPTu profile and information available on the USGS Charleston quadrangle geologic map by Weems and Lemon (1993). Figure 2.8e shows the variation with depth of  $MEVR$ , which will be discussed later in this chapter.

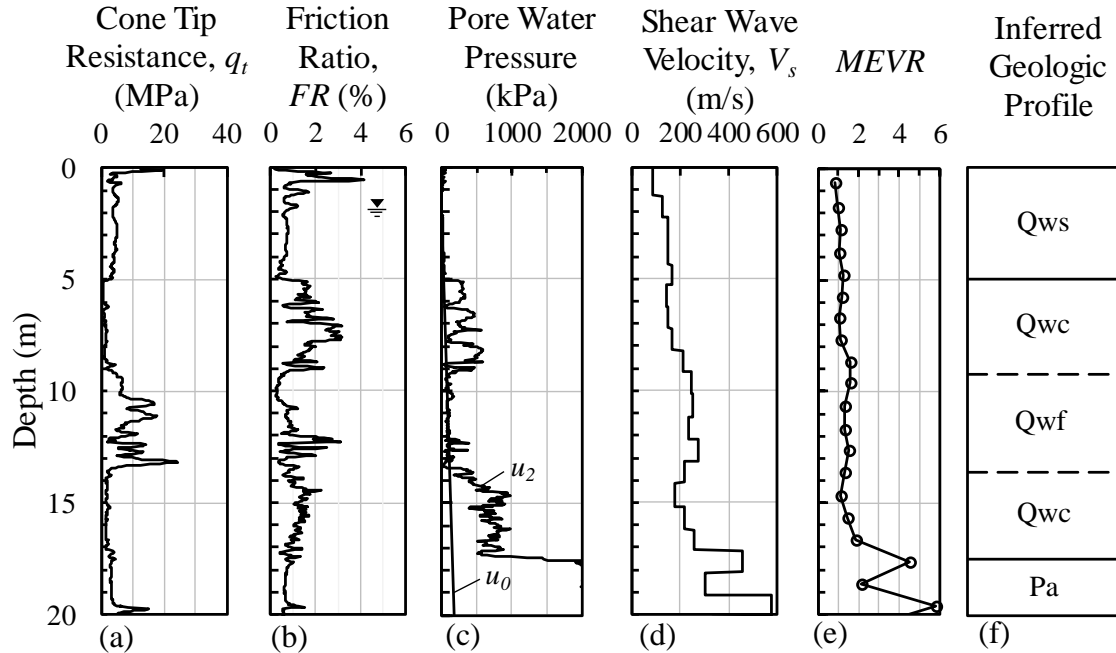


Figure 2.8 SCPTu profile and inferred geologic profile for site Qws85. The abbreviated geologic units given in the profile are (Weems et al. 2014): Qws, a barrier-island quartz sand facies of the Wando Formation (70–130 ka); Qwc, a clayey sand and clay facies of the Wando Formation; Qwf, a fossiliferous shelf-sand facies of the Wando Formation; and Pa, the Ashley Formation (lower Oligocene, about 29 Ma), known locally as the Cooper Marl.

Downhole seismic cone data are often evaluated by conventional means of the direct method and/or interval method (Kramer 1996; Martin and Mayne 1997; Kim et al. 2004). The direct method involves correcting the measured travel time in the inclined path to a travel time in the vertical path. Each corrected travel time is then plotted versus depth, and the average wave velocity is equal to the slope of a line fitted to points with a similar trend. The interval method involves measuring the travel times of waves from the source to two receivers located at different known depths and calculating wave velocities based on these times and inclined travel paths. In using the direct and interval methods, it is most common to assume that the wave path follows a straight line from source to receiver. While the assumption of straight ray path simplifies the calculation, it overlooks the effects of refraction at soil layer boundaries with contrasts in soil

stiffness, which may yield a measured  $V_s$  higher or lower than the true  $V_s$ . This issue is of greatest concern near the ground surface, where the assumed straight ray path may vary significantly from the true path, depending on the magnitude of horizontal source-to-hole offset, measurement depth interval, and variation in soil stiffness.

The downhole  $V_s$  data utilized in this study were originally analyzed using the pseudo interval or direct interval method, and have been re-evaluated by means of the Snell's Law ray path method (Kim et al. 2004) where complete metadata were accessible. For sites with insufficient metadata (< 16% of the sites),  $V_s$  values were used as provided in the geotechnical reports. The pseudo interval method involves the use of only one receiver, and the travel times are obtained by pushing the receiver to the different desired depths and hitting the seismic source twice (once at each location). Another form of the interval method is the true interval, in which two receivers are used and a single seismic source is generated. Thus, in a true interval, both receivers respond to the same seismic energy. In each case of the interval method, the wave velocity of the depth interval is computed by dividing the difference between the two inclined travel path distances by the difference in travel times. In this analysis of sand deposits, three SCPTu locations (Qlws14, Qlws15, and Qlws16) were conducted such that  $V_s$  measurements were obtained by means of the true interval method. While the true interval method improves the  $V_s$  measurement for a given depth interval, successive depth intervals often overlap, providing varying travel times. This variation in depths and travel times along the profile precludes the use of the Snell's Law ray path method. Therefore, these data were re-evaluated following the modified interval method in order to provide an improved estimate of shear wave velocity.

The modified interval method and the Snell's Law ray path method (Kim et al. 2004) both help improve the measured  $V_s$  from downhole data, the latter being most reliable. The limitation remaining with the modified interval method is the fact that a straight ray path is still assumed. However, the modified interval takes into account the wave travel distance within each layer along the straight path, based on the actual thickness of the layer. The modified travel distances are then used to calculate shear wave velocity for each successive layer. Specific equations to be used in this procedure are presented by Kim et al. (2004). A reduced form of these equations was developed as part of this study by Ronald Andrus, considering a two-layer system. This equation is given as:

$$V_{s2} = \frac{d_2 \cdot \left(1 - \frac{z_1}{z_2}\right)}{t_2 - \left[t_1 \cdot \left(\frac{z_1}{z_2}\right) \cdot \left(\frac{d_2}{d_1}\right)\right]} \quad (2.1)$$

where  $V_{s2}$  = shear wave velocity of second layer;  $z_1$  and  $z_2$  = vertical depth below ground surface to receiver at the top and at the base of second layer, respectively;  $t_1$  and  $t_2$  = wave travel times recorded by receiver above and below second layer, respectively;  $d_1$  and  $d_2$  = inclined distance between seismic source and receiver above and below second layer, respectively. The results provided by Equation 2.1 have been shown to offer much-improved velocity estimates, even when assuming a top layer comprised of multiple measurement intervals, resting above what has been termed the "second layer."

The Snell's Law ray path method involves an iterative process wherein the wave travel path and velocity for each successive measurement interval are computed based on refraction at each layer boundary, as shown in Figure 2.9. The primary criteria that must be satisfied in this method include Snell's Law and trigonometric relationships. Iterations for each layer are continued until the initial assumed velocity and the calculated velocity converge. Kim et al. (2004) discuss other details regarding this procedure and a comparison of analysis methods.

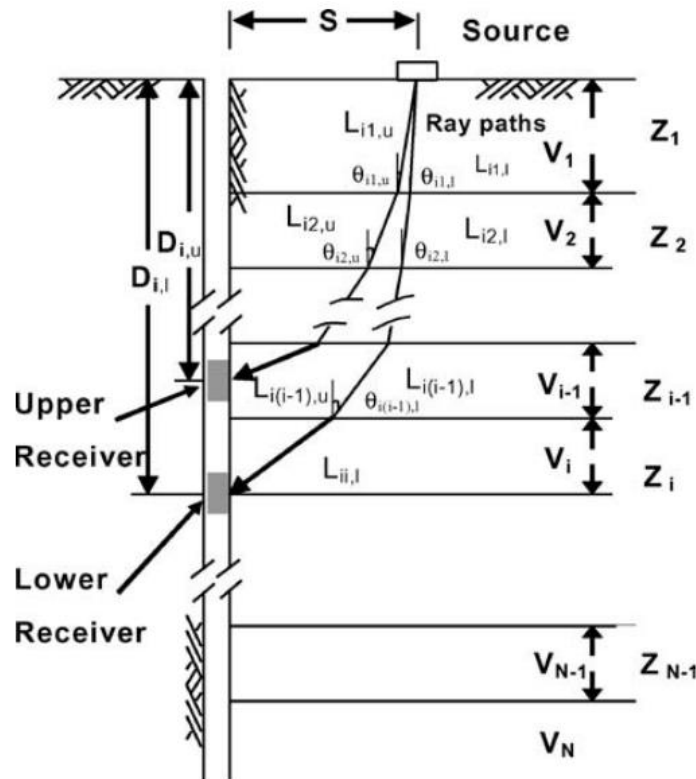


Figure 2.9 Illustration of Snell's Law ray path method for reducing downhole shear wave velocity ( $V_s$ ) data. Reprinted, with permission from the Geotechnical Testing Journal, Vol. 27, No. 6, 2004, copyright ASTM International, 100 Barr Harbor Drive, West Conshohocken, PA 19428.

Issues with estimating downhole  $V_s$  are of greatest concern when the source-to-cone offset is large, and when soil layers have high contrasts in stiffness. Also, the greatest variation between  $V_s$  estimates are likely to occur when analyzing data obtained for the second and/or third layer below the ground surface. When applying the modified interval method for source-to-cone offsets  $< 1.5$  m, the percent difference from values calculated by Snell's Law ray path method is typically  $< 1$ -2% throughout the profile, but may be up to 6-7% at very large contrasts in soil stiffness. However, for profiles in the database of this study, even large stiffness contrasts may have percent differences  $< 2\%$  if the horizontal source offset is only 0.5 m. The modified interval method (Equation 2.1) offers a significantly improved estimate when compared to a difference of 36% at high stiffness contrasts using the interval method. In general, where the downhole measurements are made at intervals  $< 2$  m, and the source-to-cone offset is  $< 1.5$  m, the estimated  $V_s$  values from the modified interval are  $< 1\%$  of the Snell's Law ray path method estimates, which are considered the most reliable of the possible data reduction values.

## **2.5 Measured to Estimated Shear Wave Velocity**

The ratio of measured  $V_s$  to estimated  $V_s$  ( $MEVR$ ) is a promising index for quantifying the effects of aging processes on soil liquefaction resistance. Andrus et al. (2009) proposed estimating  $V_s$  based on a  $q_t - V_s$  relationship for uncemented sand deposits that are ~6 years old, which is defined as:

$$(V_{s1})_{cs} = 62.6[(q_{t1N})_{cs}]^{0.231} \quad (2.2)$$

where  $(V_{s1})_{cs}$  = overburden stress-corrected clean sand-equivalent shear wave velocity;  $(q_{t1N})_{cs}$  = average of normalized and corrected cone tip resistance over the interval corresponding to the measured  $V_s$ . The measured  $V_s$  used to compute  $MEVR$  is also corrected for overburden stress and fines content following procedures recommended by Youd et al. (2001) and Juang et al. (2001). As mentioned previously, Figure 2.8e shows the variation in  $MEVR$  versus depth for the example SCPTu profile Qws85. The plotted values of  $MEVR$  represent the average value over an interval corresponding to the  $V_s$  measurement interval. Plotted values of  $MEVR$  in Figure 2.8e increase from around 1.0 near the ground surface to 1.5 at a depth of 16 m. Below 17 m,  $MEVR$  values increase above 2.0, which is typical of the Cooper Marl.

Presented in Figure 2.10 is a composite plot of  $MEVR$  with depth for Qsbs, provided as an example profile. Values closer to the ground surface show a tighter range, suggesting a lower degree of diagenesis and/or disturbance during the 1886 Charleston earthquake.  $MEVR$  values at depth increase from around 1.0 to over 6.0, indicating stiffer soil structure due to diagenetic changes. This reflects the generally greater resistance to liquefaction within deeper sections of the profile.

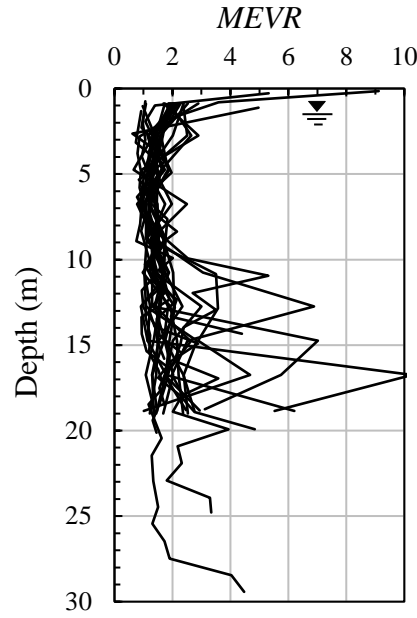


Figure 2.10 Composite *MEVR* profile for Qsbs. Depicted groundwater level represents average depth within deposit based on available data.

## **2.6 Liquefaction Potential Index**

The liquefaction potential index (*LPI*) is used to characterize overall liquefaction susceptibility and liquefaction potential at the SCPT and SCPTu sites. *LPI* has been used in the analysis of liquefaction susceptibility and potential because it offers a single value for a site, is one of the best single-value approaches currently available, and may be used to compare with results of other researchers (Holzer et al. 2006, 2009; Lenz and Baise 2007; Cramer et al. 2008, 2012; Hayati and Andrus 2008a; Heidari and Andrus 2010, Heidari 2011). *LPI* is defined as (Iwasaki et al. 1978):

$$LPI = \int_0^{20m} F \bullet w(z) dz \quad (2.3)$$

where  $F = 1 - FS$  for  $FS \leq 1$  and 0 for  $FS > 1$  ( $FS$  is factor of safety against liquefaction triggering, defined as the cyclic resistance ratio divided by the cyclic stress ratio);  $z$  is depth below ground surface in meters; and  $w(z)$  is a depth weighting function. *LPI* therefore depends on the thickness of liquefiable layers in the top 20 m, their proximity to ground surface, and their associated  $FS$ .



Presented in Figure 2.11 are example *LPI* calculations for Qws85 assuming peak ground acceleration ( $a_{max}$ ) = 0.25 and  $M_w$  = 7.0 (approximate earthquake loading on the Charleston Peninsula during the 1886 earthquake), and based on the liquefaction triggering procedure by Boulanger and Idriss (2016). Added to this procedure is the diagenesis correction factor ( $K_{DR}$ ) applied to the cyclic resistance ratio (*CRR*), where  $K_{DR} = 1.08MEVR - 0.08$ . This equation for  $K_{DR}$  was found by Heidari and Andrus (2012) to be the most appropriate  $K_{DR}$  relationship, of those proposed by Hayati and Andrus (2009). Plotted in Figure 2.11a are profiles of overburden stress-corrected cone tip resistance ( $q_{t1N}$ ) and stress-corrected clean-sand equivalent cone tip resistance ( $q_{t1N,cs}$ ). Figure 2.11b shows the profile of soil behavior type index ( $I_c$ ) versus depth, using  $I_c$  as defined by Lunne et al. (1997). Layers with  $I_c > 2.6$  are considered nonsusceptible to liquefaction and are not considered in the calculations of *LPI*. Figure 2.11d presents the calculated values of cyclic stress ratio (*CSR*) and *CRR* versus depth, with both  $K_{DR} = 1.0$  and  $K_{DR} \neq 1.0$  ( $CRR_K$ ). Figure 2.11f indicates that *LPI* based on  $K_{DR} = 1.0$  is 17, which incorrectly suggests moderate to severe liquefaction in Qws during the 1886 Charleston earthquake.

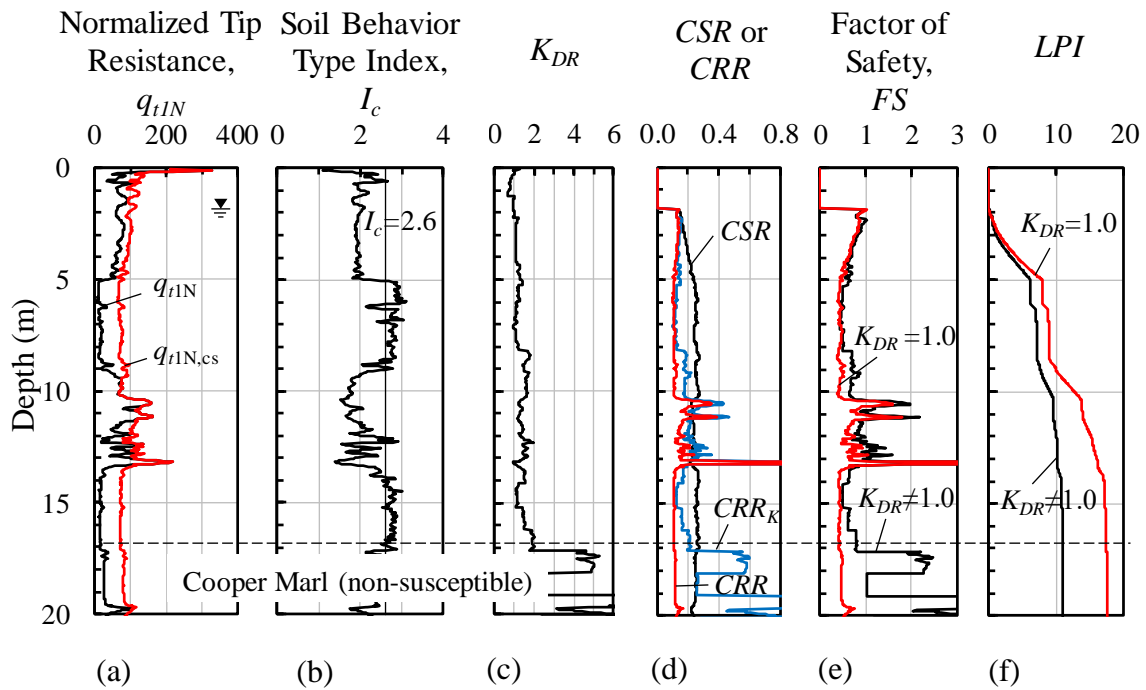


Figure 2.11 *LPI* calculation for site Qws85 assuming  $a_{max} = 0.25g$  and  $M_w = 7.0$ .

For the computed *LPI* to be considered in this study, SCPT profiles needed to extend to depths  $\geq 20$  m, extend into the nonsusceptible Cooper Marl, or terminate within 2 m (Qhs, Qws, Qwls, Qts, Qps) or 3 m (Qsbs) of the Cooper Marl, based on available geologic maps. A 3-m standard for Qsbs was allowed because many of the sites within this unit would otherwise be eliminated. Where cone soundings were terminated 2-3 m above 20 m or Marl, the remaining profile was assumed to be the same as the last 2-3 m. Some profiles were removed from *LPI* calculations due to limitations such as:  $V_s$  measurements covering an interval  $> 4$  m; uncertainty in  $u_2$  baseline values; excessive data points with negative sleeve friction; and failure to achieve sufficient test depth. These criteria resulted in a reduced number of sites used in *LPI* calculations, providing 30, 22, 82, and 46 profiles for Qhs, Qsbs, Qws, and Qts, respectively. No sites were eliminated from Qwls and Qps. Thus, 16 and 17 sites were retained for each of these surficial units, respectively. Due to uncertainty in  $u_2$  baseline values for three of the SCPTu profiles in Qwls (Qwls14-16), a single  $V_s$  profile was averaged from the three SCPTu's and applied to three CPTu profiles from the same research test location near Hollywood, SC. These CPTu profiles were repeated tests conducted at the original test site in order to obtain correct  $u_2$  values (Hasek 2016). The resulting *LPI* values calculated from the three CPTu profiles were then averaged to provide a single *LPI* value for the site. Averaging the *LPI* values from these profiles was done in order to minimize any potential error that may have been introduced by applying the average  $V_s$  profile of nearby test holes.

## **2.7 Liquefaction Susceptibility Assessment**

The liquefaction susceptibility of the six sand units is evaluated using the *LPI* method and assuming a constant earthquake loading of  $a_{max} = 0.25g$  and  $M_w = 7.0$  for the entire study area. Although  $a_{max}$  would vary during a seismic event as a function of distance from source, the assumption of  $a_{max} = 0.25g$  is made in order to assess relative susceptibility across the six sand units, including the influence of distance from Woodstock fault ( $d_f$ ). The *LPI* results for the constant earthquake loading are presented in Figures 2.12 and 2.13.

Presented in Figure 2.12 is the relationship between *LPI* and  $d_f$  for (a) Qhs, (b) Qsbs, (c) Qws, (d) Qwls, (e) Qts, and (f) Qps. For each unit the *LPI* values range from 0 – 20, except for one statistical outlier in Qps. The large amount of scatter in the data suggests that a single probability curve (independent of  $d_f$ ) for each unit is appropriate, given that no visible trends are detected which would merit otherwise. An initial analysis by Heidari and Andrus (2012) suggested that a closer proximity to the seismic source may lead to lower *MEVR* and weaker soil structure as a result of increased ground shaking from previous seismic events. However, the plotted data suggest that none of the units exhibited a strong correlation between distance from Woodstock fault and *LPI* for the range of  $d_f$ . This difference in findings can be attributed to the augmented database now included in this study. It may be noted, however, that all but one of the six plots show a negative-sloping best-fit line, indicating slightly lower *LPI* with greater distance from the fault. Overall, Figure 2.12 suggests that sites in Qhs are just as susceptible to liquefaction as sites in Qps when considering all the factors contributing to *LPI*. The earthquake loading conditions are the most significant controls on liquefaction occurrence for the sand deposits in this study.

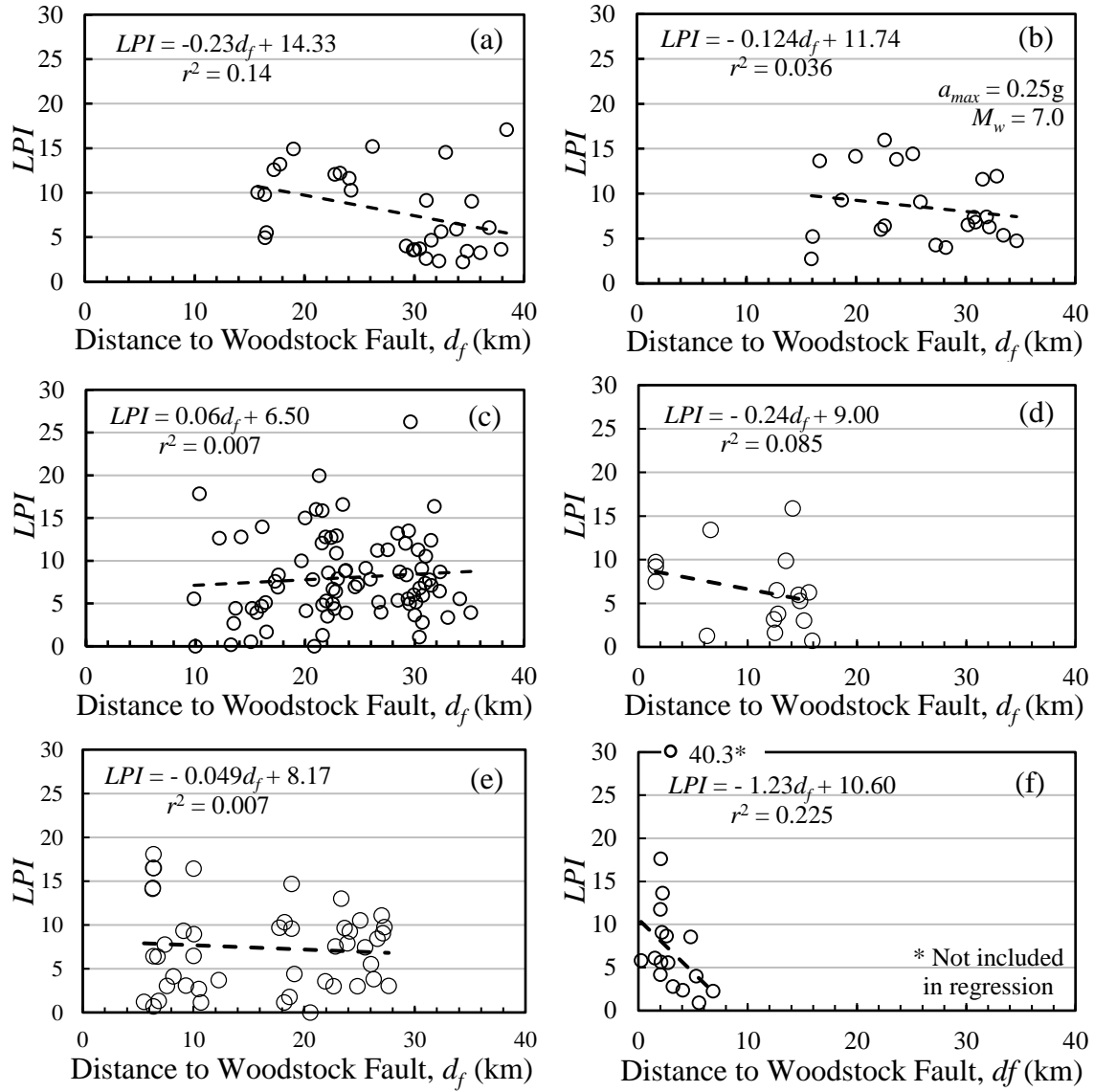


Figure 2.12 Plot of  $LPI$  versus distance to Woodstock fault for (a) Qhs, (b) Qsbs, (c) Qws, (d) Qwls, (e) Qts, and (f) Qps based on constant earthquake loading (i.e.,  $a_{max} = 0.25g$ ,  $M_w = 7.0$ ).

An additional analysis of  $LPI$  versus distance to Woodstock fault was undertaken for the loading scenarios of  $M_w = 7.0$  and  $a_{max} = 0.1g$  and  $0.5g$  for the sand units. The results of this analysis likewise indicate a weak correlation between  $LPI$  and  $d_f$ , and a relative liquefaction susceptibility among the units that is consistent with the findings from Figure 2.12. In terms of their age, the plots in Figure 2.12 have similar ranges among the data and trend lines. This suggests little influence of age on liquefaction susceptibility for the given earthquake loading and range of  $d_f$ .

Presented in Figure 2.13 are histograms and probability density functions ( $PDF$ ) showing the frequency of occurrence for the computed  $LPI$  values within (a) Qhs, (b) Qsbs, (c) Qws, (d) Qwls, (e) Qts, and (f) Qps for the constant earthquake loading. The data presented in this figure are assumed to be lognormally distributed. The six histograms show greatest frequency for  $LPI$  values between 3 and 12, with distributions skewed to the right. The  $PDF$  curves also indicate a slightly higher average  $LPI$  for Qhs and Qsbs, and lower average  $LPI$  for Qwls and Qps. However, the distributions are fairly similar among all units.

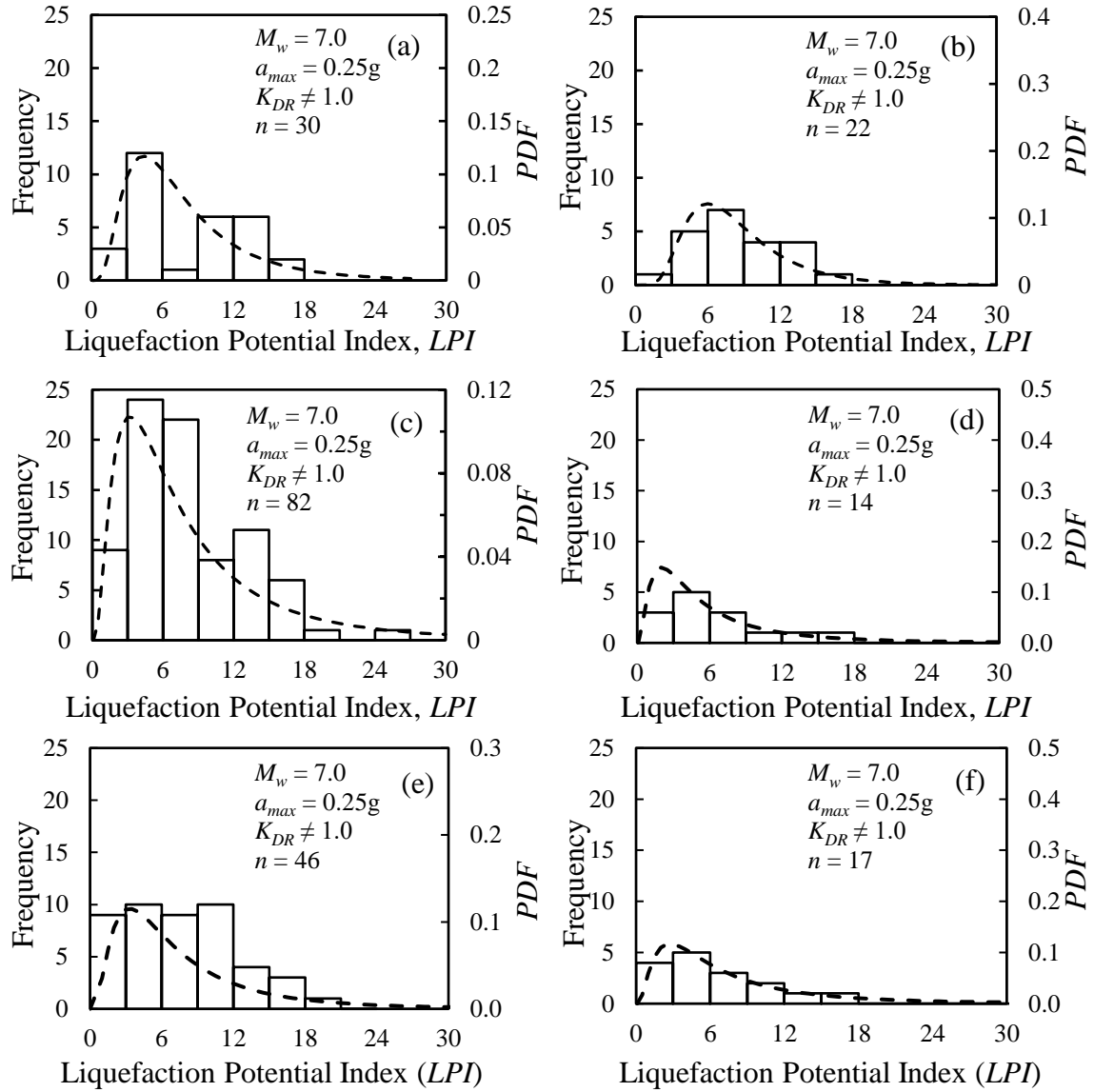


Figure 2.13 Probability density function (PDF) and  $LPI$  histogram for (a) Qhs, (b) Qsbs, (c) Qws, (d) Qwls, (e) Qts, and (f) Qps based on constant earthquake loading.

Presented in Figure 2.14 are cumulative distribution function (*CDF*) curves for the six sand units based on calculated values of *LPI*. Figure 2.14 shows that the sand units have generally similar *LPI-CDF* relationships for the same constant earthquake loading. However, until reaching nearly 85% of the data, Qwls has a smaller *LPI* value than the remaining five units, indicating lower susceptibility. The two units with the higher *LPI* value until reaching 50% – 60% cumulative distribution are Qsbs followed by Qhs.

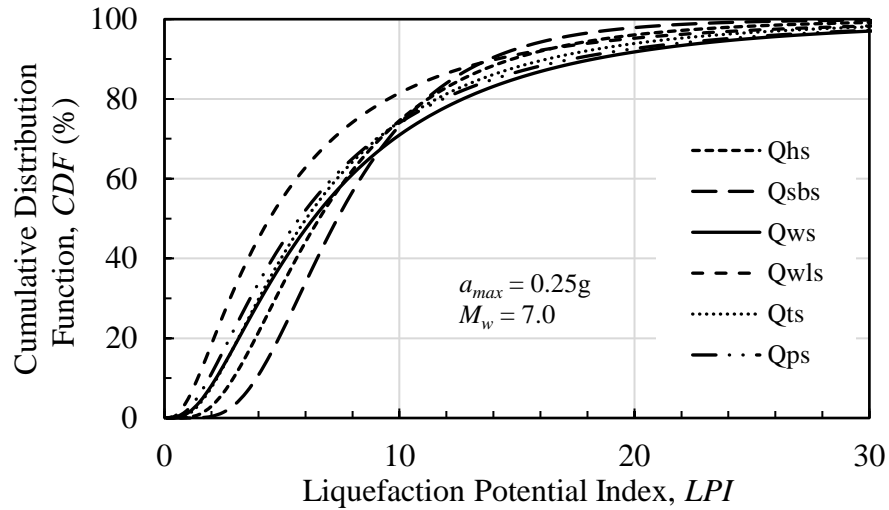


Figure 2.14 *CDF* curves for *LPI* values of Qhs, Qsbs, Qws, Qwls, Qts, and Qps based on constant earthquake loading (i.e.,  $a_{max} = 0.25g$ ,  $M_w = 7.0$ ).

Presented in Figure 2.15 are box-and-whisker plots for the six sand units generated from calculated values of  $LPI$ . Overall, the six units have common ranges of  $LPI$ , with Qws and Qps having the greatest spread due to a larger sample size (Qws) and presence of an outlier (Qps). Mean and median  $LPI$  values are also comparable across units, and are tabulated in Table 2.3. When outliers are omitted, the younger Qhs and Qsbs sand deposits were found to have slightly higher mean  $LPI$  values, and Qwls and Qps show the lowest mean values. The general similarity between units may be explained by underlying deposits often being the same and/or being formed by like depositional processes. These commonalities may contribute similarly to overall liquefaction susceptibility.

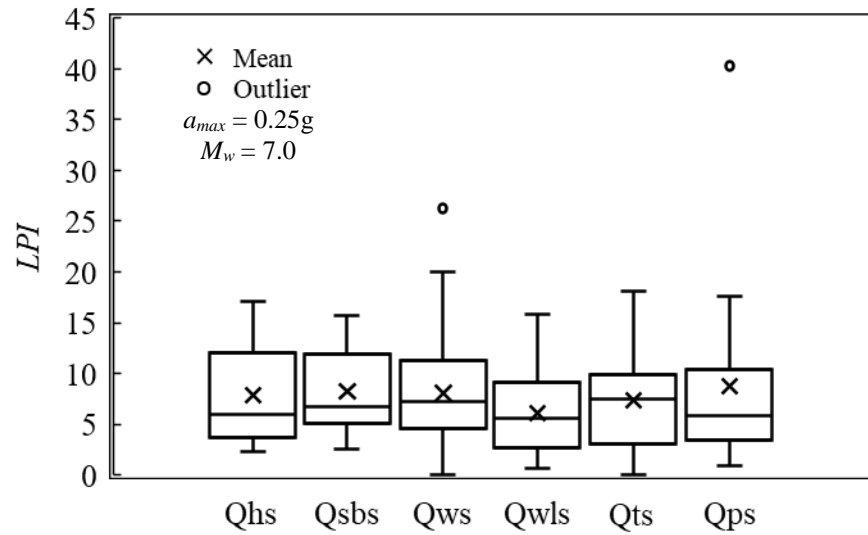


Figure 2.15 Box-and-whiskers plots of  $LPI$  values for Qhs, Qsbs, Qws, Qwls, Qts, and Qps based on constant earthquake loading (i.e  $a_{max} = 0.25g$ ,  $M_w = 7.0$ ).

Table 2.3  $LPI$  statistics for six sands, assuming a constant earthquake loading of  $a_{max} = 0.25g$  and  $M_w = 7.0$ . Value in parentheses represents the mean when outlier is omitted.

Surface Geology	Mean $LPI$	Median $LPI$	Standard Deviation	$n$
Qhs	7.9	6.0	4.6	30
Qsbs	8.2	7.1	3.9	22
Qws	8.0 (7.8)	7.2	4.5	82
Qwls	6.1	5.6	4.5	16
Qts	7.4	7.5	4.9	46
Qps	8.8 (6.8)	5.8	4.5	17

## 2.8 Liquefaction Probability Curves for Regional Hazard Mapping

Shown in Figure 2.16 are liquefaction probability curves for Qhs, Qsbs, Qws, Qwls, Qts, and Qps. The curves are based on results of  $LPI$  calculations performed on the SCPT and SCPTu profiles by varying  $a_{max}$  between 0.1 and 0.7 g and  $M_w$  between 5 and 9, and assuming  $LPI$  values are lognormally distributed. The basis of the probability curves is derived from the methodology proposed by Holzer et al. (2006) and Rix and Romero-Hudock (2007), with two modifications. First, in place of magnitude scaling factor ( $MSF$ ), the probability curves are constructed from pairs of  $a_{max}$  and magnitude ratio ( $MR$ ), where  $MR = 7.5/M_w$ .  $MR$  is used due to the depth dependence of the  $MSF$  relationship in the Boulanger and Idriss (2016) procedure. The interval of  $a_{max}$  used is 0.02g between 0.1g and 0.3g, and 0.1g from 0.3g to 0.7g. The interval of  $M_w$  is every 0.5.

The second modification involves the assumed  $LPI$  threshold ( $LPI_t$ ) separating no to minor manifestations of liquefaction from moderate to severe surface manifestations. Holzer et al. (2006) and Rix and Romero-Hudock (2007) assumed  $LPI_t = 5$ . Maurer et al. (2015a) studied the relationship between surface manifestation of liquefaction and average cone soil behavior type index in the top 10 m ( $I_{c10}$ ) at over 7,000 sites in Christchurch, New Zealand, and found that  $LPI_t = 6$  for sites with  $I_{c10} < 2.05$  and  $LPI_t = 15.5$  for sites with  $I_{c10} \geq 2.05$ . The  $I_{c10}$  values computed for the Charleston area vary greatly within a surface geology and are often well distributed across the  $I_{c10} = 2.05$  boundary. Thus, to better match observed ground behavior, a weighted  $LPI_t$  is used for each unit (i.e., 9 for Qhs, 14 for Qsbs, 13 for Qws, 12 for Qwls, 12 for Qts, and 15 for Qps). Table 2.4 provides a range of  $I_{c10}$  values and the assumed  $LPI_t$  for the profiles in this dataset.

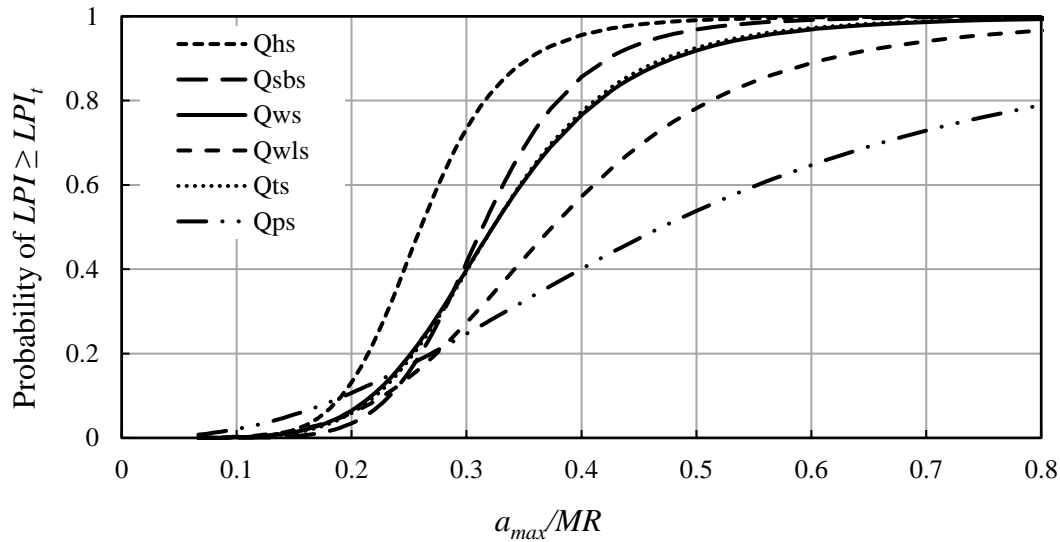


Figure 2.16 Liquefaction probability curves for Qhs, Qsbs, Qws, Qwls, Qts, and Qps.



The probability curves presented in Figure 2.16 are defined by:

$$P_{LPI \geq LPI_t} = 1 / \left( 1 + \left[ (a_{\max} / MR) / a \right]^b \right) \quad (4)$$

where  $a$  and  $b$  are curve-fitting variables. The values of  $(a, b)$  for Qhs, Qsbs, Qws, Qwls, Qts, and Qps are (0.260, -7.147), (0.314, -7.383), (0.323, -5.560), (0.374, -4.423), (0.323, -5.779), and (0.470, -2.486), respectively.

The curves in Figure 2.16 tend to reflect a decreased probability of liquefaction as the geologic age of the deposit increases. However, the curve for Qts matches well with the curve for Qws, despite the nearly 100 ka difference in age. This may be due in part to the relative influence of weighted  $LPI_t$  on probability curves. For a given deposit, a greater  $LPI_t$  tends to recline the curve to the right. The effect may be such that an  $LPI_t$  of 13 for Qws pushes the curve to the right, and an  $LPI_t$  of 12 for Qts maintains the curve to the left somewhat, thereby overlapping the curves for the two units. Also to be considered is the change in behavior of Qts due to previous seismicity, which may have disturbed the microstructure of the soil.

Based on the probability curves in Figure 2.16 and for a given  $a_{\max}/MR$ , the unit with the greatest potential for liquefaction is Qhs, and the unit with the least potential is Qps. Although, at small values of  $a_{\max}/MR$ , particularly near 0.25, the curves largely overlap. As the magnitude and/or ground acceleration increases, greater differences in the liquefaction probability of these six sand units is predicted. The greatest overall differences in the curves are seen at an  $a_{\max}/MR$  value of 0.4. At higher degrees of earthquake loading, the occurrence of liquefaction becomes more uniformly probable for all surface geologies.

Table 2.4 Range of  $I_{c10}$  values and assumed  $LPI_t$  for surficial sand deposits.

Surface Geology	Minimum value $I_{c10}$	Maximum value $I_{c10}$	Average $I_{c10}$	$LPI_t$
Qhs	1.69	2.38	1.96	9
Qsbs	1.74	2.70	2.23	14
Qws	1.70	2.74	2.21	13
Qwls	1.92	2.50	2.13	12
Qts	1.78	2.59	2.13	12
Qps	2.25	2.71	2.49	15

The observations of disturbance along railroads discussed in Section 2.3 provide an estimate on the percentage of area covered by each unit that experienced damage related to liquefaction. These estimates are used here to verify the probability curves presented in Figure 2.16. Based on notes by Earle Sloan and W. J. McGee along the railway lines, approximately 8% of Qws, 18% of Qwls, 17% of Qts, and 14% of Qps experienced minor to severe surface manifestations of liquefaction. No recorded observations of failures in Qhs and Qsbs were included in their notes.

Table 2.5 presents a rough approximation of average earthquake loading along the railway lines within each unit, given that ground accelerations during the 1886 earthquake would vary as a function of distance to fault. The estimated values of  $a_{max}$  are based on maps from Silva et al. (2003) assuming  $M_w = 7.3$ , and on a SHAKE analysis from Bwambale (2018) using  $V_s$  profiles from Qts (see Appendix E). Using the approximate loading values indicated, Table 2.5 presents the predicted probability of  $LPI \geq LPI_t$  for sand deposits, based on the probability curves in Figure 2.16. Under the given loading assumptions, the probabilities predicted by the curves generally over-estimate the percentage of the rail lines with observed liquefaction, with the possible exception of Qwls where the predicted value coincides closely with the percentage of observed rail line disturbance. The greatest over-estimate is the predicted probability for  $LPI \geq LPI_t$  within Qts, followed by the predicted probabilities for Qws and Qps to a lesser extent. Thus, the probability curves offer a conservative yet reasonable prediction for liquefaction occurrence in Qhs, Qsbs, Qws, and Qps. Efforts to apply the curves should ensure that the assumed values of  $a_{max}/MR$  are representative of the given location. Bwambale (2018) in Appendix E presents further discussion on the liquefaction probability of Qts.

Table 2.5 Comparison of observed liquefaction along railway lines versus predicted probability of  $LPI \geq LPI_t$  for sand deposits.

Surface Geology	Distances from Rail Line to Fault (km)	Observed Minor to Severe Liquefaction Along Rail Line (%)	Approximate Loading		Probability of $LPI \geq LPI_t$ (%)
			$a_{max}$	$M_w$	
Qhs	N/A	N/A	0.15*	7.0	1.2
Qsbs	N/A	N/A	0.18*	7.0	1.6
Qws	9.9 – 21.8	8	0.27	7.0	20.4
Qwls	5.4 – 16.4	18	0.30	7.0	21.7
Qts	0.0 – 11.4	17	0.32	7.0	38.9
Qps	0.0 – 18.6	14	0.30	7.0	21.6

N/A = not available because rail lines do not intersect surficial deposit

\*Estimated based on average distance between surficial deposit and Woodstock fault, not along rail line

## **2.9 Conclusion**

The overall liquefaction susceptibility of six surficial sand deposits in the greater Charleston area was characterized using 228 SCPT profiles from sites located 0 to 39 km from the Woodstock fault and assuming a constant ground shaking. Computed *LPI* values for five of the six units exhibited only slight increasing correlation with distance to the fault. Cumulative distributions of *LPI* values for a constant loading are similar for all six units with Qwls showing slightly less susceptibility.

Liquefaction probability curves were expressed as a function of  $a_{max}/MR$  and a weighted threshold *LPI* at which surface manifestations occur. Qhs exhibited the highest probability of liquefaction for a given  $a_{max}/MR$ , and Qwls and Qps exhibited the lowest probability. Qsbs, Qws, and Qts exhibit a similar probability to each other which is less than Qhs but greater than Qwls and Qps. These probability curves were shown to agree well with the observations of ground failure following the 1886 earthquake. The results may be used to create regional hazard maps, but should not replace site-specific evaluations.

## CHAPTER THREE

### LIQUEFACTION PROBABILITY OF SURFICIAL CLAYEY UNITS IN THE CHARLESTON AREA

#### **3.1 Introduction**

The liquefaction probability of surficial clayey deposits in the Charleston area is characterized in this chapter. The characterization begins with a discussion of their ground behavior following the 1886 earthquake. Next, liquefaction susceptibility is assessed among the deposits, with consideration for geologic age, distance to Woodstock fault zone, and for the first time, distance to nearest perennial stream or river. Finally, liquefaction probability curves are developed for the given units, based on both site-specific conditions and uniform conditions of depth to groundwater and depth to Cooper Marl.

A map of the Charleston area is presented in Figure 3.1. Included on the map are: 1) the likely source of the 1886 earthquake (Woodstock fault zone), 2) spatial distributions of five Quaternary surficial clayey deposits, 3) locations of selected 1886 earthquake observed ground behavior in these deposits, and 4) locations of 90 seismic cone penetration tests (designated as SCPT if no pore pressure measurements were made and SCPTu if pore pressure measurements were made) conducted in the clayey deposits. This number of cone penetration tests is nearly three times the number Heidari (2011) used to characterize the liquefaction probability of four of these units.

#### **3.2 Geology**

Pleistocene formations within the greater Charleston area include three distinct facies from three main depositional environments: fluvial-estuarine-backbarrier, barrier-island, and open-marine shelf (Weems and Lemon 1988). In this chapter, five of the surface deposits associated with fluvial-estuarine-backbarrier environments are considered for analysis, including Qsbc, Qwc, Qtc, Qlc, and Qpc.

Qsbc (33–85 ka) is a clayey sand and clay facies from the Silver Bluff beds and is often present along rivers and streams at elevations below 3 m. Qwc (70–130 ka) is a clayey sand and clay facies of the Wando Formation, and likely formed in fluvial to estuarine environments as suggested by the presence of wood and terrestrial vertebrate fossils (Weems et al. 2014). Qtc (200–240 ka) is a clayey sand and clay facies from the Ten Mile Hill Formation. It underlies the lower Talbot terrace (Colquhoun 1974) and is dominant in areas to the north and northwest of Charleston. Qlc (240–730 ka) is a clayey sand and clay facies of the Penholoway Formation that underlies the upper Talbot terrace (Colquhoun 1974). Weems et al. (2014) suggest that Qlc was deposited in fluvial, estuarine, and lagoonal environments. Qpc (730–970 ka) is a clayey sand and clay facies of the Penholoway Formation and is located the farthest inland of the five units considered, at ground surface elevations around 20 m. Due to sequences of sea level transgression and regression, the older deposits are generally located farther from the coast and at higher elevations than each successively younger unit.

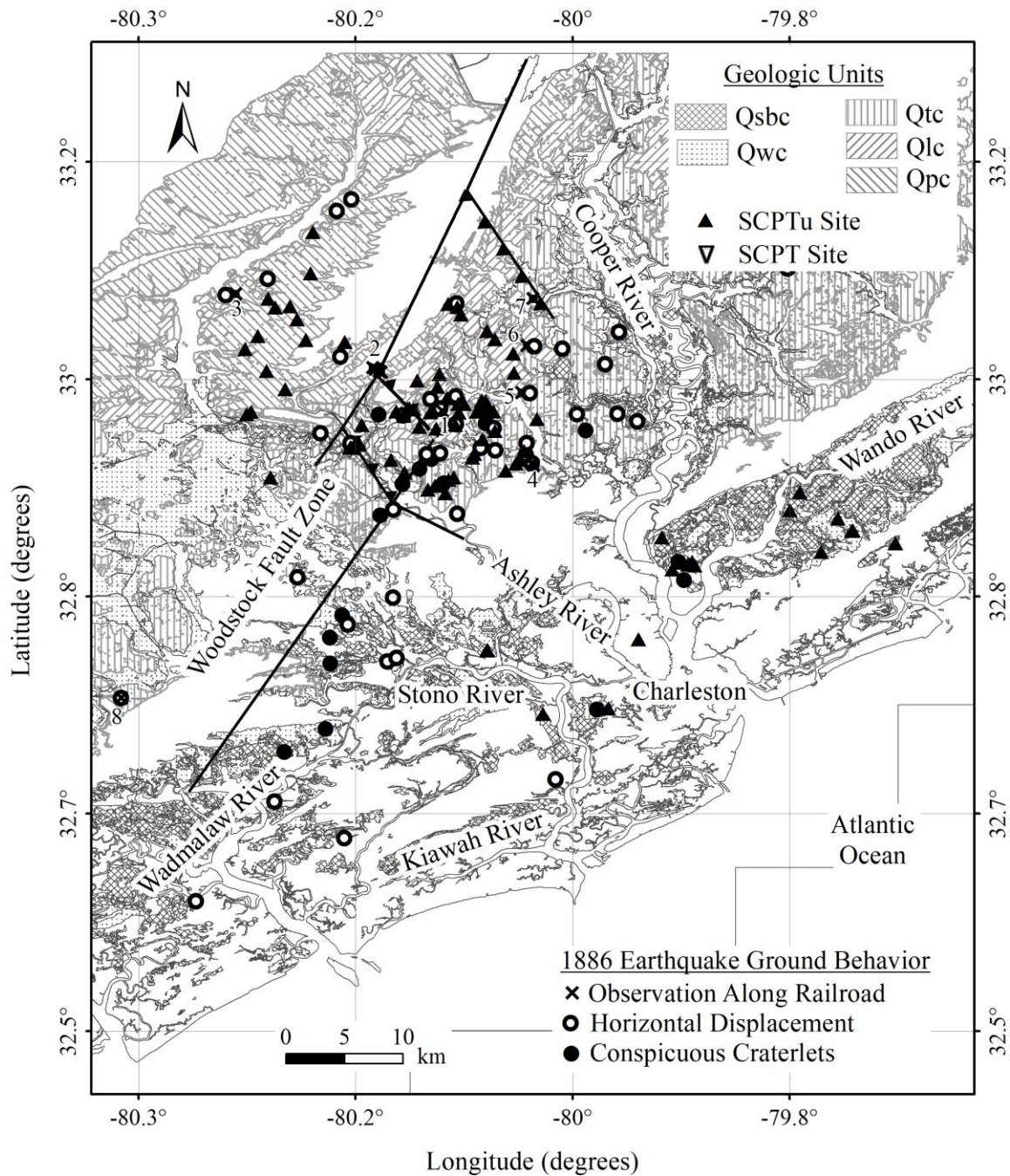


Figure 3.1 Geologic map of the Charleston area showing surficial clayey deposits (modified from Heidari and Andrus 2012; Weems et al. 2014), the Woodstock fault zone (Durá-Gómez and Talwani 2009), seismic cone penetration test sites within Qsbc, Qwc, Qtc, Qlc, and Qpc, and mapped sites of ground failures within these units (Dutton 1889, PLs. XXVII & XXVIII; Peters and Hermann 1986).

Table 3.1 presents the average values of reported depths to groundwater table at the SCPT/SCPTu sites for each of the five units. All profiles have reported water table depths that were provided in the cone data files, with the exception of Qsbc1. For this profile, an average water table depth from the other profiles within Qsbc was determined, and applied to Qsbc1 during the *LPI* analyses. Efforts to assess liquefaction susceptibility of the clayey deposits, independent of water table levels, are outlined in this chapter.

Also included in Table 3.1 is the approximate range of depth below ground surface at which the Cooper Marl may be encountered. The depth ranges for the Cooper Marl are based on data presented in the geologic maps by Weems and Lemon (1988, 1993), and Weems et al. (1997), which generally agree well with profiles interpreted from the SCPT database and depths reported in geotechnical reports.

Table 3.1 Average depths below ground surface to water table and the top of Cooper Marl for surficial clayey deposits.

Surface Geology	Average Depth to Water Table (m)	Approximate Range of Depths to Cooper Marl (m)
Qsbc	1.40	6 to 18
Qwc	1.63	2 to 10
Qtc	2.05	4 to 14
Qlc	1.77	6 to 12
Qpc	2.60	5 to 13

### **3.3 1886 Earthquake and Ground Behavior**

Dutton (1889) reported several cases of ground failure that occurred during the 1886 earthquake, including 113 cases of horizontal ground displacement and 55 cases of conspicuous craterlets. Heidari (2011) estimated coordinates for these sites and noted that these areas include only major occurrences mapped by Earle Sloan. However, additional cases of lesser severity occurred at many other locations throughout the region (Hayati and Andrus 2008a; Heidari and Andrus 2010).

Within Qsbc, Qwc, Qtc, Qlc, and Qpc, the number of mapped occurrences of horizontal ground displacement in the Dutton (1889) report are 16, 1, 14, 9, and 4, respectively; and the number of mapped areas of conspicuous craterlets are 8, 0, 7, 1, and 0, respectively. Due to limited information regarding the original location of these ground failures in Dutton (1889) and the limitation of geologic maps, it is possible that some of these mapped failures actually occurred in adjacent units, despite careful efforts by Heidari (2011) to determine accurate coordinates. Sloping ground and the presence of other underlying units in the shallow subsurface may have also affected these observed ground behaviors. Yet these observations generally agree with the newspaper and other accounts compiled by Heidari and Andrus (2010) from Mount Pleasant (located east of the peninsula), as well as the field notes by Earle Sloan and W. J. McGee along the railway lines summarized in Table 3.2.

Assuming that the field notes by Sloan and McGee accurately describe all significant ground behavior (see Table 3.2), about 1.4% of the area along the railway lines through Qtc experienced moderate to severe surface manifestations of liquefaction, 4.7% experienced minor manifestations, and about 94% experienced none. For Qlc, approximately 1.3% of the total railway line distance within the unit experienced moderate to severe surface manifestations of liquefaction, 2.5% experienced minor surface manifestations, and the remaining 96.2% exhibited no surface evidence of liquefaction. For the distance of the railway lines through Qpc, about 1.3% experienced moderate to severe surface manifestations of liquefaction, 5.4% experienced minor, and 93.3% experienced none. Areas within a radius of 80 meters (0.05 mile) from observed craterlets were classified as moderate to severe liquefaction. Areas were classified as minor liquefaction if fissures and depressions were present within a radius of 80 meters, and no liquefaction if there were no observed disturbances or craterlets along the railway lines.

The field notes by Sloan and McGee did not include any observations of surface manifestations of liquefaction within Qsbc and Qwc deposits. However, documentation of disturbances to the railroad line within areas of artificial fill were included in their notes, and often map adjacent to Qsbc and Qwc. While it is likely that these disturbances are a result of ground failure within the fill deposits, the relative influence of fill deposits, Qsbc, and Qwc on the railroad disturbance remains uncertain. A more complete record of the observations along the railroad lines is included in extended tables of ground behavior along railroads in Appendix B.

Table 3.2 Disturbances along railroads in Qtc, Qlc, and Qpc during the 1886 Charleston earthquake (adapted from field notes by Earle Sloan and W. J. McGee as cited by Dutton [1889, pp. 283-294, 303-306] and Peters and Hermann [1986, pp. 18-26, 51-55, 62-64]).

Site No.	Surface Geology	Mile Point	Latitude (degrees)	Longitude (degrees)	Elev. (m)	Description of Disturbance
South Carolina Railroad						
1	Qlc	16.4	32.975708	-80.100185	---	Fissures and craterlets short distance from tracks; long (>200 m) fissure makes sharp turn before cut in slope for railroad
2	Qpc	19.66	33.005322	-80.146989	14.38	Culvert strained to the north and broken
		19.76	33.006021	-80.148318	5.49	Sever flexure to the east
		19.76	33.006097	-80.148455	5.49	Bending of wooden guard rail
		19.95	33.007564	-80.151212	14.93	Sinuuous flexures
		20.09	33.008737	-80.153331	15.21	Embankment over swamp; roadbed and superstructure forced to the right in series of irregular flexures, generally of no great amount
3	Qpc	27.38	33.065449	-80.258853	---	Jedburg – occasional craterlets; superstructure suffered stress to left at the south end of trestle
Northeastern Railroad						
4	Qtc	12.0	32.933806	-80.029967	7.92	Several fish-plates broken and joints parted; start of long flexure
	Qtc	12.09	32.934950	-80.030603	7.31	Flexure is 200 mm to the west; 51 mm crack extends across road and cut; within 46 m of track series of cracks developed with largest having widths of 530 mm and bearing N40E
	Qtc	12.13	32.935469	-80.030897	6.55	Superstructure shifted 2.5 m to the west and down grad jamming south end of trestle; bents of trestle inclined or fallen to the southeast; alignment restored by cutting out 550 mm section
5	Qlc	16.0	32.989658	-80.039014	12.80	Long sinuous curve in tracks through cut; ground thrown into ridges and rails bent in a vertical plane to conform to the fixed undulations
6	Qlc	18.51	33.025833	-80.034792	---	Descending grade; flexure along 370 m chord with 100 mm ordinate to the east
7	Qtc	21.0	33.061831	-80.030511	6.10	“Last manifestation of great energy”; flexure along 270 m chord with 76 mm ordinate to the east
Charleston and Savannah Railroad						
8	Qtc	29.85	32.755248	-80.346519	---	Adams Run Station – limiting line of craterlets



Figures 3.2 through 3.6 are histograms that present the relationship between inferred distance to Woodstock fault ( $d_f$ ) and the occurrence of ground failures reported by Dutton (1889) for each of the five clayey deposits. Also included in these figures are data for the railroad disturbances presented in Table 3.2 above. The distance to fault has been measured to the fault segments trending NE-SW, or to a linear projection of these segments. In each case, the occurrence of ground failures along the railroad and otherwise is well within the spatial extent of each deposit with respect to distance to fault. These figures indicate that surface evidence of liquefaction is constrained within certain distances from the Woodstock fault. Also evident is the relative number of occurrences of major craterlets and ground displacements in these units, as reported by Dutton (1889).

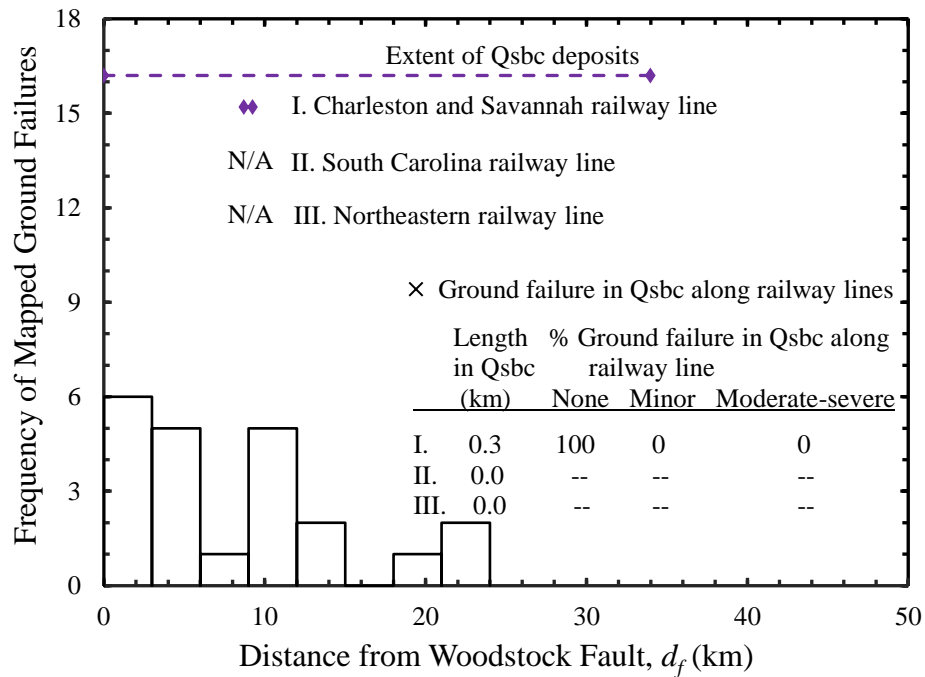


Figure 3.2. Histogram of ground failures reported by Dutton (1889) within Qsbc and railroad observation data from field notes of Sloan and McGee.

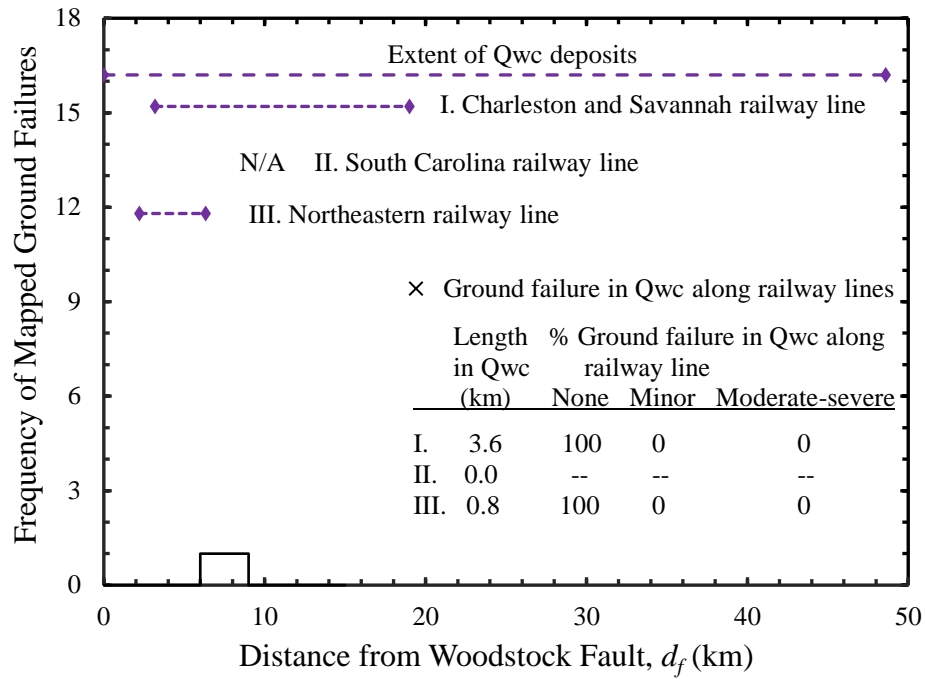


Figure 3.3 Histogram of ground failures reported by Dutton (1889) within Qwc and railroad observation data from field notes of Sloan and McGee.

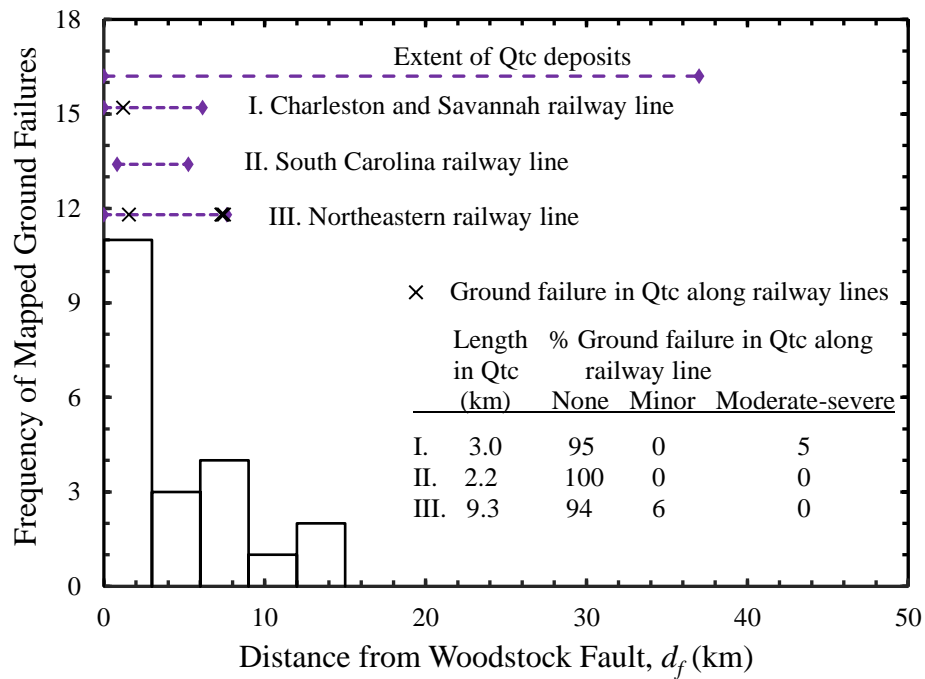


Figure 3.4. Histogram of ground failures reported by Dutton (1889) within Qtc and railroad observation data from field notes of Sloan and McGee.

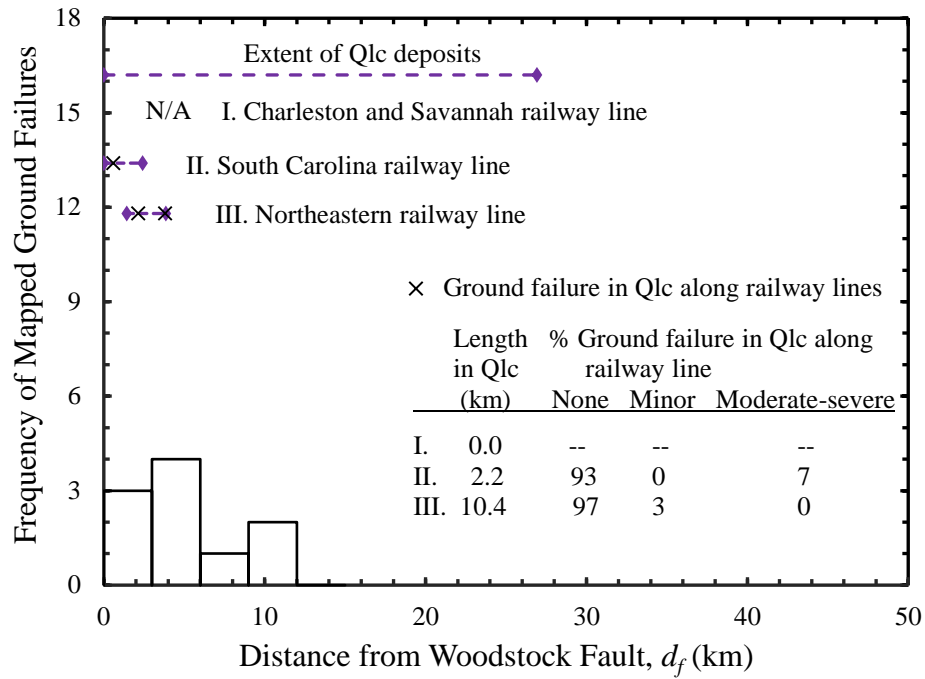


Figure 3.5. Histogram of ground failures reported by Dutton (1889) within Qlc and railroad observation data from field notes of Sloan and McGee.

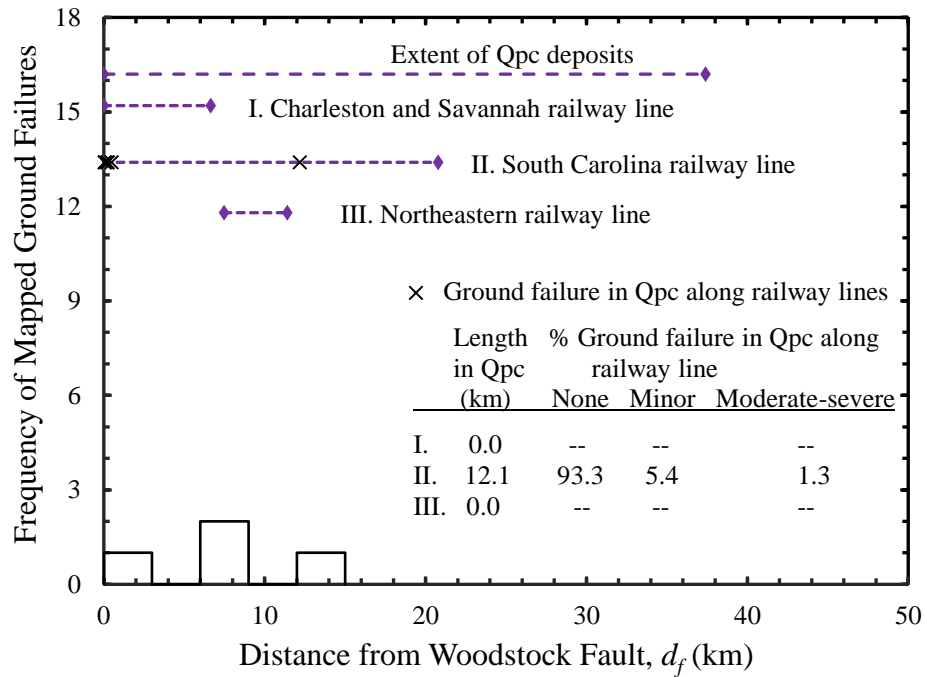


Figure 3.6. Histogram of ground failures reported by Dutton (1889) within Qpc and railroad observation data from field notes of Sloan and McGee.

### **3.4 Seismic Cone Penetration Test Data**

A compilation of 1 SCPT and 89 SCPTu profiles has been gathered from various available research and consulting reports. Table A-2 provides a summary of these sites. Of the 90 profiles total, 18 plot in Qsbc, 9 in Qwc, 23 in Qtc, 27 in Qlc, and 13 in Qpc. Twenty-four of the sites are the same as those analyzed by Heidari (2011) and their electronic files are available in Mohanan et al. (2006), as indicated in Table A.1. Heidari (2011) states that the coordinates associated with these SCPTu profiles are believed to be accurate within 100 m. Of the remaining 66 profiles, 16 are from project reports by S&ME (2005-2013), 41 are from projects by Terracon (2013-2016), and 1 SCPT is from the United States Geological Survey online database compiled by Thomas Holzer and his colleagues ([earthquake.usgs.gov/research/cpt/data/charleston/](http://earthquake.usgs.gov/research/cpt/data/charleston/)). Three of the 66 sites are from original work by Boller (2008), and the remaining five were compiled by Hasek (2016) at the Colonial Dorchester State Historic Site (“Fort Dorchester”). Coordinates for these 66 sites were obtained either directly from the project data files, or by identifying the site address from the report and pinpointing the CPT sounding location in Google Earth Pro software based on the site layout map. The location accuracy of these latter profiles is believed to be within 60 m.

The 3 SCPTu profiles from Boller (2008) were performed at the Coastal Research and Education Center (CREC). Previous researchers (Boller 2008; Boller et al. 2008; Hossain et al. 2014; Esposito et al. 2014) have identified the surface soil at the CREC field test site as the sand facies of the Wando Formation (Qws). While the 3 cone profiles and SPT/fixed-piston sample borings do show sand deposits present near the ground surface, Weems et al. (2014) map the test location to be at the center of Qsbc, a “silty to sandy clay and quartz sand” (Weems et al. 2014). According to their surficial geologic map, a Qws deposit is present at the surface 3 km to the east of CREC. In addition, computed *MEVR* values correspond more closely to Qws than younger deposits. While acknowledging these discrepancies, the three profiles in question have been grouped within Qsbc for this study. This decision bears in mind that future hazard mapping may rely heavily on available surface geology maps, and the need to remain consistent with such maps.

Ground surface elevations for each site in the database were obtained by plotting profile coordinates (LAT/LONG) in *The National Map Viewer*, a product of the U.S. Geological Survey’s National Geospatial Program. When elevations were reported with the cone data, these values were typically within 1 m of the elevations determined from *The National Map* ([viewer.nationalmap.gov/advanced-viewer/](http://viewer.nationalmap.gov/advanced-viewer/)). This free online resource was also the means by which the distance between each SCPT site and the closest perennial stream or river was obtained for liquefaction susceptibility assessment. The designation as a perennial stream or river is provided within the National Hydrography Dataset, which has been incorporated into *The National Map*.

The shear wave velocity ( $V_s$ ) data utilized in this study were originally analyzed using the pseudo-interval method or direct method. Where complete metadata were accessible (39% of the sites), downhole  $V_s$  data have been re-evaluated by means of the Snell’s Law ray path and modified interval methods (Kim et al. 2004). For sites with insufficient metadata (61% of the sites),  $V_s$  values were used as provided in the geotechnical reports. Included in those sites which were not re-evaluated are the 5 SCPTu profiles conducted at Fort Dorchester, where downhole, true-interval seismic testing was performed. See Figure 2.9 for illustration of the Snell’s Law ray path method.

### **3.5 Liquefaction Potential Index**

The liquefaction potential index (*LPI*) is used to characterize overall liquefaction susceptibility and liquefaction potential at the SCPT and SCPTu sites. The procedures used for calculating *LPI* are the same as those outlined in Chapter 2, which are based on the liquefaction triggering procedure by Boulanger and Idriss (2016). The cyclic resistance ratio (*CRR*) has again been multiplied by the diagenesis correction factor ( $K_{DR}$ ) to account for liquefaction resistance of aged soils, where  $K_{DR} = 1.08MEVR - 0.08$  (Hayati and Andrus 2009). Layers above the Cooper Marl with  $I_c > 2.6$  are considered nonsusceptible to liquefaction and are not included in the calculations. The Cooper Marl is likewise considered nonsusceptible to liquefaction (Li et al. 2007; Hayati and Andrus 2008b).

For the computed *LPI* to be considered in this study, SCPT profiles needed to extend to depths  $\geq 20$  m, extend into the nonsusceptible Cooper Marl, or terminate within 2 m above the Cooper Marl, based on available geologic maps. Only one cone sounding in the database (Qsbc8) terminated 2 m above the Cooper Marl, which was determined based on surface map data, the cone profile, and by comparison with nearby site Qsbc15. For this case, the remaining profile was assumed to be the same as the last 2 m. Two profiles from Qsbc (Qsbc2, Qsbc3) and one profile from Qtc (Qtc5) were precluded from *LPI* calculations due to the limitation of having  $V_s$  measurements covering an interval  $> 4$  m. Thus, for calculating *LPI*, the respective number of profiles for Qsbc, Qwc, Qtc, Qlc, and Qpc were 16, 9, 22, 27, and 13.

### **3.6 Liquefaction Susceptibility Assessment**

The overall liquefaction susceptibility of the five clayey units is evaluated using the *LPI* method and assuming a constant earthquake loading of  $a_{max} = 0.25g$  and  $M_w = 7.0$  for the entire study area. The assumption of  $a_{max} = 0.25g$  is made in order to assess relative susceptibility across the five clayey units, although  $a_{max}$  would vary during a seismic event as a function of distance from source. This assessment of liquefaction susceptibility evaluates the influence of distance to Woodstock fault ( $d_f$ ) and distance to a perennial stream or river ( $d_s$ ), based both on site-specific conditions of groundwater level ( $W$ ) and depth to top of Cooper Marl ( $D_{marl}$ ), as well as on uniform conditions (i.e.,  $W = 1$  m,  $D_{marl} = 5$  m). The relationship between depth to top of Cooper Marl and *LPI* is also evaluated. Computing *LPI* under uniform conditions has been done in an effort to constrain the influence of water table and marl, in order to isolate the behavior of the deposit alone. Under uniform conditions, the number of profiles analyzed for Qsbc, Qwc, Qtc, Qlc, and Qpc are 16, 4, 15, 27, and 13, respectively.

The liquefaction potential index is based on an expression that relates the thickness and factor of safety of liquefiable soil layers, and their proximity to the ground surface. The upper limit of integration for this calculation is a depth of 20 m. In cases where Cooper Marl is present within this range of the subsurface, the *LPI* calculation is concluded upon reaching marl. Since the Cooper Marl is considered nonsusceptible to liquefaction, it does not contribute to *LPI*. Thus, the depth at which marl is encountered directly influences the computed liquefaction potential.

Figure 3.7 displays this influence as a plot of *LPI* versus depth to Cooper Marl for (a) Qsbc, (b) Qwc, (c) Qtc, (d) Qlc, and (e) Qpc. Readily apparent in each plot is the positive slope indicating an increase in *LPI* as the depth to Cooper Marl increases. Having the marl located deeper below ground surface allows for thicker layers of potentially liquefiable soils to contribute positively to

the *LPI* calculation. Recognizing the depth to Cooper Marl as a significant factor of *LPI* is valuable in understanding the results of this study. Heidari (2011) found similar trends, consistent with the definition of *LPI*, including an increase in *LPI* as depth to groundwater decreased. This is the reason for which *LPI* has been calculated with profiles where the depth to the water table and depth to Cooper Marl have been artificially assigned to various depths, as discussed in this chapter. By so doing, a more accurate understanding of the Quaternary deposit behavior is achieved.

Figure 3.8 presents a combined plot of *LPI* versus inferred distance to Woodstock fault ( $d_f$ ) for each surficial clayey unit, based on *LPI* calculated under (a) site-specific conditions, and (b) uniform conditions of groundwater (i.e.,  $W = 1.0$  m) and Cooper Marl (i.e.,  $D_{marl} = 5.0$  m). The figures reveal scatter in the data for both conditions, particularly for the site-specific *LPI* in Figure 3.8a. However, a high  $R^2$  value for the data that plot in Qtc suggests an increase in *LPI* as  $d_f$  increases in Figure 3.8a. Yet this value reduces significantly for Qtc data in Figure 3.8b. When the influence of marl and groundwater is set to constant values, the slope of each trend line moves toward zero (Figure 3.8b). This indicates a minimal correlation between *LPI* and distance to Woodstock fault, which agrees with the research findings for the sand deposits presented in Chapter 2. An analysis of *LPI* versus  $d_f$  was also undertaken for earthquake loading parameters of  $M_w = 7.0$  and  $a_{max} = 0.1g$  and  $0.5g$ . Results show a similar trend as those presented in Figure 3.8, with no strong correlation between *LPI* and  $d_f$  for the range of  $d_f$  in this dataset.

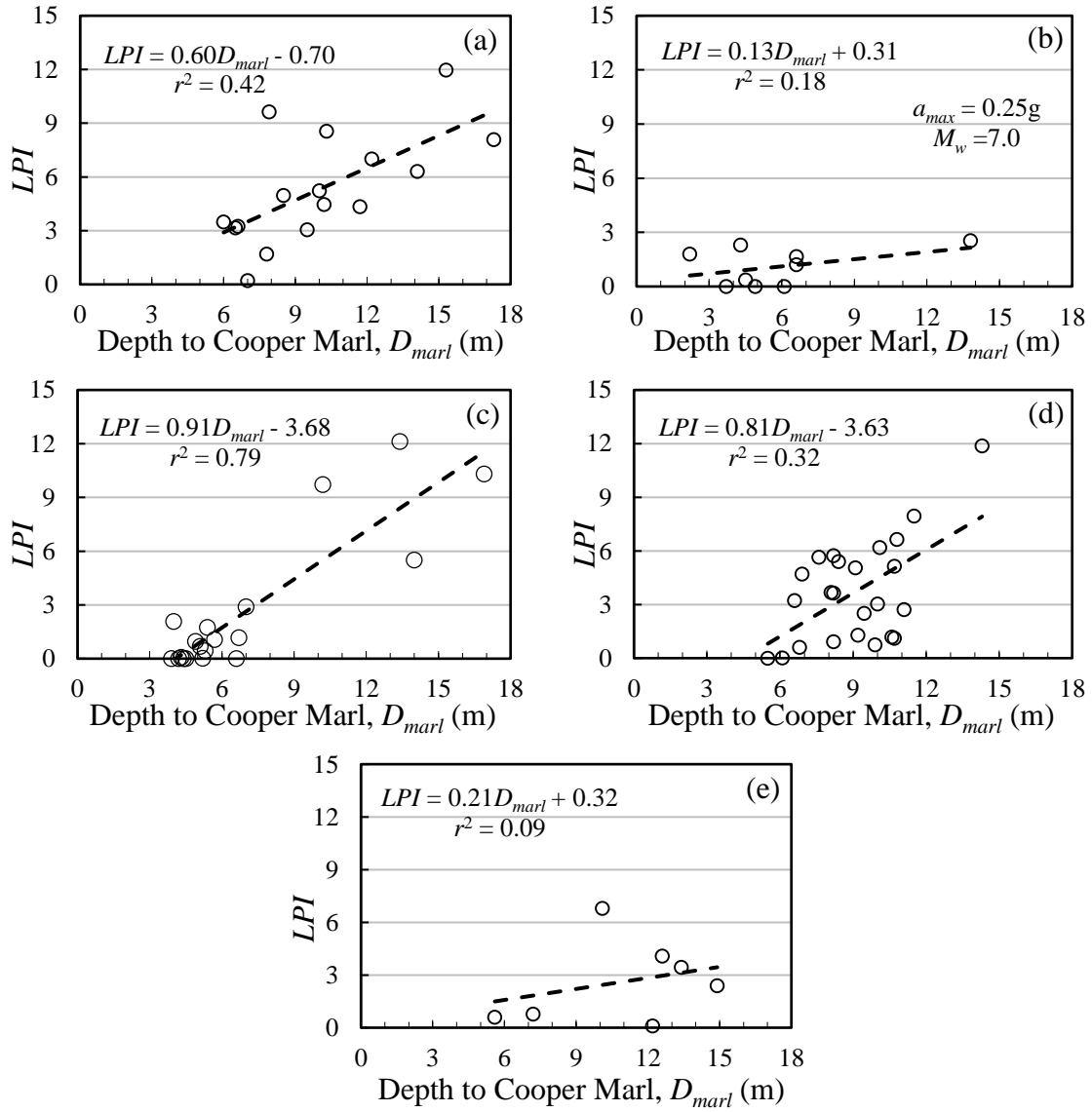


Figure 3.7 Plot of  $LPI$  versus depth to top of Cooper Marl for (a) Qsbc, (b) Qwc, (c) Qtc, (d) Qlc, and (e) Qpc based on constant earthquake loading (i.e.,  $a_{max} = 0.25g$ ,  $M_w = 7.0$ ) and site-specific conditions of groundwater and marl.

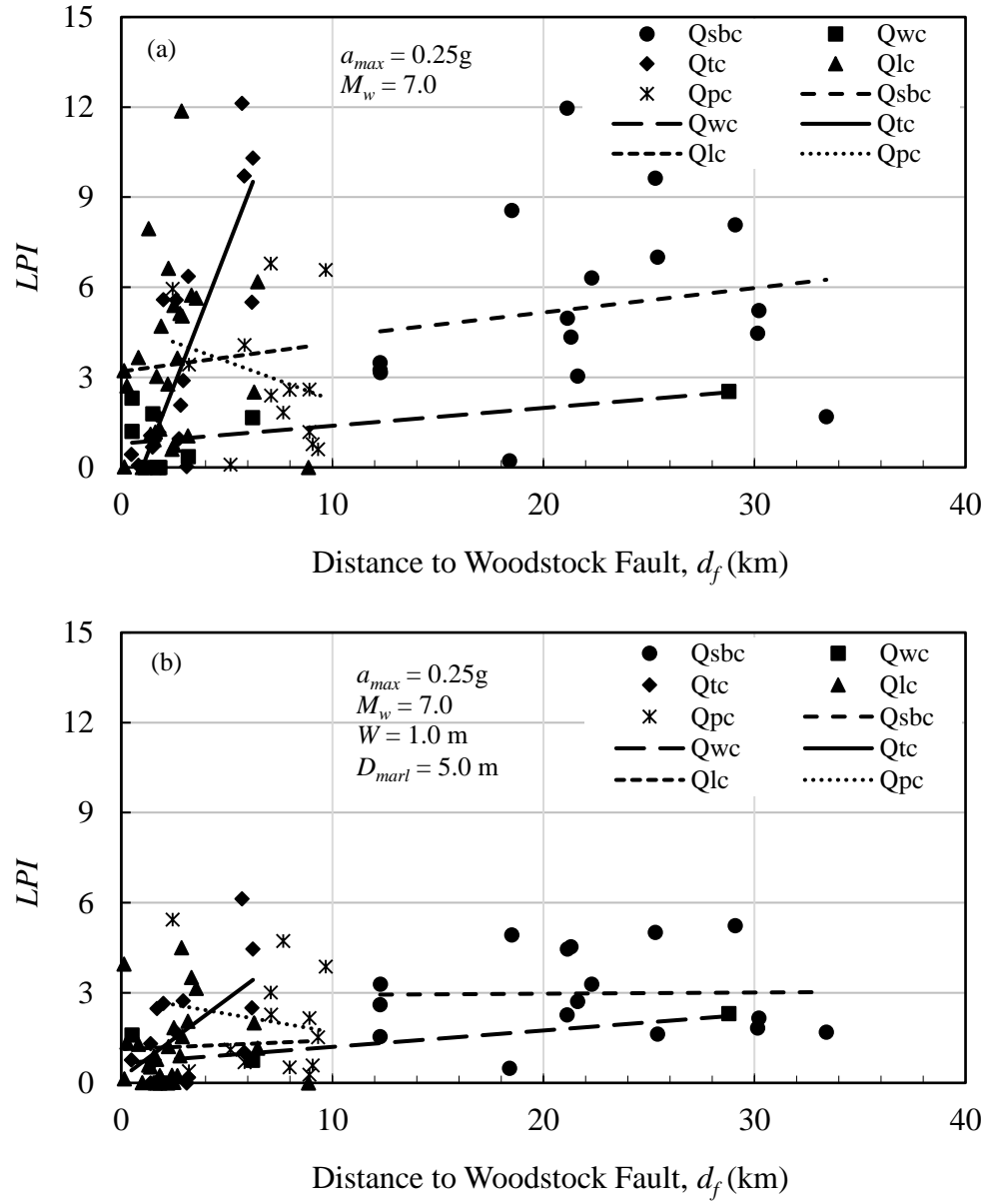


Figure 3.8 Combined plot of  $LPI$  versus distance to Woodstock fault for clayey soils under (a) site-specific conditions and (b) uniform conditions (i.e.,  $W = 1.0 \text{ m}$ ,  $D_{marl} = 5.0 \text{ m}$ ) based on constant earthquake loading (i.e.,  $a_{max} = 0.25g$ ,  $M_w = 7.0$ ).



Presented in Figure 3.9 is the relationship between  $LPI$  and distance to a perennial stream or river ( $d_s$ ), based on  $LPI$  calculated under (a) site-specific conditions, and (b) uniform conditions of groundwater (i.e.,  $W = 1.0$  m) and Cooper Marl (i.e.,  $D_{marl} = 5.0$  m). Two of the units, Qlc and Qwc, show an increase in  $LPI$  when SCPT sites are closer to a drainage channel, more noticeably in Figure 3.9a. This relationship suggests that fluvial deposition along the stream has affected the soil characteristics and liquefaction susceptibility of adjacent, coeval deposits within Qlc and Qwc. Such an impact could exist only within the influence zone of the stream. This zone is often defined by the width of the meander belt, a metric constrained by the floodplain area. The trend displayed in Figure 3.9 is based on values of  $d_s$  that would exceed the meander belt width for many of the nearby perennial streams. Yet, for SCPT sites near the Ashley, Cooper, Wando, and Stono Rivers, this influence may be valid and present. As part of this investigation, the few cases where  $d_s$  is the distance to the inside of a meander, versus outside or along a straight channel section, have also been considered, yielding no strong correlation.

Despite the relationship suggested for Qwc and Qlc, the other three units possess an opposing trend of increasing  $LPI$  with distance, even when the influence of groundwater and marl has been constrained, as in Figure 3.9b. Figure 3.9b also illustrates that as the behavior of the Quaternary deposit is considered independent of groundwater and marl, the value of  $LPI$  has a diminished response to changes in  $d_s$  (i.e., the trend lines flatten out). In light of these conflicting patterns and the scatter among the data, the overall consensus is that distance to stream has little to no effect on the magnitude of  $LPI$  for sites within this data set.

Viewing the units in Figure 3.9 in terms of their relative geologic age can also help assess the controls on liquefaction behavior. If the trend line for each unit is taken as a reflection of the average  $LPI$  value for a given  $d_s$ , Qsbc consistently plots above the other units in both Figures 3.9a and 3.9b. Qwc plots toward the bottom in Figure 3.9a, but when the depths to groundwater and marl are kept uniform, the units of Qwc, Qtc, Qlc, and Qpc overlap one another at low values of  $LPI$ . This suggests there is little to no influence of deposit age on the relative susceptibility of the older clayey units after applying  $K_{DR} \neq 1.0$ .

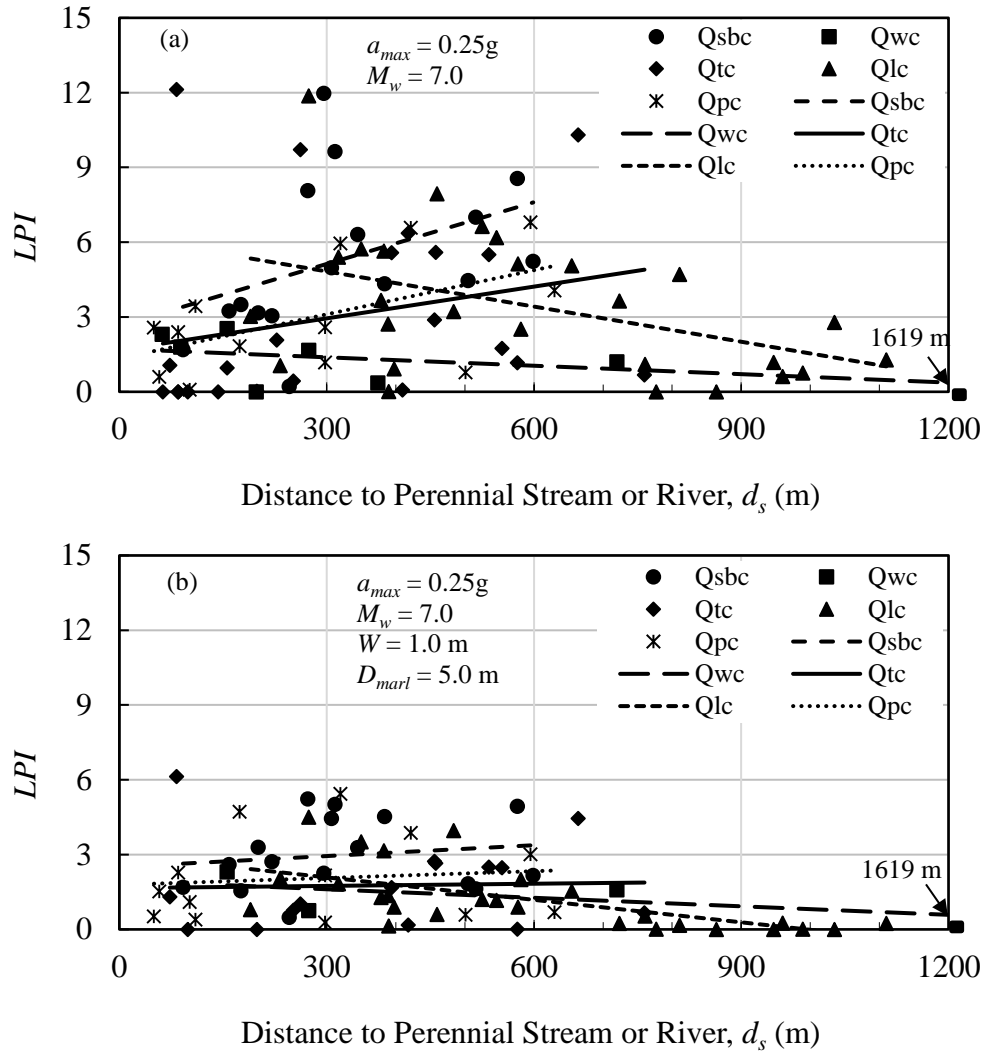


Figure 3.9 Combined plot of  $LPI$  versus distance to perennial stream for clayey soils under (a) site-specific conditions and (b) uniform conditions (i.e.,  $W = 1.0$  m,  $D_{marl} = 5.0$  m) based on constant earthquake loading (i.e.,  $a_{max} = 0.25g$ ,  $M_w = 7.0$ ).

Presented in Figure 3.10 are cumulative distribution function (*CDF*) curves for the five clayey units based on site-specific calculated values of *LPI*. Figure 3.10 shows that the clayey units have generally similar *LPI*-*CDF* relationships for the same constant earthquake loading. However, for each of the four older units, 60% of the sites are predicted to have *LPI*s approximately equal to or less than 3.5. Yet at 60% of the sites in Qsbc, the curve predicts an *LPI* value around 5.5. Even though these *LPI* values are below the weighted thresholds, the differences in *CDF* for each unit reflect the higher susceptibility associated with Qsbc. As the cumulative distribution exceeds 60%, the curves tend toward each other, with the exception of Qwc which continues to predict lower *LPI* values than the other units.

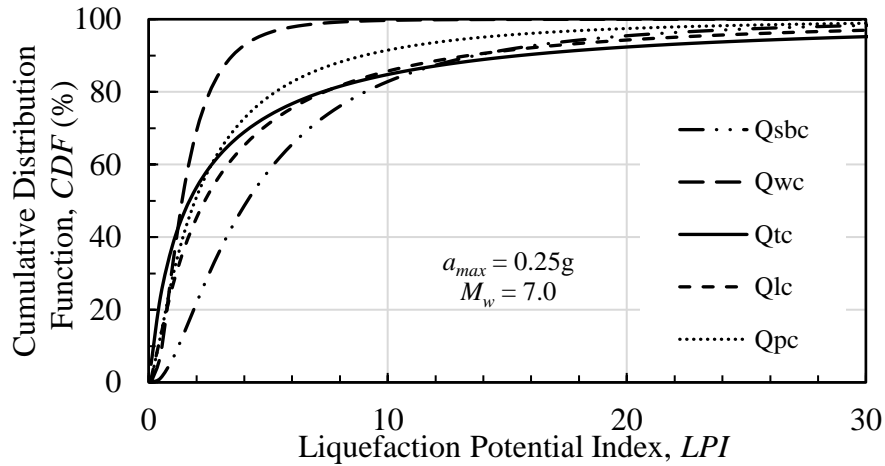


Figure 3.10 *CDF* curves for *LPI* values of Qsbc, Qwc, Qtc, Qlc, and Qpc based on constant earthquake loading (i.e.,  $a_{max} = 0.25g$ ,  $M_w = 7.0$ ) and site-specific conditions.

Presented in Figure 3.11 are box-and-whisker plots of *LPI* for the five clayey units. Plots are included for both (a) site-specific conditions of groundwater and marl, and (b) where the influence of groundwater and marl has been set to constant values (i.e.,  $W = 1.0$  m and  $D_{marl} = 5.0$  m). Overall, the five units have common ranges of *LPI*, reaching from 0 to 12 in Figure 3.11a and from 0 to 6 in Figure 3.11b. Mean and median *LPI* values are also comparably low across units with respect to their weighted *LPI* threshold. These statistics are tabulated in Tables 3.3 and 3.4, for plots (a) and (b), respectively. The younger Qsbc clayey facies were found to have slightly higher mean and median *LPI* values in both cases, although the sample standard deviation is also one of the highest. The mean and median for Qwc are some of the lowest under both conditions. Qwc also has the smallest standard deviation, despite the limited sample size. Qtc, Qlc, and Qpc appear to have similar statistics in between those of Qsbc and Qwc. Although, it is noted that Qlc revealed the most drastic changes between plots (a) and (b), with respect to its standing among the other units. This suggests that the deposits in Qlc exhibit the greatest influence from groundwater and marl conditions out of the five clayey units.

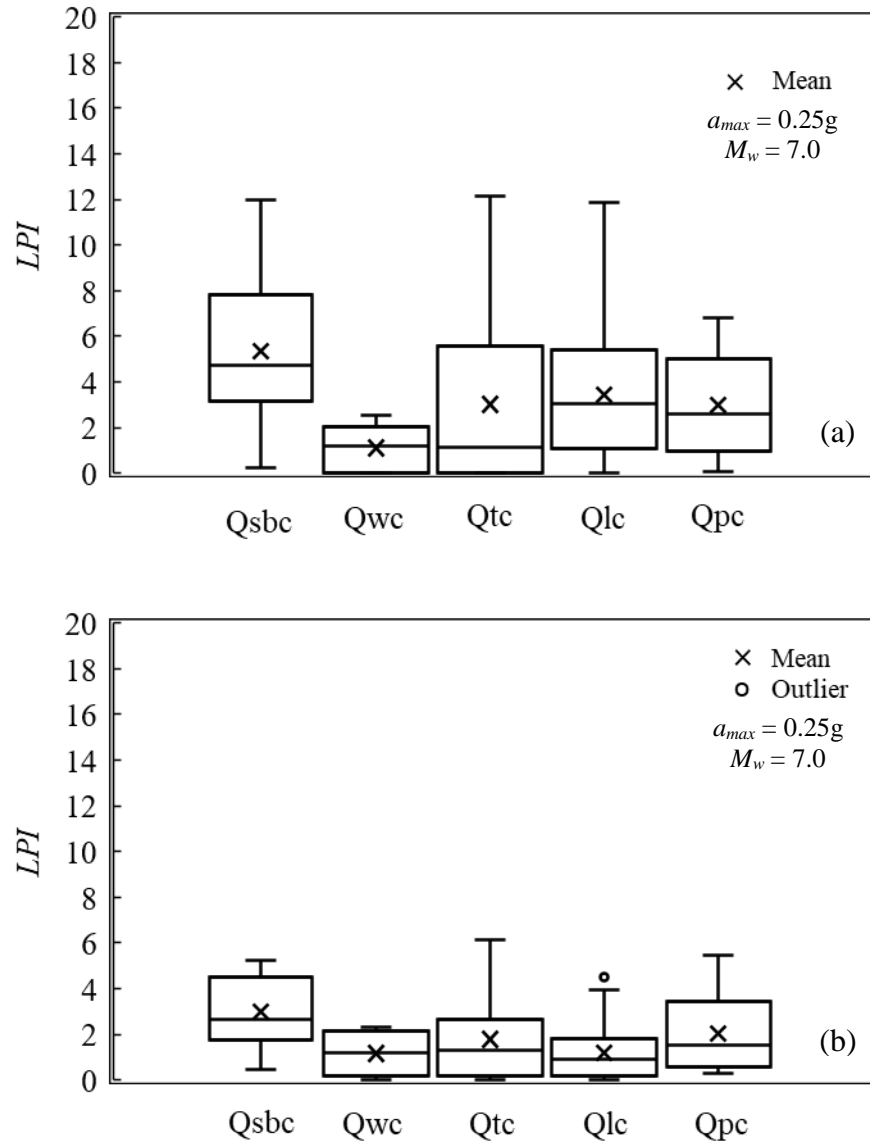


Figure 3.11 Box-and-whisker plots of  $LPI$  values based on constant earthquake loading (i.e.,  $a_{max} = 0.25g$  and  $M_w = 7.0$ ), obtained assuming (a) site-specific conditions, and (b) where the depth to water table = 1 m and depth to marl = 5 m.

Table 3.3 *LPI* statistics for five clayey deposits assuming a constant earthquake loading of  $a_{max} = 0.25g$  and  $M_w = 7.0$ . Based on site-specific depths of groundwater and Cooper Marl.

Surface Geology	Mean <i>LPI</i>	Median <i>LPI</i>	Standard Deviation	<i>n</i>
Qsbc	5.3	4.3	3.1	16
Qwc	1.1	1.2	1.0	9
Qtc	3.0	1.1	3.8	21
Qlc	3.4	3.0	2.8	27
Qpc	3.0	2.6	2.3	13

Table 3.4 *LPI* statistics for five clayey deposits assuming a constant earthquake loading of  $a_{max} = 0.25g$  and  $M_w = 7.0$ . Based on a depth to groundwater of 1 m and a depth to Cooper Marl of 5 m.

Surface Geology	Mean <i>LPI</i>	Median <i>LPI</i>	Standard Deviation	n
Qsbc	3.0	2.7	1.5	16
Qwc	1.2	1.2	1.0	4
Qtc	1.8	1.3	1.8	15
Qlc	1.2	0.9	1.3	27
Qpc	2.0	1.5	1.7	13

### **3.7 Liquefaction Probability Curves for Regional Hazard Mapping**

Shown in Figure 3.12 are liquefaction probability curves for Qsbc, Qwc, Qtc, Qlc, and Qpc. They are based on results of  $LPI$  calculations performed on the SCPT and SCPTu profiles as outlined in Chapter 2, assuming a lognormal distribution. These curves were generated assuming depths to groundwater and Cooper Marl that are specific to each site. As mentioned in Chapter 2, an important modification to the methodology for generating liquefaction probability curves (Holzer et al. 2006; Rix and Romero-Hudock 2007) is the assumed  $LPI$  threshold ( $LPI_t$ ). Based on  $I_{c10}$  values computed from each profile, the  $LPI_t$  for each unit is 15 for Qsbc, 14 for Qwc, 14 for Qtc, 15 for Qlc, and 15.5 for Qpc. Table 3.5 provides a range of  $I_{c10}$  values and the assumed  $LPI_t$  for the profiles in this dataset.

The probability curve for Qsbc plots well above the four older deposits, which together form a narrow band of roughly parallel curves. The curves appear to generally order themselves in terms of age. This would reflect an overall decrease in liquefaction potential as the geologic age of the deposit increases. An exception to this is the curve for Qwc, which lies immediately above the Qpc curve instead of between Qsbc and Qtc. The influence of  $LPI_t$  on these curves tends to yield lower probability curves for higher threshold values. Given the range of these threshold values is small, the influence of  $LPI_t$  is minimal for the given data.

In view of the commonality among the curves for the four older deposits, a single probability curve combining the data for Qwc, Qtc, Qlc, and Qpc has also been provided, as shown in Figure 3.13. Upon inspection, the single curve for the older deposits may appear higher than the anticipated average, based on the four individual curves in Figure 3.12. The location of the average curve with respect to the four older units is due largely to the influence of  $LPI_t$ . The  $I_{c10}$  values of the combined units collectively indicate that  $LPI_t = 14$  for data plotting in Qwc, Qtc, Qlc, and Qpc. This pulls the single curve upward toward the original curves for Qtc ( $LPI_t = 14$ ) and Qlc ( $LPI_t = 15$ ), which units had the highest number of individual data points. The combined curve and the curve for Qsbc are considered suitable for mapping application.

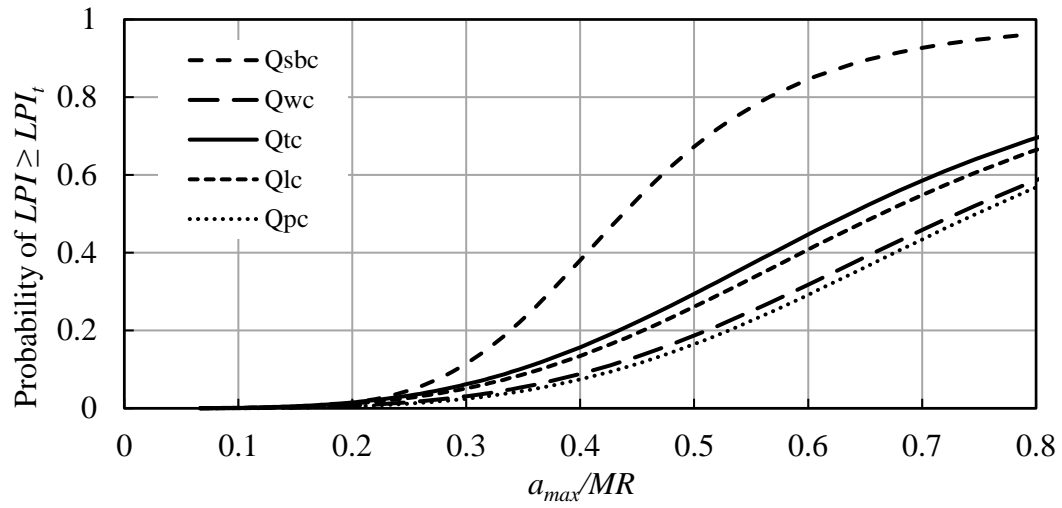


Figure 3.12 Liquefaction probability curves for Qsbc, Qwc, Qtc, Qlc, and Qpc based on site-specific conditions of groundwater and Cooper Marl.

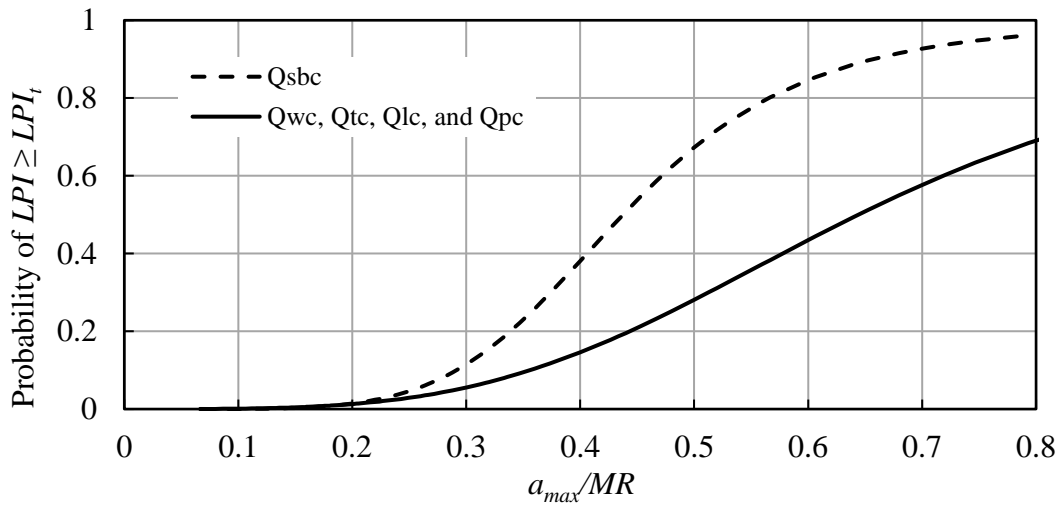


Figure 3.13 Liquefaction probability curve for Qsbc, and a single curve for Qwc, Qtc, Qlc, and Qpc, based on site-specific conditions of groundwater and Cooper Marl.

When the ratio of  $a_{max}/MR = 0.8$ , the probability curves in Figure 3.13 predict that less than 70% of the area covered by Qwc, Qtc, Qlc, and Qpc will exceed the assigned threshold, while 96% of the area covered by Qsbc will exceed the threshold. Exceeding  $LPI_t$  corresponds to the occurrence of surface manifestations of liquefaction.

The probability curves presented in Figures 3.12 and 3.13 are defined by:

$$P_{LPI \geq LPI_t} = 1 / (1 + [(a_{max} / MR) / a]^b) \quad (5)$$

where  $a$  and  $b$  are curve-fitting parameters. The values of  $(a, b)$  for Qsbc, Qwc, Qtc, Qlc, and Qpc in Figure 3.12 are (0.438, -5.409), (0.731, -3.872), (0.637, -3.620), (0.664, -3.672), and (0.747, -4.036), respectively. In Figure 3.13, the parameter values for Qsbc are the same. However, the values of  $(a, b)$  for the single curve for Qwc, Qtc, Qlc, and Qpc are (0.644, -3.709).

Table 3.5 Range of  $I_{c10}$  values and assumed  $LPI_t$  for surficial clayey deposits.

Surface Geology	Minimum value $I_{c10}$	Maximum value $I_{c10}$	Average $I_{c10}$	$LPI_t$
Qsbc	2.00	3.14	2.38	15
Qwc	1.91	2.53	2.16	14
Qtc	1.88	2.72	2.24	14
Qlc	2.02	2.76	2.40	15
Qpc	2.27	2.69	2.48	15.5

The observations of disturbance along railroads discussed in Section 3.3 provide an estimate on the percentage of area covered by each unit that experienced damage related to liquefaction. These estimates are used here to verify the probability curves presented in Figure 3.13. Based on notes by Earle Sloan and W. J. McGee along the railway lines, approximately 6.1% of Qtc, 3.8% of Qlc, and 6.7% of Qpc experienced either minor to severe surface manifestations of liquefaction. No recorded observations of failures in Qsbc and Qwc were included in their notes. Table 3.6 presents an estimate of average earthquake loading along the railway lines within each unit. The approximate values of  $a_{max}$  are based on maps from Silva et al. (2003) assuming  $M_w = 7.3$ , and on a SHAKE analysis from Bwambale (2018) using  $V_s$  profiles from Qts. Using the approximate loading values indicated, Table 3.6 presents the predicted probability of  $LPI \geq LPI_t$  for clayey deposits, based on Figure 3.13. Under the given loading assumptions, the probabilities predicted by the curves over-estimate the actual percentage of rail lines with observed liquefaction for all units except Qpc, where the predicted and observed values coincide. Thus, the probability curves offer a conservative yet reasonable prediction for liquefaction occurrence in Qsbc, Qwc, Qtc, Qlc and Qpc.



Table 3.6 Comparison of observed liquefaction along railway lines versus predicted probability of  $LPI \geq LPI_t$  for clayey deposits.

Surface Geology	Distances from Rail Line to Fault (km)	Observed Minor to Severe Liquefaction Along Rail Line (%)	Approximate Loading		Probability of $LPI \geq LPI_t$ (%)
			$a_{max}$	$M_w$	
Qsbc	9.1 – 9.2	0.0	0.30	7.0	8.2
Qwc	2.2 – 19.0	0.0	0.32	7.0	5.5
Qtc	0.0 – 7.7	6.1	0.36	7.0	8.2
Qlc	0.0 – 3.9	3.8	0.38	7.0	9.9
Qpc	0.0 – 20.8	6.7	0.34	7.0	6.7

The fact that depth to groundwater and depth to Cooper Marl influence the calculated  $LPI$  values has been established in this chapter. The curves presented in Figures 3.12 and 3.13 are subject to this influence. However, the analysis for the five clayey deposits is extended here to eliminate this influence. The additional analysis consists of a series of model liquefaction probability curves, each pertaining to a given set of groundwater and Cooper Marl surface depths. The water table level varies at 2-m intervals from 0 to 10 meters below ground, in relevant combination with depths to top of Cooper Marl, which range from 2 to 12 meters at 2-m intervals. Curves have been generated specifically for Qsbc alone, as well as single curves for the combined units of Qwc, Qtc, Qlc, and Qpc. An example set of these curves is presented in Figure 3.14 for Qsbc, and in Figure 3.15 for the combined group of Qwc, Qtc, Qlc, and Qpc. Overall, the two sets of curves appear to be very similar, given their respective values of  $LPI_t$  (i.e., 15 for Qsbc, 14 for Qwc, Qtc, Qlc, and Qpc). Qsbc shows greater probability over the remaining units when the contribution from the top 2 m are included in the analysis. It is apparent that as the depth to groundwater increases while depth to marl remains the same, the probability of  $LPI$  reaching the threshold value for surface manifestations of liquefaction decreases. In all cases where depth to groundwater is located only 2 m above marl, the liquefaction potential is predicted to be near zero.

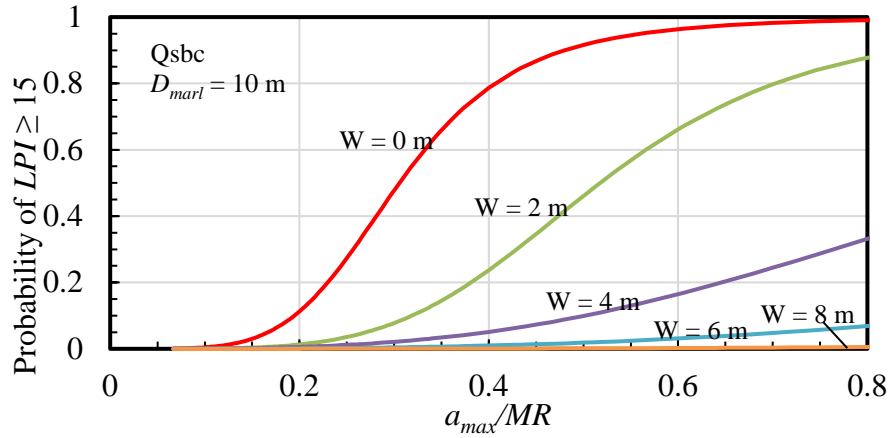


Figure 3.14 Liquefaction probability curves for  $Q_{sbc}$  assuming a depth to top of Cooper Marl of 10 m, and depths to groundwater ( $W$ ) of 0, 2, 4, 6, and 8 m.

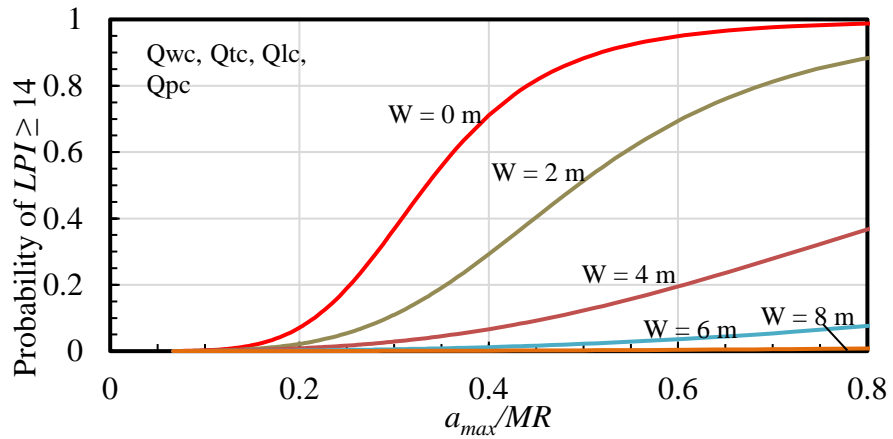


Figure 3.15 Liquefaction probability curves for  $Q_{wc}$ ,  $Q_{tc}$ ,  $Q_{lc}$ , and  $Q_{pc}$  assuming a depth to top of Cooper Marl of 10 m, and depths to groundwater ( $W$ ) of 0, 2, 4, 6, and 8 m.

Tables 3.7 and 3.8 present the parameter values associated with each curve, as well as the respective root-mean-square error (RMSE). The curves can be used in regional hazard mapping efforts for the clayey units included. Heidari (2011) and Bwambale (2018) created similar curves for areas covered by the Wando sand facies (Qws) and Ten Mile Hill sand facies (Qts), respectively. As shown in Table 3.7, curve-fitting parameter values for Qsbc corresponding to a marl depth of 12 m were not determined, which is due to a limited number of profiles at this depth.

Table 3.7 Curve-fitting parameter values for liquefaction probability curves, based on combinations of depth to groundwater and depth to marl within Qsbc.

Depth to top of Cooper Marl (m)	Depth to groundwater table (m)	Parameter <i>a</i>	Parameter <i>b</i>	RMSE
2	0	16.489	-6.830	0.008
4	0	0.894	-3.071	0.011
4	2	1.804	-4.182	0.001
6	0	0.536	-3.331	0.027
6	2	1.034	-3.337	0.010
6	4	3.037	-3.296	0.0003
8	0	0.389	-3.570	0.043
8	2	0.713	-3.512	0.028
8	4	1.599	-2.988	0.004
8	6	--*	--!	0.002
10	0	0.306	-4.861	0.029
10	2	0.518	-4.535	0.034
10	4	0.996	-3.203	0.010
10	6	1.964	-2.903	0.002
10	8	4.523	-3.002	0.0002

--\* = very high parameter value, indicating close to zero probability

--! = very low parameter value, indicating close to zero probability

Table 3.8 Curve-fitting parameter values for liquefaction probability curves, based on combinations of depth to groundwater and depth to marl within Qwc, Qtc, Qlc, and Qpc.

Depth to top of Cooper Marl (m)	Depth to groundwater table (m)	Parameter $a$	Parameter $b$	RMSE
2	0	5.080	-1.821	0.001
4	0	1.427	-2.502	0.005
4	2	2.804	-3.369	0.0004
6	0	0.711	-2.860	0.014
6	2	1.245	-2.848	0.007
6	4	3.615	-2.525	0.001
8	0	0.452	-3.531	0.022
8	2	0.727	-3.245	0.020
8	4	1.537	-2.827	0.005
8	6	3.771	-2.680	0.001
10	0	0.334	-5.014	0.013
10	2	0.494	-4.203	0.022
10	4	0.958	-3.029	0.011
10	6	2.002	-2.729	0.002
10	8	6.317	-2.348	0.0003
12	0	0.291	-5.162	0.013
12	2	0.430	-4.159	0.024
12	4	0.814	-2.930	0.015
12	6	1.512	-3.163	0.003
12	8	2.520	-2.890	0.001
12	10	--*	--!	0.001

--\* = very high parameter value, indicating close to zero probability

--! = very low parameter value, indicating close to zero probability

### **3.8 Conclusion**

The overall liquefaction susceptibility of five surficial clayey deposits in the greater Charleston area has been characterized in this chapter using 90 SCPT profiles from sites located 0 to 34 km from the Woodstock fault and assuming a constant ground shaking. Computed *LPI* values for the five units exhibited weak, conflicting correlations with distance to Woodstock fault and distance to perennial stream. Cumulative distributions of *LPI* values for a constant loading are similar for all five units, with Qwc showing less susceptibility, and Qsbc showing the most susceptibility until surpassing 60% of the data.

Liquefaction probability curves were expressed as a function of  $a_{max}/MR$  and a weighted threshold *LPI* at which surface manifestations occur, assuming the liquefaction triggering procedure of Boulanger and Idriss (2016). Qsbc exhibited the highest probability of liquefaction for a given  $a_{max}/MR$ , and the similar probabilities of the remaining four units justified a single curve to represent their collective probability. Results from the curves suggest an overall greater resistance to liquefaction with geologic age. One exception is Qwc, which has higher resistance despite being younger than three other clayey units in this study. This is likely due to lower groundwater tables and/or shallower depths to marl in the Qwc dataset. Thus, an additional set of model probability curves considering the influence of depth to Cooper Marl and depth to groundwater table were developed.

The deposit-specific probability curves agree well with observations of ground behavior during the 1886 Charleston earthquake, where ground failures were limited to a range within 15 km of the fault for the four oldest units, and within 24 km for Qsbc. The probability curves may be used to create regional hazard maps, but should not replace site-specific evaluations.

## CHAPTER FOUR

### SUMMARY, CONCLUSIONS, AND RECOMMENDATIONS

#### **4.1 Summary and Conclusions**

This report investigated the liquefaction susceptibility and the liquefaction potential of major surficial Quaternary deposits in the Charleston, South Carolina area. Liquefaction susceptibility was expressed in terms of the liquefaction potential index (*LPI*), computed from SCPT profiles assuming a constant earthquake loading (i.e.,  $a_{max} = 0.25g$ ,  $M_w = 7.0$ ). *LPI* was determined following the liquefaction triggering procedure of Boulanger and Idriss (2016). Liquefaction probability curves were generated based on probability of exceeding the *LPI* threshold for surface manifestations of liquefaction. The potential analysis also considered the major ground failures and railroad observations reported by Dutton (1889), which helped to verify the results of the analyses.

##### **4.1.1 Surficial Sand Deposits**

The overall liquefaction susceptibility of six surficial sand deposits in the greater Charleston area was characterized using 228 SCPT profiles from sites located 0 to 39 km from the Woodstock fault and assuming a constant ground shaking. Computed *LPI* values for five of the six units exhibited only slight increasing correlation with distance to the fault. Cumulative distributions of *LPI* values for a constant loading are similar for all six units with Qwls showing slightly less susceptibility.

Liquefaction probability curves were expressed as a function of  $a_{max}/MR$  and a weighted threshold *LPI* at which surface manifestations occur. Qhs exhibited the highest probability of liquefaction for a given  $a_{max}/MR$ , and Qwls and Qps exhibited the lowest probability. Qsbs, Qws, and Qts exhibit a similar probability to each other which is less than Qhs but greater than Qwls and Qps. These probability curves are shown to agree overall with the observations of ground failure following the 1886 earthquake, with varying degrees of conservatism.

##### **4.1.2 Surficial Clayey Deposits**

The overall liquefaction susceptibility of five surficial clayey deposits in the greater Charleston area was characterized using 90 SCPT profiles from sites located 0 to 34 km from the Woodstock fault and assuming a constant ground shaking. Computed *LPI* values for the five units exhibited weak, conflicting correlations with distance to Woodstock fault and distance to perennial stream. Cumulative distributions of *LPI* values for a constant loading are similar for all five units, with Qwc showing less susceptibility, and Qsbc showing greater susceptibility until the cumulative distribution exceeds 60%.

Liquefaction probability curves were expressed as a function of  $a_{max}/MR$  and a weighted threshold *LPI* at which surface manifestations occur. Qsbc exhibited the highest probability of liquefaction for a given  $a_{max}/MR$ , and the similar probabilities of the remaining four units justified a single curve being used to represent their collective probability. These probability curves are

generally conservative, yet in agreement with the observations of ground failure following the 1886 earthquake. Results from the curves suggest an overall greater resistance to liquefaction with geologic age. One exception is Qwc, which has higher resistance despite being younger than three other clayey units in this study. This is due, at least in part, to deeper groundwater tables and/or shallower depths to top of Cooper Marl within Qwc. Thus, the influence of depth to groundwater table and depth to Cooper Marl on liquefaction potential was established, and a set of model probability curves for specified conditions were provided for the four oldest clayey deposits.

#### **4.1.3 Relative Liquefaction Potential of Quaternary Deposits**

The values of computed *LPI* have led to the creation of liquefaction probability curves for each surface geologic unit considered in this study. Figure 4.1 presents a comparison of the liquefaction probability curves for all of the sand and clayey deposits. This comparison helps illustrate the greater liquefaction susceptibility associated with the sand facies, and puts in perspective the relative potential connected to each of the surface units displayed.

As evident in Figure 4.1, there is some overlap extending between the curves plotted in Figures 4.1a and 4.1b. Although Qsbc is classified as a clayey deposit, areas covered by Qsbc are predicted to have a greater percent of the area exceed the threshold for surface manifestations of liquefaction than Qps, at higher values of  $a_{max}/MR$ . However, below  $a_{max}/MR = 0.4$ , all of the sand deposits, including Qps, have a predicted probability of liquefaction higher than any of the clayey deposits presented.

The recorded observations of ground behavior after the 1886 earthquake generally agree with the calculated probabilities based on the curves shown in Figure 4.1. The railroad observations themselves show a greater percentage of disturbance within the sands than within the clayey units.

Regional hazard maps may be created based on the curves presented above, but these curves should not replace the necessary site-specific evaluations.

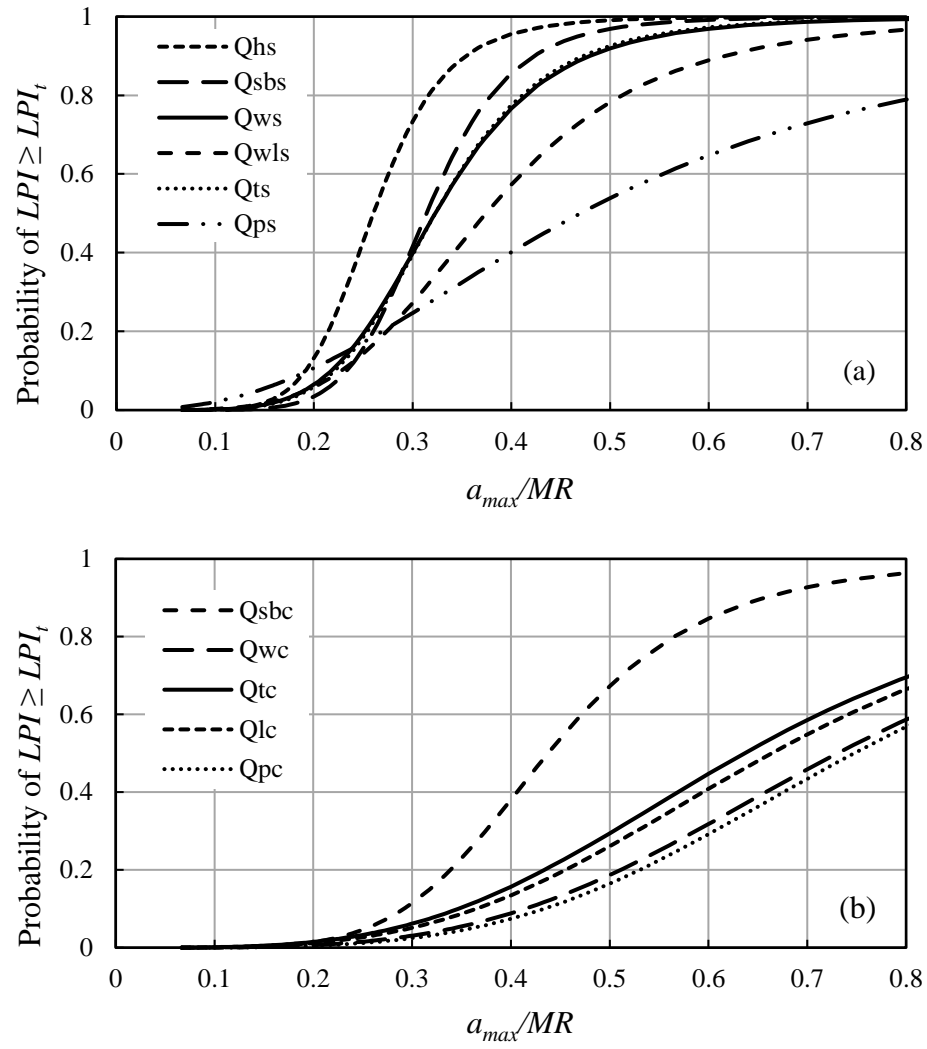


Figure 4.1 Liquefaction probability curves for surficial (a) sand deposits and (b) clayey deposits, assuming site-specific conditions of groundwater and marl.



## **4.2 Recommendations**

Based on the results presented in this report, the following are recommendations pertaining to future related work and the application of the research findings in this study. In all liquefaction potential assessments, careful efforts in the site investigation should be made for determining the depth below ground surface to the top of Cooper Marl. Likewise, careful efforts are needed in determining accurate groundwater table levels. These factors contribute significantly to the liquefaction behavior for all deposits considered in this study, assuming a given earthquake loading.

Further analysis of local and regional geomorphic features that may influence the extent of liquefaction evidence at a site is recommended. Analyses may consider variations in slope that would impact the degree and type of ground failure.

While the total number of SCPT profiles analyzed in this study well exceeds that of previous work in the Charleston area, several mapped surface deposits remain uncharacterized, including fluvial and marine shelf facies, as well as Qhm and Qht. In order to evaluate the liquefaction hazard associated with these units, it is recommended that more SCPT profiles be collected, particularly as urban development continues along the coast and near waterways. In the downhole  $V_s$  data reduction for the additional recommended SCPT profiles, the author recommends the use of the modified interval method (Equation 2.1) for more accurate interpretation of  $V_s$ , or the Snell's Law ray-path method where time permits.

## REFERENCES

- Amoly, R. S., Ishihara, K., and Bilsel, H. (2015). "Relations between liquefaction resistance and shear wave velocity as affected by aging of sand deposits." *Journal of Seismology and Earthquake Engineering*, 17(1), 19-30.
- Andrus, R. D., Hayati, H., and Mohanan, N. P. (2009). "Correcting liquefaction resistance for aged sands using measured to estimated velocity ratio." *Journal of Geotechnical and Geoenvironmental Engineering*, 135(6), 735-744.
- Bakun, W. H., and Hopper, M. G. (2004). "Magnitudes and locations of the 1811-1812 New Madrid, Missouri, and the 1886 Charleston, South Carolina, earthquakes." *Bulletin of the Seismological Society of America*, 94(1), 64-75.
- Balon, D. R., and Andrus, R. D. (2006). "Liquefaction potential index of soils in Charleston, South Carolina based on the 1886 Earthquake." *Proceedings of the 8th U.S. National Conference on Earthquake Engineering*, San Francisco, CA, Mira Digital Publishing, St. Louis, MO.
- Boller, Jr., R. C. (2008). "Geotechnical investigations at three sites in the South Carolina Coastal Plain that did not liquefy during the 1886 Charleston earthquake." *M.S. Thesis*, Clemson University, Clemson, SC.
- Boller, Jr., R. C., Andrus, R. D., Hayati, H., Camp, W. M., Gassman, S. L., and Talwani, P. (2008). "Liquefaction evaluation of the Coastal Research and Education Center geotechnical experimentation site near Charleston, South Carolina based on cone tests." *Proceedings of the 6th National Seismic Conference on Bridge and Highways, Seismic Technologies for Extreme Loads*, MCEER-08-SP04, held July 28-30 in Charleston, SC, MCEER, Buffalo, NY, Poster No. P23.
- Bollinger, G. (1977). "Reinterpretation of the intensity data for the 1886 Charleston, South Carolina, earthquake." *Studies Related to the Charleston, South Carolina, Earthquake of 1886: A Preliminary Report*, D. W. Rankin, ed., USGS Professional Paper 1028, U.S. Government Printing Office, Washington, DC, 17-32.
- Boulanger, R. W., and Idriss, I. M. (2006). "Liquefaction susceptibility criteria for silts and clays." *Journal of Geotechnical and Geoenvironmental Engineering*, 132(11), 1413-1426.
- Boulanger, R. W., and Idriss, I. M. (2016). "CPT-based liquefaction triggering procedure." *Journal of Geotechnical and Geoenvironmental Engineering*, 142(2).
- Bray, J. D., Sancio, R. B., Riemer, M. F., and Durgunoglu, T. (2004). "Liquefaction susceptibility of fine-grained soils." *Proceedings, 11th International Conference on Soil Dynamics and Earthquake Engineering and 3rd International Conference on Earthquake Geotechnical Engineering*, D. Doolin et al., eds., Stallion Press, Singapore, 655-662.

- Bwambale, B., and Andrus, R. D. (2017). "Liquefaction resistance of Pleistocene loess-colluvium deposits near Christchurch, New Zealand." *Proceedings, 3rd International Conference on Performance-based Design in Earthquake Geotechnical Engineering (PBD-III)*, Vancouver, Canada, Paper No. 206.
- Bwambale, B., and Andrus, R. D. (2018). "State of the art in the assessment of aging effects on soil liquefaction." *Research Report to Professor Yousef Bozorgnia*, University of California Berkeley Task Order Principal Investigator, Pacific Earthquake Engineering Research Center.
- Bwambale B., Andrus, R. D., and Cubrinovski, M. (2017). "Influence of age on liquefaction resistance of Holocene alluvial and marine soils in Christchurch and Kaiapoi, New Zealand." *Proceedings of the 3rd International Conference on Performance-based Design in Earthquake Geotechnical Engineering (PBD-III)*, Vancouver, Canada, July 16–19.
- Bwambale, B. (2018). "Reducing uncertainty in the assessment of aging effects on soil liquefaction." *Ph.D. Dissertation*, Clemson University, Clemson, SC.
- Chapman, M. C., and Talwani, P. (2002). "Seismic hazard mapping for bridge and highway design." *Report to the South Carolina Department of Transportation*, Columbia, SC.
- Chen, C. J., and Juang, C. H. (2000). "Calibration of SPT- and CPT-based liquefaction evaluation methods." *Innovations and Applications in Geotechnical Site Characterization, Geotechnical Special Publication No. 97*, P. W. Mayne and R. Hryciw, eds., ASCE, Reston, VA., 49-64.
- Colquhoun, D. J. (1974). "Cyclic surficial stratigraphic units of the Middle and Lower Coastal Plains, central South Carolina." In: Oaks, R. Q., Jr., and DuBar, J. R., (Eds.), *Post-Miocene stratigraphy, central and southern Atlantic Coastal Plain*, Logan, Utah, Utah State University Press, p. 179-190.
- Cooke, C. W. (1936). "Geology of the Coastal Plain of South Carolina." *U.S. Geological Survey, Bulletin 867*, 196 p.
- Côté, R. N. (2006). *City of Heroes: The Great Charleston Earthquake of 1886*. Corinthian Books, Mt. Pleasant, SC, 542 p.
- Cox, B. R. (2006). "Development of a direct test method for dynamically assessing the liquefaction resistance of soils in situ." *Ph.D. Dissertation*, University of Texas, Austin, TX.
- Cramer, C. H., Rix, G., and Tucker, K. (2008). "Probabilistic liquefaction hazard maps for Memphis, Tennessee." *Seismological Research Letters*, 79, 392-399.
- Cramer, C. H., Rogers, J. D., and Chung, J.-W. (2012). "Liquefaction hazard maps for the St. Louis area earthquake hazards mapping project: Collaborative Research with the Missouri University of Science and Technology and the University of Memphis." *Final Technical Report, U.S. Geological Survey, Award Nos. G11AP20124 and G11AP20125*, July 10, 2012, CERl, 29 p.

- Cramer, C. H., and Boyd, O. S. (2014). “Why the New Madrid earthquakes are M7–8 and the Charleston earthquake is ~M7.” *Bulletin of the Seismological Society of America*, 104(6), 2884.
- Durá-Gómez, I., and Talwani, P. (2009). “Finding faults in the Charleston area, South Carolina: 1. Seismological data.” *Seismological Research Letters*, 80(5), 883–900.
- Dutton, C. E., (1889). “The Charleston earthquake of August 31, 1886.” *Ninth Annual Report of the U.S. Geological Survey 1887-1888*, Washington, D.C., 203-528.
- Elton, D. J., and Hadj-Hamou, T. (1990). “Liquefaction potential map for Charleston, South Carolina.” *Journal of the Geotechnical Engineering Division*, ASCE, 116(2), 244-265.
- Esposito, M. P., III, Andrus, R. D., and Camp, W. M., III (2014). “Ground freezing and sampling of Pleistocene sand near Charleston, South Carolina.” *Journal of Geotechnical and Geoenvironmental Engineering*, ASCE, 140(1), 185–193.
- Fairbanks, C. D., Andrus, R. D., Zhang, J., Camp, W. M., Casey, T. J., and Clearly, T. J. (2004). “Electronic files of shear-wave velocity and cone penetration test measurements from the Charleston quadrangle, South Carolina.” *Data Report to the U. S. Geological Survey, Award No. 03HQGR0046*, Civil Engineering Department, Clemson University, Clemson, S.C.
- Franke, K. W., Ulmer, K. J., Ekstrom, L. T., and Meneses, J. F. (2016). “Clarifying the differences between traditional liquefaction hazard maps and probabilistic liquefaction reference parameter maps.” *Soil Dynamics and Earthquake Engineering*, 90(11), 240-249.
- Green, R. A., Cubrinovski, M., Cox, B., Wood, C., Wotherspoon, L., Bradley, B., and Maurer, B. (2014). “Select liquefaction case histories from 2010-2011 Canterbury earthquake sequence.” *Earthquake Spectra*, 30(1), 131-153.
- Hasek, M. J. (2016). “Age-related liquefaction resistance of Pleistocene coastal plain sands in South Carolina.” *Ph.D. Dissertation*, University of South Carolina, Columbia, SC.
- Hatanaka, M., and Masuda, T. (2008). “Experimental study on the relationship between degree of saturation and P-wave velocity in sandy soils.” *Proceedings, 2nd International Conference on Geotechnical Engineering for Disaster Mitigation and Rehabilitation*, H. Liu, A. Deng, and J. Chu, eds., Science Press, Beijing, 346-351.
- Hayati, H., and Andrus, R. D. (2008a). “Liquefaction potential map of Charleston, South Carolina based on the 1886 earthquake.” *Journal of Geotechnical and Geoenvironmental Engineering*, 134(6), 815–828.
- Hayati, H., and Andrus, R. D. (2008b). “Liquefaction susceptibility of fine-grained soils in Charleston, South Carolina based on CPT.” In: Reddy, K.R., Khire, M.V., Alshawabkeh, A.N. (Eds.), *Proceedings of GeoCongress 2008, Geosustainability and Geohazard Mitigation, Geotechnical Special Publication No. 178*, ASCE, Reston, VA, pp. 327–334.

- Hayati, H., and Andrus, R. D. (2009). "Updated liquefaction resistance correction factors for aged sands." *Journal of Geotechnical and Geoenvironmental Engineering*, 135(11), 1683–1692.
- Heidari, T., and Andrus, R. D. (2010). "Mapping Liquefaction Potential of Aged Soil Deposits in Mount Pleasant, South Carolina." *Engineering Geology*, 112(1-4), 1- 12.
- Heidari, T. (2011). "Characterizing liquefaction potential of Pleistocene soil deposits in the Charleston area, South Carolina." *Ph.D. Dissertation*, Clemson University, Clemson, SC.
- Heidari, T., and Andrus, R. D. (2012). "Liquefaction potential assessment of Pleistocene beach sands near Charleston, South Carolina." *Journal of Geotechnical and Geoenvironmental Engineering*, 138(10), 1196-1208.
- Holzer, T. L., Bennett, M. J., Noce, T. E., Padovani, A. C., and Tinsley, J. C. (2006). "Liquefaction hazard mapping with LPI in the greater Oakland, California, area." *Earthquake Spectra*, 22(3), 693–708.
- Holzer, T. L., Noce, T. E., and Bennett, M. J. (2009). "Scenario liquefaction hazard maps of Santa Clara Valley, Northern California." *Bulletin of the Seismological Society of America*, 99(1), 367-381.
- Holzer, T. L., Noce, T. E., and Bennett, M. J. (2011). "Liquefaction probability curves for surficial geologic deposits." *Environmental and Engineering Geoscience*, 17(1), 1-21.
- Hossain, M. A., Andrus, R. D., and Camp, W. M. (2013). "Correcting liquefaction resistance of unsaturated soil using wave velocity." *Journal of Geotechnical and Geoenvironmental Engineering*, 139(2), 277-287.
- Hossain, A. M., Geiger, A. J., Andrus, R., Hayati, H., Aboye, S. A., Esposito, M. P., III, and Heidari, T. (2014). "In situ seismic crosshole testing of six natural sand deposits in the South Carolina coastal plain." *Proceedings of the 2014 Geo-Congress: Geo-Characterization and Modelling for Sustainability*, ASCE, Reston, VA, 1142–1156.
- Idriss, I., and Boulanger, R. W. (2008). *Soil Liquefaction during Earthquakes*, Earthquake Engineering Research Institute Publication MNO-12, Oakland, CA.
- Iwasaki, T., Tatsuoka, F., Tokida, K.-I., and Yasuda, S. (1978). "A practical method for assessing soil liquefaction potential based on case studies at various sites in Japan." *Proceedings of the 2nd International Conference on Microzonation*, National Science Foundation, Washington, DC, 885–896.
- Iwasaki, T., Arakawa, T., and Tokida, K. (1982). "Simplified procedures for assessing soil liquefaction during earthquakes." *Proceedings, Conference on Soil Dynamics and Earthquake Engineering*, Southampton, UK, 925-939.

- Juang, C. H., Chen, C. J., and Jiang, T. (2001). "Probabilistic framework for liquefaction potential by shear wave velocity." *Journal of Geotechnical and Geoenvironmental Engineering*, 127(8), 670-678.
- Juang, C. H., and Li, D. K. (2007). "Assessment of liquefaction hazards in Charleston quadrangle, South Carolina." *Engineering Geology*, 92(1-2), 59-72.
- Kim, D. S., Bang, E. S., and Kim, W. C. (2004). "Evaluation of various downhole data reduction methods for obtaining reliable Vs profiles." *Geotechnical Testing Journal*, 27(6), 585-597.
- Kiyota, T., Koseki, J., Sato, T., and Kuwano, R. (2009). "Aging effects on small strain shear moduli and liquefaction properties of in-situ frozen and reconstituted sandy soils." *Soils and Foundations*, 49(2), 259-274.
- Kokusho, T., Nagao, Y., Ito, F., and Fukuyama, T. (2012). "Aging effect on sand liquefaction observed during the 2011 earthquake and basic laboratory studies." *Proceedings, International Symposium on Engineering Lessons Learned from the 2011 Great Japan Earthquake*, Tokyo, Japan, 759-770.
- Kramer, S. L. (1996). *Geotechnical Earthquake Engineering*, Prentice Hall, Upper Saddle River, NJ, pp. 207-208.
- Leon, E., Gassman, S., and Talwani, P., (2006). "Accounting for soil aging when assessing liquefaction potential." *Journal of Geotechnical and Geoenvironmental Engineering*, 132(3), 363-377.
- Lenz, J. A., and Baise, L. G. (2007). "Spatial variability of liquefaction potential in regional mapping using CPT and SPT data." *Soil Dynamics and Earthquake Engineering*, 27(7), 690-702.
- Li, D. K., Juang, C. H., Andrus, R. D., and Camp, W. M. (2007). "Index properties-based criteria for liquefaction susceptibility of clayey soils: a critical assessment." *Journal of Geotechnical and Geoenvironmental Engineering*, 133(1), 110-115.
- Lunne, T., Robertson, P. K., and Powell, J. J. M. (1997). *Cone penetration testing in geotechnical practice*. Blackie Academic, EF Spon/Routledge, New York.
- Martin, G. K., and Mayne, P. W. (1997). "Seismic flat dilatometer tests in Connecticut Valley varved clay." *Geotechnical Testing Journal*, Vol. 20, No. 3, pp. 357-361.
- Maurer, B. W., Green, R., Cubrinovski, M., and Bradley, B. A. (2014). "Assessment of aging correction factors for liquefaction resistance at sites of recurrent liquefaction." *Proceedings, 10th National Conference in Earthquake Engineering*, Earthquake Engineering Research Institute, Anchorage, AK.
- Maurer, B. W., Green, R., Cubrinovski, M., and Bradley, B. A. (2015a). "Fines-content on liquefaction hazard evaluation in Christchurch, New Zealand." *Soil Dynamics and Earthquake Engineering*, 76, 58-68.

- Maurer, B. W., Green, R. A., and Taylor, O. S. (2015b). "Moving towards an improved index for assessing liquefaction hazard: Lessons from historical data," *Soils and Foundations*, 55(4), 778-787.
- Mohanan, N. P., Fairbanks, C. D., Andrus, R. D., Camp, W. M., Clearly, T. J., Casey, T. J., and Wright, W. B. (2006). "Electronic files of shear wave velocity and cone penetration test measurements from the Greater Charleston area, South Carolina." *Data Report to the U.S. Geological Survey, Award No. 05HQGR0037*, Civil Engineering Department, Clemson University, Clemson, SC.
- Nuttli, O. W., Bollinger, G. A., and Herrmann, R. B. (1986). "The 1886 Charleston earthquake – A 1986 perspective." *Circular 985*, U.S. Geological Survey, Washington, D.C.
- Okamura, M., Ishihara, M., and Tamura, K. (2006). "Degree of saturation and liquefaction resistances of sand improved with sand compaction pile." *Journal of Geotechnical and Geoenvironmental Engineering*, 132(2), 258-264.
- Peters, K. E., and Herrmann, R. B., editors, (1986). "First-hand observations of the Charleston earthquake of August 31, 1886, and other earthquake materials." *Bulletin 41 of the South Carolina Geological Survey*, Columbia, SC.
- Petersen, M. D., Moschetti, M. P., Powers, P. M., Mueller, C. S., Haller, K. M., Frankel, A. D., Zeng, Y., Rezaeian, S., Harmsen, S. C., Boyd, O. S., Field, N., Chen, R., Rukstales, K. S., Luco, N., Wheeler, R. L., Williams, R. A., and Olsen, A. H., (2014). "Documentation for the 2014 update of the United States national seismic hazard maps." *U.S. Geological Survey Open-File Report 2014-1091*, 243 p.
- Rix, G. J., and Romero-Hudock, S. (2007). "Liquefaction potential mapping in Memphis and Shelby County, Tennessee." *Report to the U. S. Geological Survey*, Denver, CO.
- Robertson, P. K., and C. E. Wride. (1998). "Evaluating cyclic liquefaction potential using the cone penetration test." *Canadian Geotechnical Journal*, 35(3), 442–459.
- Seed, H. B. (1979). "Soil liquefaction and cyclic mobility evaluation for level ground during earthquakes." *Journal of Geotechnical Engineering Division*, 105(2), 201-255.
- Seed, H. B., and Idriss I. M. (1971). "Simplified procedure for evaluating soil liquefaction potential." *Journal of the Soil Mechanics and Foundation Division*, 97(9), 1249-1273.
- Seed, H. B., and Idriss, I. M. (1982). *Ground motions and soil liquefaction during earthquakes*, Earthquake Engineering Research Institute Monograph, Oakland, CA.
- Silva, W., Wong, I., Siegel, T., Gregor, N., Darragh, R., and Lee, R. (2003). "Ground motion and liquefaction simulation of the 1886 Charleston, South Carolina, Earthquake." *Bulletin of the Seismological Society of America*, 93(6), 2717-2736.
- Simonson, L. A. (2012). "Geology-based probabilistic liquefaction potential mapping of the 7.5-minute Charleston quadrangle, South Carolina for resilient infrastructure design." *M.S. Thesis*, Clemson University, Clemson SC.

- Talwani, P., and Schaeffer, W. T. (2001). "Recurrence rates of large earthquakes in the South Carolina Coastal Plain based on paleo-liquefaction data." *Journal of Geophysical Research*, 106, 6621-6642.
- Talwani, P., and Gassman, S. L. (2008). "The use of paleoliquefaction features in seismic hazard assessment – the Charleston experience." *Proceedings, 6th National Seismic Conference on Bridge and Highways, Seismic Technologies for Extreme Loads*, MCEER-08-SP04, Charleston, SC, MCEER, Buffalo, NY, Poster No. P30.
- Toprak, S., and Holzer, T. L. (2003). "Liquefaction potential index: Field assessment." *Journal of Geotechnical and Geoenvironmental Engineering*, 129(4), 315-322.
- van Ballegooy, S., Malan, P. J., Jacka, M. E., Lacrosse, V. I. M. F., Leeves, J. R., and Lyth, J. E. (2012). "Methods for characterising effects of liquefaction in terms of damage severity." *Proceedings, 15th world conference of earthquake engineering*, Lisbon, Portugal.
- Weems, R. E., and Lemon, E. M., Jr. (1988). "Geologic map of the Ladson quadrangle, Berkeley, Charleston, and Dorchester Counties, South Carolina." *U.S. Geological Survey Geologic Quadrangle, Map GQ-1630, scale 1:24,000, text*, U.S. Geological Survey, Reston, VA.
- Weems, R. E., and Lemon, E. M., Jr. (1993). "Geology of the Cainhoy, Charleston, Fort Moultrie, and North Charleston quadrangles, Charleston and Berkeley counties, South Carolina." *U.S. Geological Survey Miscellaneous Investigation Map I-1935, Scale 1:24,000*, U.S. Geological Survey, Reston, VA.
- Weems, R. E., Lemon, E. M., Jr., and Nelson, M. S. (1997). "Geology of the Pringletown, Ridgeville, Summerville, and Summerville Northwest 7.5-minute quadrangles, Berkeley, Charleston, and Dorchester counties, South Carolina." *U.S. Geological Survey Miscellaneous Investigations Map 2502, Scale 1:24,000*.
- Weems, R. E., Lewis, W. C., and Lemon, E. M., Jr. (2014). "Surficial geologic map of the Charleston region, Berkeley, Charleston, Colleton, Dorchester, and Georgetown Counties, South Carolina." *U.S. Geological Survey Open-File Report 2013-1030, scale 1:100,000*. U.S. Geological Survey, Reston, VA.
- Whitman, R. V. (1971). "Resistance of soil to liquefaction and settlement." *Soils and Foundations*, 11(4), 59–68.
- Wong, I., Bouabid, J., Graf, W., Huyck, C., Porush, A., Silva, W., Siegel, T., Bureau, G., Eguchi, R., and Knight, J. (2005). "Potential losses in a repeat of the 1886 Charleston, South Carolina, earthquake." *Earthquake Spectra*, November 2005, Vol. 21, No. 4, pp. 1157–1184.
- Youd, T. L., and Hoose, S. N. (1977). "Liquefaction susceptibility and geologic setting." *Proceedings, 6th World Conference on Earthquake Engineering*, New Delhi, India, 6, 37-42.



- Youd, T. L., and Perkins, D. M. (1978). "Mapping of liquefaction induced ground failure potential." *Journal of Geotechnical Engineering Division*, 104(4), 433-446.
- Youd, T. L., Idriss, I. M., Andrus, R. D., Arango, I., Castro, G., Christian, J. T., Dobry, R., Finn, W. D. L., Harder, L. F., Hynes, M. E., Ishihara, K., Koester, J. P., Liao, S. C. C., Marcuson, W. F., III, Martin, G. R., Mitchell, J. K., Moriwaki, Y., Power, M. S., Robertson, P. K., Seed, R. B., and Stokoe, K. H., III (2001). "Liquefaction resistance of soils: Summary report from the 1996 NCEER and 1998 NCEER/NSF Workshops on Evaluation of Liquefaction Resistance of Soils." *Journal of Geotechnical and Geoenvironmental Engineering*, 127, 817–833.
- Zhang, J., Andrus, R. D., and Juang, C. H. (2005). "Normalized shear modulus and material damping ratio relations." *Journal of Geotechnical and Geoenvironmental Engineering*, 131(4), 453-464.
- Zhang, J., Andrus, R. D., and Juang, C. H. (2008). "Uncertainty in normalized shear modulus and damping relations." *Journal of Geotechnical and Geoenvironmental Engineering*, 134(1), 24-36.
- Zhang, G., Robertson, P. K., and Brachman, R. W. I. (2002). "Estimating liquefaction induced ground settlements from CPT for level ground." *Canadian Geotechnical Journal*, 39(5), 1168–1180.

## **APPENDICES**

## **APPENDIX A**

### **SUMMARY OF SCPT DATABASE FOR SAND AND CLAYEY UNITS**

The Clemson University Site Code designates the surface geology and site number within this database. The Performing Organization Project Code begins with one letter that represents the organization performing the test: U = U.S. Geological Survey (USGS); W = WPC, Inc.; S = S&ME, Inc.; and T = Terracon Consultants, Inc. The two numbers following the test organization letters represent the year the test was conducted. The remaining numbers and letters represent the project number and the cone sounding/boring location. If an additional identifier is needed for projects with similar codes, a letter has been included at the end of the project number to be used in distinguishing between project locations. For example, the Site code S02522-B4 refers to a test made by S&ME, Inc. in 2002 for project number 522 at boring location B4. In the case of data obtained from the USGS, the three letters following the organization letter indicate that the test was performed in either the Charleston (CHN) or Berkeley (BKY) quadrangle, and the remaining numbers represent the test site. Project codes beginning with B96 were part of an investigation by Hu et al. (2002) in the Ten Mile Hill sands, and were also analyzed by Heidari and Andrus (2012).

Table A-1. Summary of SCPT and SCPTu data used in analysis of sand deposits.

CU Site Code	Performing Organization Project Code	Latitude	Longitude	Ground Surface Elev. (m)	Max Test Depth (m)	Water Table Depth (m)	Depth to Top of Cooper Marl (m)
Qhs1	UCHN001	32.78739929	-79.78997040	3.60	20.3	N/A	15.0
Qhs2	UCHN002	32.80298996	-79.74799347	3.00	20.3	N/A	13.9
Qhs3	UCHN003	32.79872131	-79.76293182	2.10	20.3	N/A	14.3
Qhs4	UCHN004	32.79533005	-79.77385712	0.30	20.3	N/A	> 20.0
Qhs5	UCHN005	32.78377152	-79.79881287	2.10	20.3	N/A	> 20.0
Qhs6†	UCHN024	32.76919937	-79.81861115	2.10	20.0	N/A	> 20.0
Qhs7	UCHN025	32.77659988	-79.81453705	0.90	20.1	N/A	≥ 20.0
Qhs8	UCHN026	32.78083038	-79.80509186	4.30	13.8	N/A	> 20.0
Qhs9	UCHN027	32.76020050	-79.85701752	3.00	20.1	N/A	> 20.0
Qhs10	UCHN028	32.75968933	-79.84279633	2.10	20.2	N/A	15.0
Qhs11	UCHN039	32.59072113	-80.12827301	3.00	11.8	N/A	> 17.5
Qhs12	UCHN042	32.62453079	-80.05644989	3.60	19.8	N/A	> 20.0
Qhs13	UCHN043	32.61783981	-80.01840210	0.90	19.8	N/A	13.0
Qhs14	UCHN044	32.61359024	-80.04904175	4.30	19.8	N/A	18.3
Qhs15	UCHN045	32.61064148	-80.06033325	6.10	19.9	N/A	> 20.0
Qhs16	UCHN052	32.56167984	-80.17742920	2.10	19.8	N/A	≥ 20.0
Qhs17	UCHN053	32.57001877	-80.15833283	0.00	19.9	N/A	18.4
Qhs18†	UCHN054	32.67356873	-79.94523621	1.80	19.9	N/A	> 20.0
Qhs19	UCHN055	32.65375900	-79.94956970	3.00	20.0	N/A	19.0?
Qhs20	UCHN056	32.64870071	-79.96074677	0.90	19.9	N/A	19.0?
Qhs21	UCHN057	32.65689087	-79.94326019	4.90	20.3	N/A	20.0?
Qhs22	UCHN058	32.66270828	-79.92707825	4.30	16.8	N/A	> 17.0
Qhs23	UCHN061	32.66772080	-79.91929627	1.80	19.9	N/A	> 20.0
Qhs24	UCHN062	32.67578888	-79.90177155	2.10	19.9	N/A	≥ 20.0
Qhs25	UCHN063	32.68334961	-79.89150238	0.90	19.9	N/A	20.0?
Qhs26	UCHN070	32.58919144	-80.15154266	4.90	19.8	N/A	16.4
Qhs27	UCHN071	32.57775116	-80.16752625	4.90	20.0	N/A	16.2
Qhs28	UCHN072	32.57233048	-80.17854309	2.10	17.4	N/A	> 17.5
Qhs29	UCHN073	32.57526016	-80.17120361	4.90	19.3	N/A	16.4
Qhs30	UCHN076	32.66210938	-79.93527985	4.00	19.8	N/A	≥ 20.0
Qhs31*	W04204-S13	32.80341000	-79.73932000	2.00	18.4	1.60	> 18.0
Qhs32†	S05007-C2	32.65764700	-79.94247600	2.74	18.6	1.52	17.8
Qhs33*	S02522-B4	32.62476000	-80.04264000	4.00	20.4	2.29	22.8
Qsbs1	UCHN006	32.81927872	-79.81001282	2.10	20.5	N/A	>20.0
Qsbs2†	UCHN009	32.84453964	-79.77661896	2.70	20.5	N/A	16.5
Qsbs3	UCHN010	32.81518173	-79.81542969	3.00	20.5	N/A	15.3
Qsbs4	UCHN012	32.83103180	-79.79888153	3.00	20.5	N/A	>20.0
Qsbs5	UCHN013	32.84091950	-79.78315735	0.00	20.5	N/A	>20.0
Qsbs7	UCHN018	32.88084030	-79.73638916	0.90	20.1	N/A	N/A
Qsbs8	UCHN019	32.86034012	-79.76547241	2.10	20.5	N/A	>20.0
Qsbs9	UCHN022	32.80487061	-79.83109283	2.10	20.5	N/A	N/A
Qsbs10	UCHN023	32.79217148	-79.84715271	0.90	20.5	N/A	N/A
Qsbs12	UCHN038	32.59539032	-80.12756348	3.00	20.2	N/A	>20.0
Qsbs14	UCHN041	32.60388184	-80.10495758	4.90	20.2	N/A	N/A

Elev. = Elevation; N/A = Not available; †Site not used in liquefaction potential index (*LPI*) calculations

\*Site also included in the database compiled by Mohanan et al. (2006)

Table A-1 continued

CU Site Code	Performing Organization Project Code	Latitude	Longitude	Ground Surface Elev. (m)	Max Test Depth (m)	Water Table Depth (m)	Depth to Top of Cooper Marl (m)
Qsbs15	UCHN046	32.61013031	-80.14227295	4.90	20.2	N/A	N/A
Qsbs16	UCHN051	32.59162140	-80.16245270	4.90	20.2	N/A	N/A
Qsbs17	UCHN059	32.75751114	-79.96552277	3.00	20.0	N/A	16.7
Qsbs18	UCHN060	32.69504166	-79.96524048	3.00	20.0	N/A	N/A
Qsbs19	UCHN068	32.70848084	-79.93872833	3.00	20.2	N/A	N/A
Qsbs20	UCHN069	32.73101044	-79.91329956	0.30	18.4	N/A	N/A
Qsbs21*	W02130-S8	32.60890000	-80.14850000	N/A	18.0	1.50	>18.0
Qsbs22*	W02288-S2	32.78912800	-79.94256300	N/A	16.8	2.20	15.5
Qsbs23	S09639B-C1	32.78726800	-79.93222800	4.27	30.5	1.22	27.4
Qsbs24*	S01772-S3	32.81000000	-79.90000000	N/A	25.2	1.68	12.6
Qsbs25*	S02578-B1	32.78392000	-79.94272000	N/A	20.3	1.68	21.9
Qsbs26*	S02891-B2	32.81594000	-79.81218000	N/A	20.0	0.91	12.5
Qsbs27†*	S03305-B1	32.60466000	-80.08237000	N/A	14.9	1.52	18.7
Qws1	UCHN007	32.82307053	-79.81339264	3.00	31.8	N/A	20.5
Qws2	UCHN008	32.82872009	-79.81665802	6.40	20.4	N/A	18.6
Qws3	UCHN011	32.83111954	-79.80510712	5.50	20.4	N/A	>20.0
Qws4	UCHN014	32.84823990	-79.78704834	6.10	20.4	N/A	>20.0
Qws5	UCHN016	32.91213989	-79.70894623	3.60	20.0	N/A	11.0
Qws6	UCHN017	32.91632080	-79.71869659	7.90	20.4	N/A	14.0
Qws7	UCHN020	32.83732987	-79.81501770	7.00	20.4	N/A	>20.0
Qws8	UCHN021	32.82070160	-79.82499695	6.70	20.4	N/A	>20.0
Qws9	UCHN029	32.86824036	-79.78398895	6.10	20.1	N/A	17.7
Qws10	UCHN030	32.88478851	-79.75536346	4.90	20.0	N/A	17.8
Qws11	UCHN036	32.84696960	-79.82340241	6.40	20.0	N/A	16.0
Qws13†	UCHN047	32.74443817	-80.05003357	7.00	20.0	N/A	17.3
Qws14	UCHN048	32.73060989	-80.06582642	11.90	20.0	N/A	15.0
Qws15	UCHN049	32.66851044	-80.17838287	13.10	20.0	N/A	>19.2
Qws17	UCHN066	32.73587036	-79.96631622	3.00	20.0	N/A	17.5
Qws18	UCHN067	32.76950073	-79.99196625	3.00	20.1	N/A	14.5
Qws19	UCHN074	32.71643066	-79.96788025	1.80	20.0	N/A	18.6
Qws20	UCHN075	32.72975159	-79.94774628	4.30	20.0	N/A	>20.0
Qws21†*	W00363-S1	32.77983000	-79.93360000	7.00	18.9	2.29	18.3
Qws22†*	W01211-S4	32.75075000	-80.03594000	4.00	11.9	1.83	N/A
Qws23*	W01211-S9	32.75017000	-80.03339000	4.00	12.9	2.40	12.2
Qws24*	W01219-S1	32.81240000	-79.82970000	3.00	14.0	1.30	12.9
Qws25*	W01235-S1	32.62560000	-80.15160000	4.00	19.4	1.55	>19.4
Qws26*	W01239-S3	32.84352000	-79.81500000	6.00	18.9	4.40	>18.9
Qws27*	S02457-B1	32.78305000	-79.93475000	5.00	25.2	1.50	22.5
Qws28*	W01317-S2	32.70602800	-79.95145000	1.00	10.9	2.20	10.5
Qws29*	W01339-S1	32.72341700	-80.06530600	5.00	12.8	1.67	11.0
Qws30*	S02457-B2	32.78305000	-79.93475000	5.00	21.5	1.50	>21.3
Qws31†*	W01350-S1	32.82526600	-80.03937400	3.00	15.9	2.99	7.3
Qws32*	W02087-S5	32.84796000	-80.01652000	4.50	8.9	1.07	6.3
Qws33*	W02096-S1	32.61914000	-80.14383000	4.00	19.9	1.80	19.2
Qws34*	W02100-S1	32.80445000	-79.95087000	5.00	19.1	2.50	17.0
Qws35*	S02784-SBA	32.87448000	-79.77618000	5.00	24.3	0.30	20.9

Table A-1 continued

CU Site Code	Performing Organization Project Code	Latitude	Longitude	Ground Surface Elev. (m)	Max Test Depth (m)	Water Table Depth (m)	Depth to Top of Cooper Marl (m)
Qws36*	W02179-S1	32.80070000	-79.84580000	3.00	14.8	1.70	14.8
Qws37*	W02182-S1	32.84520000	-79.81100000	5.00	16.9	1.30	16.2
Qws38†*	W02212-S1	32.74813000	-80.09864000	2.44	15.1	1.20	>15.2
Qws39*	W02236-S1	32.84620000	-79.85438000	6.00	15.9	2.70	15.5
Qws40*	S02902-C13	32.82040000	-79.82187000	3.00	22.8	0.91	12.7
Qws41*	W03044-S1	32.75591000	-79.99801000	5.00	11.6	1.00	10.4
Qws42*	W03045-S2	32.74772000	-79.96944200	4.50	18.0	1.80	14.2
Qws43*	W03065-S1	32.84977800	-79.96704600	5.00	12.0	1.80	10.2
Qws44*	W03088-S1	32.77299000	-79.96943300	3.96	14.0	0.61	12.7
Qws45†*	W03106-S1	32.77647900	-79.92628800	4.00	14.5	1.67	N/A
Qws46*	W03114-S2	32.78550000	-79.94553000	4.00	26.0	1.60	24.3
Qws47*	W03337-S1	32.77520000	-79.96490000	4.50	13.7	1.60	13.7
Qws48*	W03367-S1	32.77420000	-79.96320000	5.50	15.0	2.50	13.6
Qws49*	W03436-S1	32.82870000	-79.83438000	5.00	16.0	0.90	16.0
Qws50*	W03454A-S1	32.79179000	-79.85435000	5.00	16.9	1.60	14.3
Qws51*	W04028-S1	32.85289000	-79.80492000	6.00	23.9	3.05	22.3
Qws52*	W04111-S1	32.75776000	-79.97323000	5.00	13.7	1.80	13.1
Qws53*	W04130-S1	32.84351000	-80.05943000	7.00	9.0	1.70	7.0
Qws54*	W04131-S1	32.77481800	-79.96544200	5.00	13.7	1.60	12.5
Qws55*	W04137-S1	32.80943000	-80.03140000	6.00	12.9	0.64	11.6
Qws56*	W04206-S2	32.83131000	-80.06847000	5.00	10.1	2.00	8.8
Qws57*	W04225-S1	32.82215900	-79.84092700	6.00	17.8	2.60	16.2
Qws58*	S03462-S1	32.78582000	-79.93626000	5.00	30.4	0.90	28.3
Qws59†*	W04375-S1	32.77620000	-79.93070000	5.00	14.7	1.90	N/A
Qws60*	S99876-S4	32.80911000	-79.94987000	4.00	39.2	1.52	17.4
Qws61*	S00297-S1	32.73262000	-80.05914000	9.00	14.5	1.82	14.5
Qws62*	S01018-B1	32.81000000	-79.87000000	7.00	12.2	0.45	11.9
Qws63*	S01039-B4	32.76220000	-79.97303000	6.00	22.8	1.98	15.0
Qws64*	S01143-B1	32.79362000	-79.85638000	6.00	30.3	0.91	24.0
Qws65*	S01317-B2	32.80000000	-79.96000000	5.00	22.7	2.13	15.5
Qws66	S11218-S2	32.84977000	-80.01041600	5.79	9.2	1.98	7.6
Qws67	S11218-S4	32.85069900	-80.01128800	5.79	9.2	1.83	7.6
Qws68	S12254-C3	32.77774000	-79.98131700	2.13	21.3	2.44	11.7
Qws69	S12588-C5	32.73216800	-79.93343400	4.57	30.3	1.52	24.0
Qws70	S13046-C8	32.82897700	-79.82835800	4.00	24.3	1.98	19.8
Qws71	S05314-S1	32.84091300	-79.86912200	6.71	22.8	1.52	18.0
Qws72	S13367-S2	32.78324000	-80.03288000	4.00	24.3	1.83	10.4
Qws73†	S13569-C2	32.78734100	-79.93665100	6.71	15.9	1.52	24.0
Qws74	S051044-C4	32.81093700	-79.85898500	5.49	15.2	0.91	12.0
Qws75	S06393-C16	32.82078091	-79.85106277	5.43	30.3	1.37	21.8
Qws76†	S06729-B1	32.81965828	-79.95712630	2.13	9.7	0.91	16.2
Qws77	S06946-B4	32.81420000	-79.84474500	5.49	30.3	1.22	13.5
Qws78	S07106-C8	32.79040500	-79.87221200	7.01	18.7	2.90	17.2
Qws79	S07226-C6	32.87774800	-79.76905700	7.92	15.7	0.91	13.0
Qws80	S07436-C5	32.81961100	-79.84378800	5.00	39.3	1.83	29.2
Qws81	S08289-C7	32.79317700	-79.94001000	5.79	30.3	2.13	17.7

Table A-1 continued

CU Site Code	Performing Organization Project Code	Latitude	Longitude	Ground Surface Elev. (m)	Max Test Depth (m)	Water Table Depth (m)	Depth to Top of Cooper Marl (m)
Qws82	S09637A1-C1	32.79999300	-79.94121700	3.66	26.0	1.22	19.7
Qws83	S09637A2-C2	32.80008700	-79.94051900	2.74	24.7	1.37	18.8
Qws84	S09637F1-C1	32.79616600	-79.93480200	4.27	22.7	1.22	16.0
Qws85	S09637F2-C2	32.79580100	-79.93480400	3.66	23.6	1.83	17.5
Qws86	S09638-C1	32.79090400	-79.93638900	4.57	22.6	1.68	16.7
Qws87	S09640-C7	32.84424000	-79.96775900	4.70	32.6	1.52	13.7
Qws88	S10470-C1	32.72070600	-79.96714000	5.18	28.4	2.29	18.9
Qws89	S13288-S1	32.79544000	-79.94026200	4.27	22.8	1.52	20.4
Qws90*	W04030-S1	32.79243000	-79.93803000	2.44	19.9	2.70	17.4
Qws91*	W03085A-S1	32.85823000	-79.91244000	3.50	12.9	1.80	12.5
Qws92*	W02195-S1	32.79328000	-80.02094000	4.50	10.9	1.89	10.9
Qws93*	W02299-S1	32.58330000	-80.34550000	6.00	16.8	0.50	18.1
Qwls1*	W02115-S5	32.88220000	-79.99966000	9.00	8.80	2.10	7.4
Qwls2*	W02127-S1	32.87976600	-79.97890300	7.00	14.00	1.49	12.8
Qwls3*	W02202-S1	32.89233000	-80.07123000	12.00	10.90	2.49	10.2
Qwls4*	W02218-S1	32.87868000	-80.00332000	9.00	14.90	1.53	13.4
Qwls5*	W02301-S1	32.88450000	-79.98310000	10.00	14.90	1.80	13.0
Qwls6*	W04016A-S6	32.86449000	-79.97742000	7.30	25.80	2.00	24.6
Qwls7*	W04337-S3	32.87599800	-79.99461400	11.00	14.90	1.50	13.9
Qwls8*	W04432-S1	32.85536000	-79.97939000	8.00	8.80	1.21	7.6
Qwls9*	S03508-S1	32.86430000	-80.01540000	9.00	18.30	1.52	10.0
Qwls10	S10334-C1	32.73833200	-80.17511700	15.80	14.97	1.83	>15.0
Qwls11	S12090-C14	32.88036800	-79.97271600	8.10	15.27	3.66	10.8
Qwls12	S13018-C1	32.88784400	-79.99917000	7.00	9.05	1.68	7.6
Qwls13	S13395-S1	32.88376000	-79.97437600	9.40	22.92	1.22	10.6
Qwls14	S06858H-S1	32.73942297	-80.23579014	9.40	10.89	2.44	13.3
Qwls15	S06858H-S2	32.73942297	-80.23579014	9.40	16.72	2.59	13.5
Qwls16	S06858H-S3	32.73942297	-80.23579014	9.40	14.01	2.44	14.2
Qts1	UBKY001	32.97032929	-79.81346893	14.90	19.7	N/A	≥17.5
Qts2	UBKY002	32.97573853	-79.80623627	14.30	20.5	N/A	≥19.0
Qts3	UCHN032	32.90428162	-80.02674866	17.00	20.5	N/A	9.7
Qts4	UCHN033	32.91664124	-80.03225708	15.80	20.5	N/A	9.6
Qts5	UCHN034	32.91704941	-80.03913879	17.90	19.8	N/A	16.6
Qts6	UCHN035	32.89944840	-80.01303101	17.30	20.5	N/A	14.0?
Qts7	UBKY003	32.98043060	-79.79762268	13.10	20.2	N/A	≥18.0
Qts8	UBKY004	32.98413849	-79.78658295	15.20	20.5	N/A	>20.0
Qts9	UBKY005	32.98994064	-79.77984619	11.90	20.3	N/A	>20.0
Qts10	UBKY006	32.90459824	-79.92373657	12.20	20.0	N/A	11.3
Qts11	UBKY007	32.91498184	-79.90614319	14.60	20.2	N/A	>20.0
Qts12	UBKY008	32.92337036	-79.89881897	11.90	20.2	N/A	≥13.0
Qts13	UBKY009	32.94427872	-79.83850098	14.00	20.0	N/A	18.0?
Qts14	UBKY010	32.96195984	-79.85299683	11.30	20.2	N/A	18.0?
Qts15	UBKY011	32.95428085	-79.81712341	13.10	20.2	N/A	16.0?
Qts16	UBKY012	32.96821976	-79.82102203	15.80	20.0	N/A	≥17.3
Qts17	UBKY013	32.96525955	-79.83425903	13.10	20.4	N/A	≥17.5
Qts18	UBKY014	32.99502945	-79.77111816	11.90	20.2	N/A	>20.0

Table A-1 continued

CU Site Code	Performing Organization Project Code	Latitude	Longitude	Ground Surface Elev. (m)	Max Test Depth (m)	Water Table Depth (m)	Depth to Top of Cooper Marl (m)
Qts19	UBKY015	32.99991989	-79.76251221	9.10	20.2	N/A	>20.0?
Qts20	UBKY016	32.99280930	-79.75895691	11.30	20.0	N/A	>20.0
Qts21	UBKY017	33.00201035	-79.74855042	11.90	20.1	N/A	>20.0
Qts22	UBKY018	33.01222992	-79.74066162	12.20	20.2	N/A	≥17.0?
Qts23	UBKY019	32.90872955	-79.91506958	14.30	33.0	N/A	>29.5
Qts24	UBKY020	33.02156067	-79.73298645	14.00	20.0	N/A	>20.0
Qts25	UBKY021	33.03567123	-79.73618317	13.10	20.0	N/A	>20.0
Qts26	UBKY022	33.03266907	-79.72120667	14.90	18.0	N/A	>18.0
Qts27	UBKY023	32.91147995	-79.98547363	14.00	20.2	N/A	9.0
Qts28	UBKY024	32.91181946	-80.00705719	14.90	15.4	N/A	8.4
Qts29	UCHN064	32.89822006	-80.06037140	17.00	20.1	N/A	15.5?
Qts30	UCHN065	32.91178131	-80.06802368	14.00	20.0	N/A	15.0?
Qts31*	W01292-S1	32.90027000	-80.05950000	11.00	12.9	3.04	11.5
Qts32*	W02104-S1	32.90420000	-79.91700000	N/A	27.9	8.00	26.0
Qts33*	W04320-S1	32.91243000	-80.04323000	N/A	18.1	3.81	>18.0
Qts34*	W05043-S1	32.90375000	-80.02839000	N/A	9.6	1.52	7.2
Qts35	S05287-C2	32.91820800	-79.90426500	13.72	12.2	1.83	>12.0
Qts36	S09537-C1	32.89485900	-80.02672200	13.41	22.9	1.98	12.5
Qts37	S09543-C1	32.90831400	-80.02545400	10.97	30.5	3.50	8.8
Qts38	S11060-C5	32.93063900	-80.02966300	12.50	17.6	2.13	13.8
Qts39	B96-Ten01	32.89100000	-80.02550000	9.00	9.1	1.50	6.0
Qts40	B96-Ten02	32.89120000	-80.02530000	9.00	9.1	1.50	6.1
Qts41†	B96-Ten03	32.89140000	-80.02510000	9.00	12.1	1.50	6.2
Qts42	S03172-B4	32.90550000	-79.91080000	12.00	28.2	4.00	24.8
Qts43	B96-Ten10	32.91430000	-80.05440000	15.00	9.0	3.00	11.2
Qts44	B96-Ten09	32.91460000	-80.05450000	14.00	9.0	3.00	11.2
Qts45	B96-Ten08	32.91490000	-80.05470000	14.00	9.0	2.30	11.2
Qts46	B96-Ten07	32.91520000	-80.05480000	14.00	9.0	2.30	11.2
Qts47	B96-Ten06	32.91540000	-80.05490000	13.00	9.0	2.30	11.2
Qps1	S08433-C16	33.07644200	-80.19247100	22.60	10.6	2.44	10.3
Qps2	S13494-B2	33.03150100	-80.18316000	23.00	15.5	2.44	14.3
Qps3	T135047-S1	33.06420000	-80.14960000	26.00	15.9	2.53	15.9
Qps4	T135057-S1	33.01630000	-80.20580000	22.00	10.2	0.76	10.1
Qps5	T155009-S4	33.06306884	-80.09817464	24.00	14.7	0.46	12.4
Qps6	T155107-S4	33.06249000	-80.09853000	23.00	13.8	1.52	12.9
Qps7	T155130-S8	33.04965400	-80.15859600	24.50	18.9	1.46	15.0
Qps8	T165011-S1	33.05570000	-80.10092000	21.00	15.0	1.68	13.7
Qps9	T165036-S1	33.10732000	-80.12902000	27.00	14.5	0.00	14.4
Qps10	T165064-S10	33.05905000	-80.09820000	21.00	13.8	1.77	13.8
Qps11	T165070-S3	33.05667200	-80.10074300	21.00	17.0	1.74	15.2
Qps12	T165076-S1	33.07125200	-80.17190200	24.00	12.9	0.70	12.9
Qps13	T165100-S1	33.04377000	-80.14735900	23.00	19.0	0.91	14.2
Qps14	T165138-S3	33.10113035	-80.12769685	27.00	16.9	0.40	16.4
Qps15	T165147-S1	33.05960000	-80.18600800	23.00	16.0	1.52	13.3
Qps16	T165151-S3	33.03097300	-80.13917200	22.00	9.7	0.24	9.7
Qps17	T165245-S1	33.16594000	-80.10755800	25.00	8.8	0.91	8.8



Table A-2. Summary of SCPT and SCPTu data used in analysis of clayey deposits.

CU Site Code	Performing Organization Project Code	Latitude	Longitude	Ground Surface Elev. (m)	Max Test Depth (m)	Water Table Depth (m)	Depth to Top of Cooper Marl (m)
Qsbc1	UCH031	32.87408066	-79.75195313	2.44	20.1	N/A	7.8
Qsbc2†	S05622-C2	32.857725	-79.910852	2.31	12.2	1.52	7.6
Qsbc3†	S05863-D12	32.854031	-79.923393	1.55	15.2	1.68	11.9
Qsbc4	S07401-C9	32.91303311	-79.82533637	1.59	15.2	1.22	7.9
Qsbc5	S09639-C1	32.800566	-79.949227	2.75	22.5	1.52	15.3
Qsbc6	S13367-S24	32.743130	-80.022680	1.59	30.5	1.52	10.3
Qsbc7	S13367-S54	32.747580	-79.972440	1.41	24.8	1.37	14.1
Qsbc8*	W01277-S1	32.884056	-79.784470	2.70	8.0	1.52	10.0
Qsbc9*	W02120-S1	32.858384	-79.911230	2.16	11.0	1.30	8.5
Qsbc10*	W03058-S6	32.859950	-79.908170	3.23	13.0	1.70	11.7
Qsbc11*	W04378-S5	32.857040	-79.906140	2.08	11.0	1.82	9.5
Qsbc12*	W02219-S1	32.878790	-79.931450	1.86	10.0	1.30	7.0
Qsbc13*	W01165-S1	32.867420	-79.808780	1.56	18.0	1.52	17.3
Qsbc14*	W01187-S1	32.899490	-79.832900	1.77	13.0	1.22	12.2
Qsbc15*	W04431-S1	32.883730	-79.785390	2.70	11.8	1.79	10.2
Qsbc16	S06858-S1C	32.792101	-80.065559	1.78	27.6	0.76	6.0
Qsbc17	S06858-S3C	32.792259	-80.065337	1.85	10.7	1.07	6.5
Qsbc18	S06858-S6C	32.791892	-80.065632	1.73	11.8	0.91	6.6
Qwc1*	W02162-S1	32.964826	-80.161839	5.36	8.9	2.00	4.9
Qwc2*	W04154-S10	32.893010	-79.796030	3.48	15.0	1.60	13.8
Qwc3	S051119-C3	32.95113556	-80.16668899	2.65	6.1	0.76	2.2
Qwc4	S09317-B24	32.974439	-80.087413	2.58	15.3	0.76	4.3
Qwc5	S13495-B2	32.924638	-80.232034	5.82	10.6	3.66	6.1
Qwc6	T165122-S1	32.980980	-80.083330	2.67	10.5	1.22	6.6
Qwc7	T165123-S1	32.944709	-80.037134	3.43	16.0	1.25	6.6
Qwc8	T165208-S1	32.950456	-80.163727	4.40	10.0	1.83	3.7
Qwc9	T165270-S1	32.942718	-80.075474	2.74	12.0	1.60	4.5
Qtc1*	W01218-S1	32.935510	-80.043350	10.94	16.2	1.98	14.0
Qtc2*	W02059-B6	32.922900	-80.095200	8.76	13.0	3.50	>13.0
Qtc3*	S03489-B1	32.969620	-80.027310	10.02	30.3	2.44	13.4
Qtc4*	W04179-S1	32.928330	-80.129100	6.81	10.9	1.90	5.3
Qtc5†	S06562-B1	32.924698	-80.091242	9.55	15.2	1.83	9.1
Qtc6	S07238-C10	32.938125	-80.139507	5.28	15.2	2.90	4.2
Qtc7	S09317-B19	32.964919	-80.089954	7.29	18.1	1.52	4.3
Qtc8	T145105-S1	32.91250875	-80.09772260	8.40	13.0	0.91	7.0
Qtc9	T155080-S2	32.918303	-80.105504	8.95	7.0	1.52	>7.0
Qtc10	T155113-S11	32.929850	-80.051440	9.12	14.1	1.83	10.2
Qtc11	T155140-S1	32.938000	-80.041210	8.54	20.0	3.05	16.9
Qtc12	T155163-S1	32.915240	-80.111050	7.74	11.3	2.07	5.4
Qtc13	T165024-S2	32.982986	-80.066605	9.72	12.0	2.21	6.7
Qtc14	T165026-S1	32.983853	-80.069650	7.98	9.0	0.99	5.1
Qtc15	T165067-S1	32.975348	-80.135316	8.67	11.0	0.76	4.9
Qtc16	T165091-S1	32.940120	-80.077018	5.80	9.2	0.61	>9.1
Qtc17	T165265-S1	32.953875	-80.069176	7.05	13.0	2.44	5.2

Elev. = Elevation; N/A = Not available; †Site not used in liquefaction potential index (*LPI*) calculations

\*Site also included in the database compiled by Mohanan et al. (2006)

Table A-2 continued

CU Site Code	Performing Organization Project Code	Latitude	Longitude	Ground Surface Elev. (m)	Max Test Depth (m)	Water Table Depth (m)	Depth to Top of Cooper Marl (m)
Qtc18	T165267-S1	32.971878	-80.129562	7.64	13.0	0.91	4.0
Qtc19	S06858D-S1	32.947477	-80.170682	7.51	9.6	2.13	5.7
Qtc20	S06858D-S2	32.947559	-80.170577	7.85	10.5	1.83	4.4
Qtc21	S06858D-S3	32.947224	-80.170414	7.70	10.6	2.29	4.5
Qtc22	S06858D-S6	32.947140	-80.169930	6.88	20.0	2.44	3.9
Qtc23	S06858D-S7	32.947619	-80.170455	7.61	9.2	5.03	6.6
Qlc1*	W01163-S1	32.994100	-80.103750	14.09	10.0	2.30	10.0
Qlc2*	W02073-S6	32.960300	-80.059600	10.32	9.0	1.49	7.6
Qlc3*	W03137-S1	32.978400	-80.069000	14.16	9.2	1.50	9.2
Qlc4*	W03390-S2	32.977070	-80.065230	13.10	8.3	2.00	>8.2
Qlc5*	W03422-S1	32.971540	-80.065250	13.89	10.0	1.50	9.9
Qlc6	S07988-C9	32.974947	-80.246952	17.60	9.8	2.74	9.4
Qlc7	S13437-M8	32.963397	-80.117648	13.87	12.4	3.05	10.7
Qlc8	T135114-S6	33.113050	-80.199580	17.08	7.7	3.05	>7.7
Qlc9	T145003-S1	32.981160	-80.087810	12.24	10.4	1.68	6.6
Qlc10	T145089-S1	32.975275	-80.060794	13.49	8.5	1.22	8.2
Qlc11	T145133-S1	33.037196	-80.065660	8.55	10.4	1.68	5.5
Qlc12	T155043-S1	33.019804	-80.045698	13.35	11.0	0.84	8.2
Qlc13	T155103-S1	32.975370	-80.073486	12.10	11.5	1.68	10.6
Qlc14	T155143-S1	32.976810	-80.122510	11.86	14.1	1.52	8.4
Qlc15	T155149-S1	33.003910	-80.102120	11.17	12.0	1.31	10.8
Qlc16	T155155-S14	32.998970	-80.119380	14.45	14.4	0.91	14.3
Qlc17	T165020-S25	32.962360	-80.104690	13.48	13.0	2.13	11.1
Qlc18	T165025-S1	32.980446	-80.066868	9.75	7.7	1.07	6.9
Qlc19	T165040-S8	33.049560	-80.085950	14.84	10.9	0.85	8.2
Qlc20	T165132-S6	32.974617	-80.109344	13.82	13.0	1.13	11.5
Qlc21	T165156-S1	33.030689	-80.059481	12.77	13.0	2.74	6.1
Qlc22	T165157-S1	32.985669	-80.096404	11.88	11.0	0.67	8.1
Qlc23	T165163-S1	33.004913	-80.044960	14.61	10.0	1.83	6.8
Qlc24	T165169-S1	32.977557	-80.126887	13.83	12.7	1.37	9.1
Qlc25	T165203-S1	33.055333	-80.088407	15.33	7.6	3.17	>7.7
Qlc26	T165217-S1	32.977781	-80.125407	12.99	13.0	2.56	10.7
Qlc27	T165240-S10	32.973146	-80.250304	17.94	10.5	1.71	10.1
Qpc1*	W02250-S1	32.992500	-80.220800	16.05	12.8	3.10	12.2
Qpc2*	W04282-S2	33.006300	-80.235200	19.85	14.9	1.70	14.9
Qpc3*	W04282-S3	33.023210	-80.251410	11.05	7.9	1.60	5.6
Qpc4*	W05024-S2	33.033260	-80.241710	18.18	9.9	0.82	7.2
Qpc5*	S02823-C1	33.056140	-80.217010	18.05	8.8	2.44	>8.7
Qpc6	S06711-C13	33.057960	-80.095472	17.04	9.8	0.91	>9.8
Qpc7	S07966-C4	33.045945	-80.211618	20.01	13.7	1.52	10.1
Qpc8	T145083-S1	33.055255	-80.228339	18.12	9.0	4.57	>9.0
Qpc9	T145083-S2	33.055255	-80.228339	18.12	8.6	4.63	>8.6
Qpc10	T155089-S1	33.081320	-80.201160	19.16	11.0	6.31	>11.0
Qpc11	T165131-S1	33.028767	-80.175049	21.66	16.0	1.83	13.4
Qpc12	T165188-S1	33.030170	-80.204910	21.19	17.0	2.13	12.6
Qpc13	T165268-S1	33.061904	-80.233912	17.42	9.0	2.29	>9.0

## **APPENDIX B**

### **SUMMARY OF OBSERVATIONS ALONG RAILROAD LINES**

The tables presented in this appendix were compiled by Ronald D. Andrus from field notes by Earle Sloan and W. J. McGee published in Dutton (1889) and Peters and Hermann (1986). Eleanor L. Huggins and Kenneth T. Wicks assisted with the latitude and longitude determination of ground deformations along the railroads. This work was supported, in part, by the United States Geological Survey (USGS), Department of the Interior, under grant numbers 08HQGR0085, and the Clemson University Restoration Institute, as part of the Resilient Infrastructure Project.

Table B-1. Disturbances along the South Carolina Railroad from Charleston to Jedburg (Adapted from field notes by Earle Sloan and W. J. McGee as cited by Dutton [1889, pp. 283-288] and Peters and Hermann [1986, pp. 18-26, 54-55])

Site No.	Mile Point	Latitude (degrees)	Longitude (degrees)	Elev. (m)	Description of Disturbance	Surface Geology <sup>a</sup>
A1	0.0	32.789764	-79.937573	---	Charleston station near Marion Square—no marked disturbance of roadbed to mile point 3.57	Qws
A2	3.57	32.835994	-79.959171	4.42	Curve disturbed, several joints well opened; occasional craterlets to mile point 5.0	Qws, af/Qhes
A3	5.0	32.851180	-79.976307	8.23	Fish-plate bolts sheared; 180 mm opening at joints on both sides; sand discharged around well	Qwls
A4	5.85	32.856491	-79.989125	5.79	Joints strained open	Qwls
	6.0	32.858214	-79.990685	5.33	Roadbed depressed 150 mm under short chord	af/Qwls
	6.09	32.859506	-79.991907	5.23	Joints strained open; occasional slight depressions and transverse flexures to mile point 9.0	Qwls
	7.0	32.869792	-80.001806	---	Seven Mile Station—fissures less common	Qwls
A5	9.0	32.892832	-80.023111	4.11	Superstructure strained laterally	af/Qts
	9.23	32.895391	-80.025498	6.02	Kink in track; train derailed and wrecked to the east; craterlets increasing in size and number	Qts
A6	9.85	32.902655	-80.032294	6.86	Large borrow pit area on sand ridge honeycombed with craterlets	Qts
	10.0	32.904402	-80.033925	7.62	Superstructure jammed to the south; craterlets reach greatest development both in size and number	Qts
A7	10.85	32.914101	-80.043026	6.05	Track severely distorted to the southeast	af/Qts
	11.01	32.915894	-80.044700	5.81	Roadbed depressed 460 mm under 18 m chord	af/Qts
	11.02	32.915990	-80.044793	5.82	180 mm gap at joint; craterlets	Qts
	11.51	32.921622	-80.050006	6.28	180 mm gap at joint; flexures to east	Qts
	---	---	---	---	Occasional depressions mile points 11.6 to 15.0	Qts, Qtc, Qhm
A8	15.0	32.961463	-80.087141	---	Depressed and small transverse displacement	af/Qal
	15.3	32.963042	-80.088810	---	Woodstock—no reported damage to track	Qtc
A9	16.4	32.975708	-80.100185	---	Fissures and craterlets short distance from tracks; long (>200 m) fissure makes sharp turn before cut in slope for railroad	Qlc
A10	17.57	32.989000	-80.116509	12.01	Ladson station—“firmer ground”	Qlc

<sup>a</sup>Based on 1:24,000 geologic maps by Weems et al. (1997); Weems and Lemon (1988, 1993).

Table B-1 continued

Site No.	Mile Point	Latitude (degrees)	Longitude (degrees)	Elev. (m)	Description of Disturbance	Surface Geology <sup>a</sup>
A10	18.57	32.996747	-80.131027	12.50	Track severely flexures in reverse curve—320 mm east and 410 mm west of common cord; waterway at north end of damaged track	Qls
A11	19.66	33.005322	-80.146989	14.38	Culvert strained to the north and broken	af/Qpc
	19.76	33.006021	-80.148318	5.49	Severe flexure to the east	af/Qpf
	19.76	33.006097	-80.148455	5.49	Bending of wooden guard rail	af/Qpf
	19.95	33.007564	-80.151212	14.93	Sinuuous flexures	af/Qpc
	20.09	33.008737	-80.153331	15.21	Embankment over swamp; roadbed and superstructure forced to the right in series of irregular flexures, generally of no great amount	af/Qpc
	20.3	33.009953	-80.155869	---	Lincolnvile—"no fissures or craterlets"	Qpc, Qps
A12	21.23	33.017491	-80.169689	15.97	Trestle distorted laterally and vertically	Qpc
	21.47	33.019379	-80.173260	10.90	Track strained into slight reverse	af/Qpf
	21.61	33.020473	-80.175328	11.51	Summerville station—no disturbance to track; cratelets common in town and fields	Qps, Qpc
	21.85	33.022164	-80.178474	---	Culvert injured; track shifted to the right; disturbance diminished rapidly to Jedburg	af/Qpc
A13	27.38	33.065449	-80.258853	---	Jedburg—occasional craterlets; superstructure suffered stress to left at the south end of trestle	Qpc

Table B-2. Disturbances along the Northeastern Railroad from Charleston to Strawberry Station (Adapted from field notes by Earle Sloan as cited by Dutton [1889, pp. 288-294] and Peters and Hermann [1986, pp. 52-53])

Site No.	Mile Point	Latitude (degrees)	Longitude (degrees)	Elev. (m)	Description of Disturbance	Surface Geology <sup>a</sup>
B1	0.0	32.789286	-79.928561	---	Charleston station near Cooper River--cylindrical wall enclosing turntable strained to the southeast	af/Qhes
	---	---	---	---	Displacements inappreciable, mile points 0.1-1.47	af/Qhes/ Qws
B2	1.47	32.807222	-79.942031	---	Large area of ground moved laterally; flexure over 1000 m distance to the east with 460 mm ordinate	af/Qhes
B3	4.0	32.837744	-79.961350	---	Curve in road distorted	af
	6.0	32.855197	-79.987178	---	Road depressed 560 mm under 120 m chord	Qwls
B4	6.38	32.859903	-79.990394	---	Fish-plate bolts sheared; 360 mm opening of joints on both sides of track	Qwls
	7.0	32.867467	-79.995433	---	Slight depression within short space over culvert	af/Qws
B5	7.02	32.867750	-79.995464	7.62	Slight sinuous flexure	af/Qws
	7.85	32.878858	-80.007619	---	Slight sinuous flexure	Qwls
	8.85	32.892111	-80.007619	10.06	Embankment 4.9 m high depressed 250 mm on both sides of narrow waterway; telegraph poles east of road broken and inclined to the east	af/Qht/ Qws/Qts
B6	8.97	32.893700	-80.008483	---	Superstructure shifted 100 mm to the east	Qts
	9.0	32.894086	-80.008689	---	Long flexure with 100 mm ordinate to the east	Qts
	9.19	32.896686	-80.010039	13.72	Borrow pit excavation 1.8 m deep with many craterlets; water/sand ejected to heights of 4.0 m	Qts
	9.51	32.900867	-80.012331	---	Fish-plates broken; rails parted 220 mm	Qts
B7	9.57	32.901694	-80.012775	---	Sliding frog (switch) sheared and shifted 200 mm to the south; craterlets abundant	Qts
	9.76	32.904114	-80.014075	4.57	Superstructure deflected to the east	Qts
	10.07	32.908333	-80.016269	3.66	Embankment 4.6 m high forced 1.4 m to the east over distance of 56 m; rails bent 270 mm	af/Qwc/ Qts
B8	10.19	32.909842	-80.017131	1.22	Wing wall of culvert cracked; embankment 4.9 m high depressed; telegraph pole inclined to the east	af/Qhec/ Qwc/Qts

<sup>a</sup>Based on 1:24,000 geologic maps by Weems and Lemon (1984, 1988, 1993).

Table B-2 continued

Site No.	Mile Point	Latitude (degrees)	Longitude (degrees)	Elev. (m)	Description of Disturbance	Surface Geology <sup>a</sup>
B9	12.0	32.933806	-80.029967	7.92	Several fish-plates broken and joints parted; start of long flexure	Qtc
	12.09	32.934950	-80.030603	7.31	Flexure is 200 mm to the west; 51 mm crack extends across road and cut; within 46 m of track series of cracks developed with largest having widths of 530 mm and bearing N40E	Qtc
	12.13	32.935469	-80.030897	6.55	Superstructure shifted 2.5 m to the west and down grad jamming south end of trestle; bents of trestle inclined or fallen to the southeast; alignment restored by cutting out 550 mm section	af/Qtc
	12.44	32.939650	-80.033081	3.81	Culvert collapsed towards the north	af/Qal
	13.5	32.953728	-80.040583	---	Otranto—no reported road disturbance	Qtc
B10	15.51	32.982528	-80.039889	---	Goose Creek crossing—south end of trestle deflected to the east and north end to the west	Qal
	16.0	32.989658	-80.039014	12.80	Long sinuous curve in tracks through cut; ground thrown into ridges and rails bent in a vertical plane to conform to the fixed undulations.	Qlc
	---	---	---	---	No mark disturbance of road, mile points 16 to 18	Qlc
	18.0	33.018542	-80.035711	9.14	Mt. Holly station—no mark disturbance of road	Qtc
B11	18.51	33.025833	-80.034792	---	Descending grade; flexure along 370 m chord with 100 mm ordinate to the east	Qtc
B12	21.0	33.061831	-80.030511	6.10	“Last manifestation of great energy”; flexure along 270 m chord with 76 mm ordinate to the east	Qtc
B13	23.0	33.090974	-80.026886	---	Strawberry station—no marked road disturbance	Qtc

Table B-3. Performance of the Charleston and Savannah Railroad from Junction with the Northeastern Railroad to Adams Run (Adapted from Peters and Hermann 1986, pp. 51-52, 62-64; Dutton 1889, pp. 303-306)

Site No.	Mile Point	Latitude (degrees)	Longitude (degrees)	Elev. (m)	Description of Damage	Surface Geology <sup>a</sup>
C1	7.1	32.86308	-80.004900	---	Junction of the Charleston and Savannah Railroads; fissures less common	Qwls
	---	---	---	---	Occasional and slight transverse displacements between mile point 7.1 and the Ashley River	Qwls
C2	11.57	32.847440	-80.050288	-0.06	Ashley River Draw Bridge—jammed due to sliding of opposite banks towards middle of river; joints short distance west of river were opened by tension	af/Qht
	---	---	---	---	No marks of serious disturbance, mile points 11.6 to 16.38	Qws, af, Qwc, Qht
C3	16.38	32.792934	-80.107867	3.51	Initial point of long flexure to the south	af/Qhec
	17.7	32.786539	-80.130345	---	Rantowles Bridge—moved 940 (or 690) mm to the south; bents indicate banks moved towards middle of stream 330 mm from west and 130 mm from east; irregular cracks present on banks, but craterlets absent	af/Qht
	17.87	32.785299	-80.134784	---	End point of long flexure to the south	af/Qht
	17.95	32.784989	-80.136096	2.54	Rantowles Station—no appreciable disturbance	af/Qwc
C4	18.05	32.784491	-80.137971	6.32	Sharp kink in track in form of double flexure within distance of 12 m	af/Qht/ Qwc
	18.06	32.784444	-80.138002	6.32	Embankment across narrow swamp depressed 600 mm	af/Qht/ Qwc
C5	18.57	32.782067	-80.146675	4.34	Roadbed displaced vertically and laterally to south; displacement to the south increasing; craterlets reappeared	Qwls
	18.85	32.781064	-80.150548	3.43	Embankment 0.9 m high depressed 0.3 m; craterlets abundant and increasing in quantity as proceed to west; increasing lateral displacement	af/Qwls
	19.0	32.780270	-80.153196	3.05	Lateral displacement southward 630 mm	af/Qwls

<sup>a</sup>Based on 1:24,000 geologic maps by Weems and Lemon (1996); and personal communication with Peter Chirico.



Table B-3 continued

Site No.	Mile Point	Latitude (degrees)	Longitude (degrees)	Elev. (m)	Description of Damage	Surface Geology <sup>a</sup>
C6	19.57	32.777854	-80.162604	3.05	West end of trestle shifted northerly, east end shifted southerly; continued increasing lateral displacement	af/Qhec/ Qwc
	20.0	32.775620	-80.170495	3.05	Lateral displacement southward 1.27 m; lateral displacement maximum at mile point 20.3	af/Qhec
C7	20.95	32.771256	-80.186498	3.05	Sinuuous flexures were continuous though the final displacements were small to mile point 22.7, where they rapidly vanished	af/Qhec
C8	22.7	32.766956	-80.217870	---	End of continuous sinuuous flexures; higher and firmer ground	Qts
C9	25.0	32.762518	-80.259181	---	North of track 460 m, a 600-m-long fissure occurred with series of craterlets trending S80W	Qhm/Qts
	25.11	32.762317	-80.261237	---	Road depressed 150 mm	af/Qts
C10	25.85	32.760746	-80.274371	---	Road depressed 460 mm over 90 m length	Qts
	26.02	32.760491	-80.277544	---	Slight sinuuous flexures	Qts
C11	26.95	32.758675	-80.294186	---	Road undermined by craterlet (2.4 m x 1.8 m and 3 m deep); adjacent ditches blocked with expelled sand from craterlets	af/Qts
	27.23	32.758123	-80.299309	---	Slight strain southward	af/ Qhm/Qts
	27.28	32.758095	-80.300259	---	Slight depression of 100 mm	Qts
	---	---	---	---	Beyond mile point 27.57 disturbances were rare	Qts, Qtc
C12	29.85	32.755248	-80.346519	---	Adams Run Station—limiting line of craterlets	Qtc

## **APPENDIX C**

### **LIQUEFACTION PROBABILITY CURVES FOR MODEL OF CLAYEY DEPOSITS**

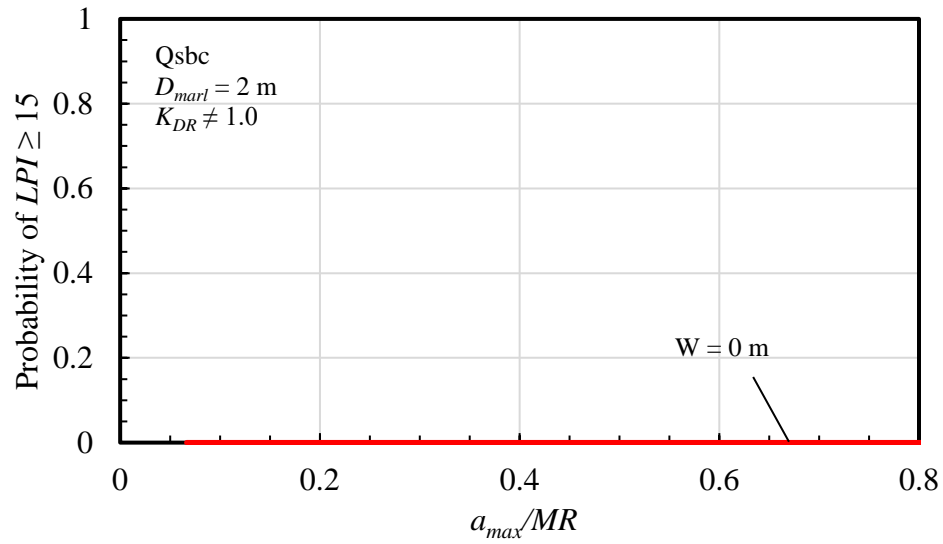


Figure C-1. Liquefaction probability curves for Qsbc assuming a depth to top of Cooper Marl of 2 m, and depth to groundwater (W) of 0 m.

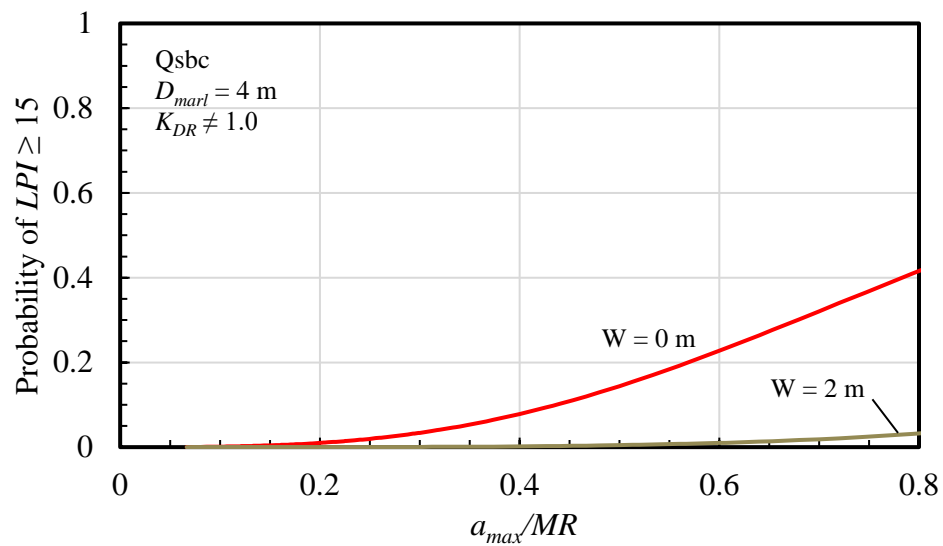


Figure C-2. Liquefaction probability curves for Qsbc assuming a depth to top of Cooper Marl of 4 m, and depths to groundwater (W) of 0 and 2 m.

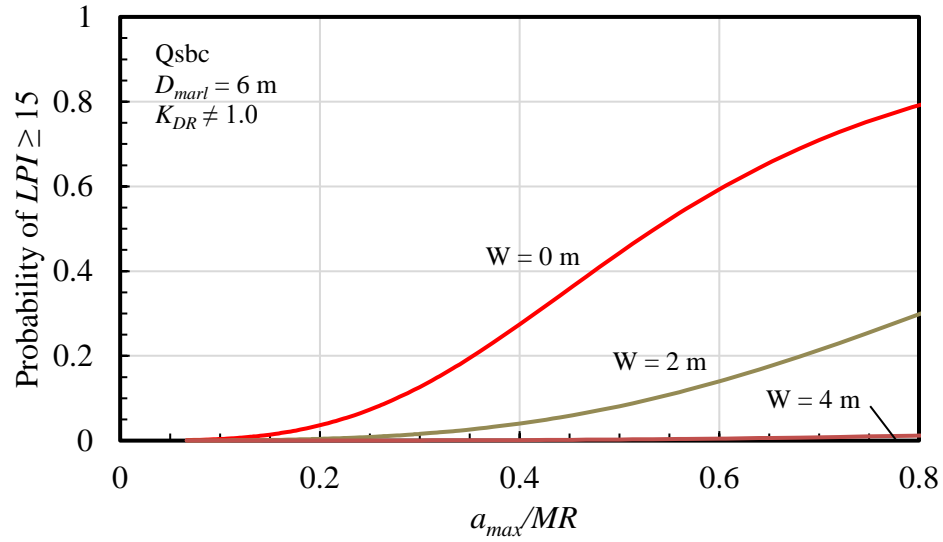


Figure C-3. Liquefaction probability curves for  $Q_{sbc}$  assuming a depth to top of Cooper Marl of 6 m, and depth to groundwater ( $W$ ) of 0, 2, and 4 m.

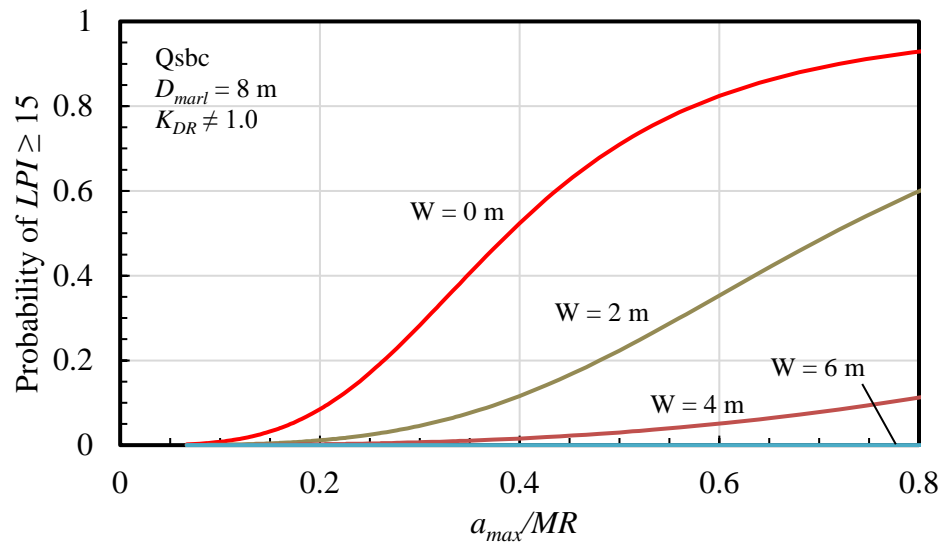


Figure C-4. Liquefaction probability curves for  $Q_{sbc}$  assuming a depth to top of Cooper Marl of 8 m, and depths to groundwater ( $W$ ) of 0, 2, 4, and 6 m.

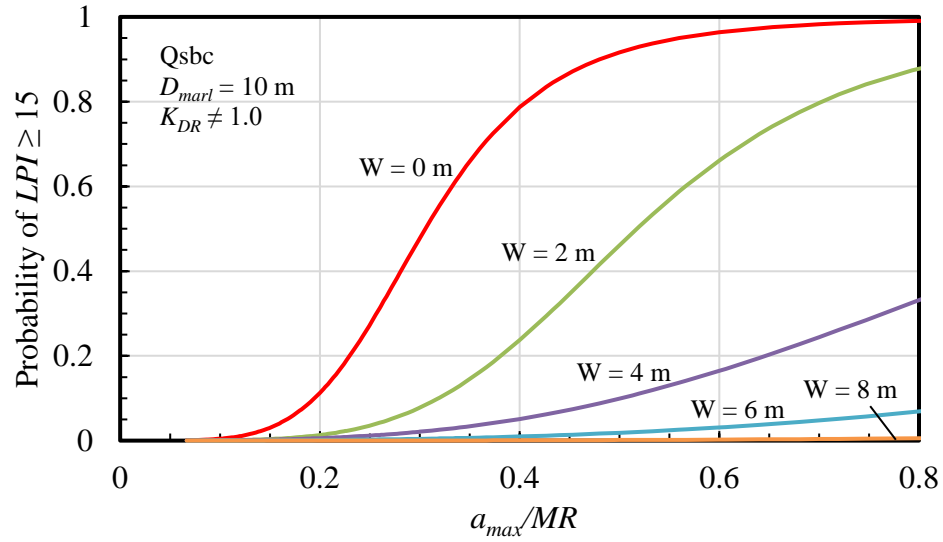


Figure C-5. Liquefaction probability curves for  $Q_{sbc}$  assuming a depth to top of Cooper Marl of 10 m, and depths to groundwater ( $W$ ) of 0, 2, 4, 6, and 8 m.

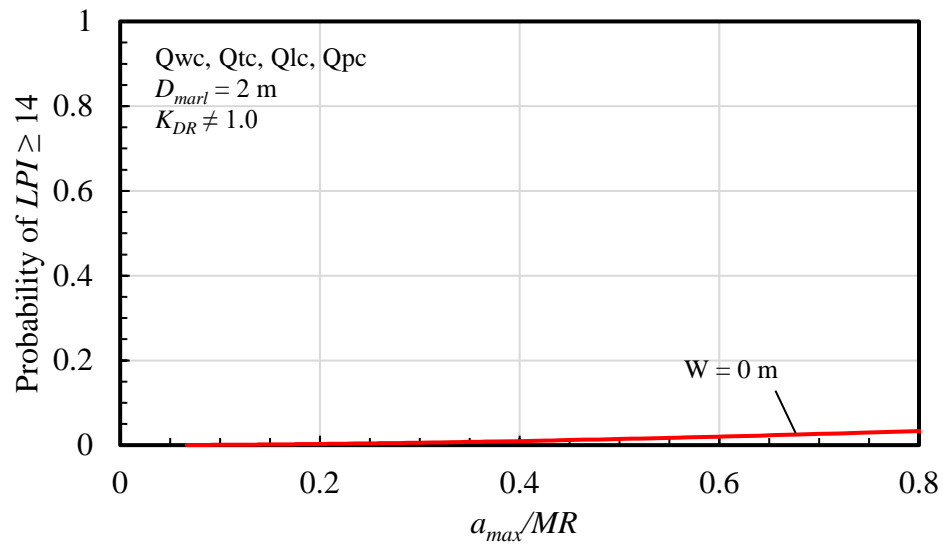


Figure C-6. Liquefaction probability curves for  $Q_{wc}$ ,  $Q_{tc}$ ,  $Q_{lc}$ , and  $Q_{pc}$  assuming a depth to top of Cooper Marl of 2 m, and depth to groundwater ( $W$ ) of 0 m.

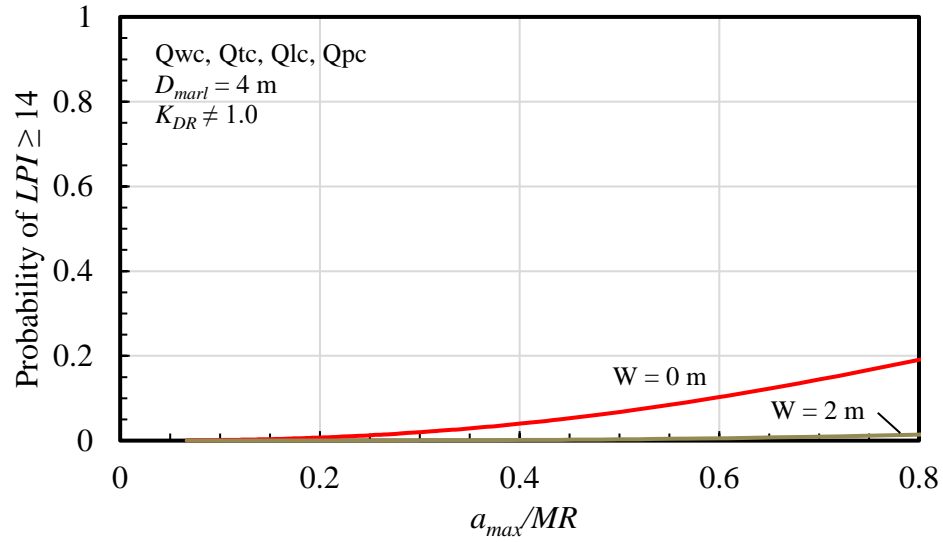


Figure C-7. Liquefaction probability curves for  $Q_{wc}$ ,  $Q_{tc}$ ,  $Q_{lc}$ , and  $Q_{pc}$  assuming a depth to top of Cooper Marl of 4 m, and depths to groundwater ( $W$ ) of 0 and 2 m.

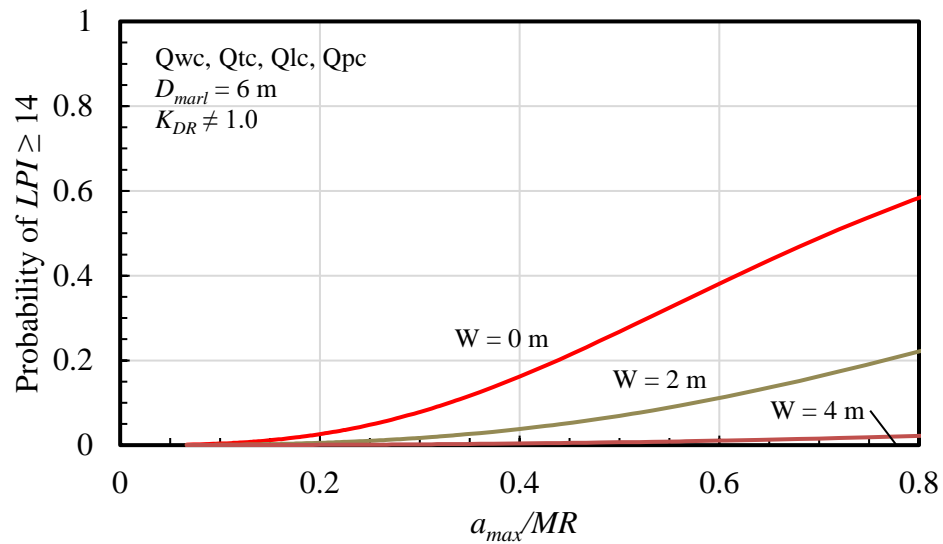


Figure C-8. Liquefaction probability curves for  $Q_{wc}$ ,  $Q_{tc}$ ,  $Q_{lc}$ , and  $Q_{pc}$  assuming a depth to top of Cooper Marl of 6 m, and depths to groundwater ( $W$ ) of 0, 2, and 4 m.

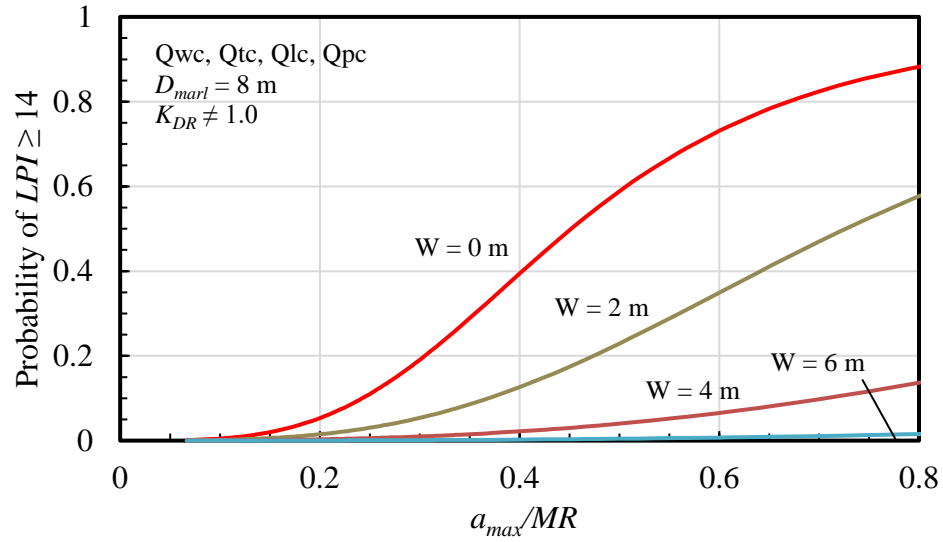


Figure C-9. Liquefaction probability curves for  $Q_{wc}$ ,  $Q_{tc}$ ,  $Q_{lc}$ , and  $Q_{pc}$  assuming a depth to top of Cooper Marl of 8 m, and depths to groundwater ( $W$ ) of 0, 2, 4, and 6 m.

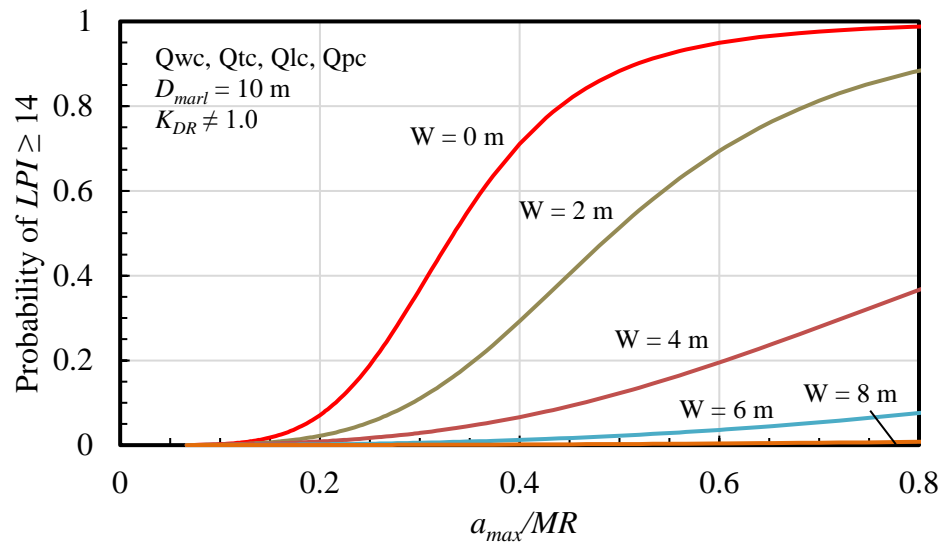


Figure C-10. Liquefaction probability curves for  $Q_{wc}$ ,  $Q_{tc}$ ,  $Q_{lc}$ , and  $Q_{pc}$  assuming a depth to top of Cooper Marl of 10 m, and depths to groundwater ( $W$ ) of 0, 2, 4, 6, and 8 m.

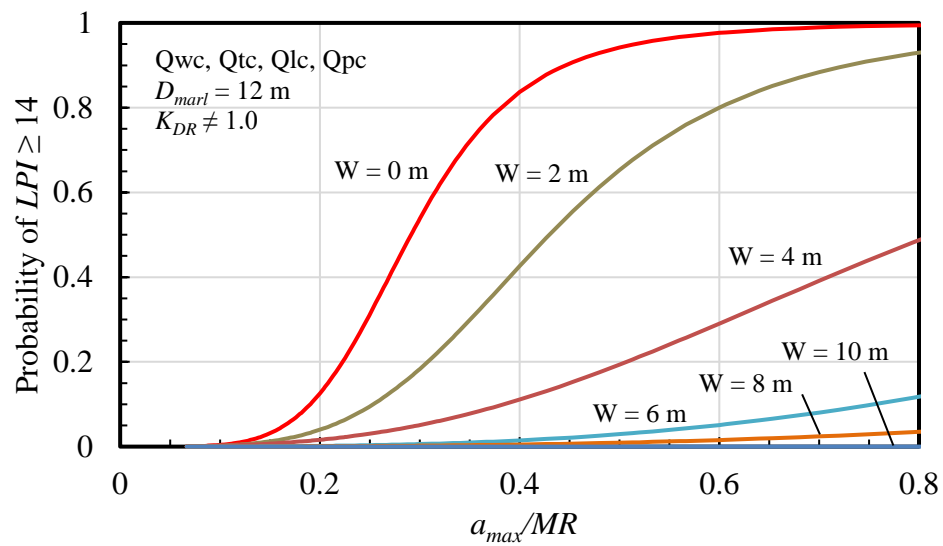


Figure C-11. Liquefaction probability curves for Qwc, Qtc, Qlc, and Qpc assuming a depth to top of Cooper Marl of 12 m, and depths to groundwater (W) of 0, 2, 4, 6, 8, and 10 m.



## **APPENDIX D**

### **SUMMARY OF SHEAR WAVE VELOCITY DATA FOR SAND AND CLAYEY UNITS**

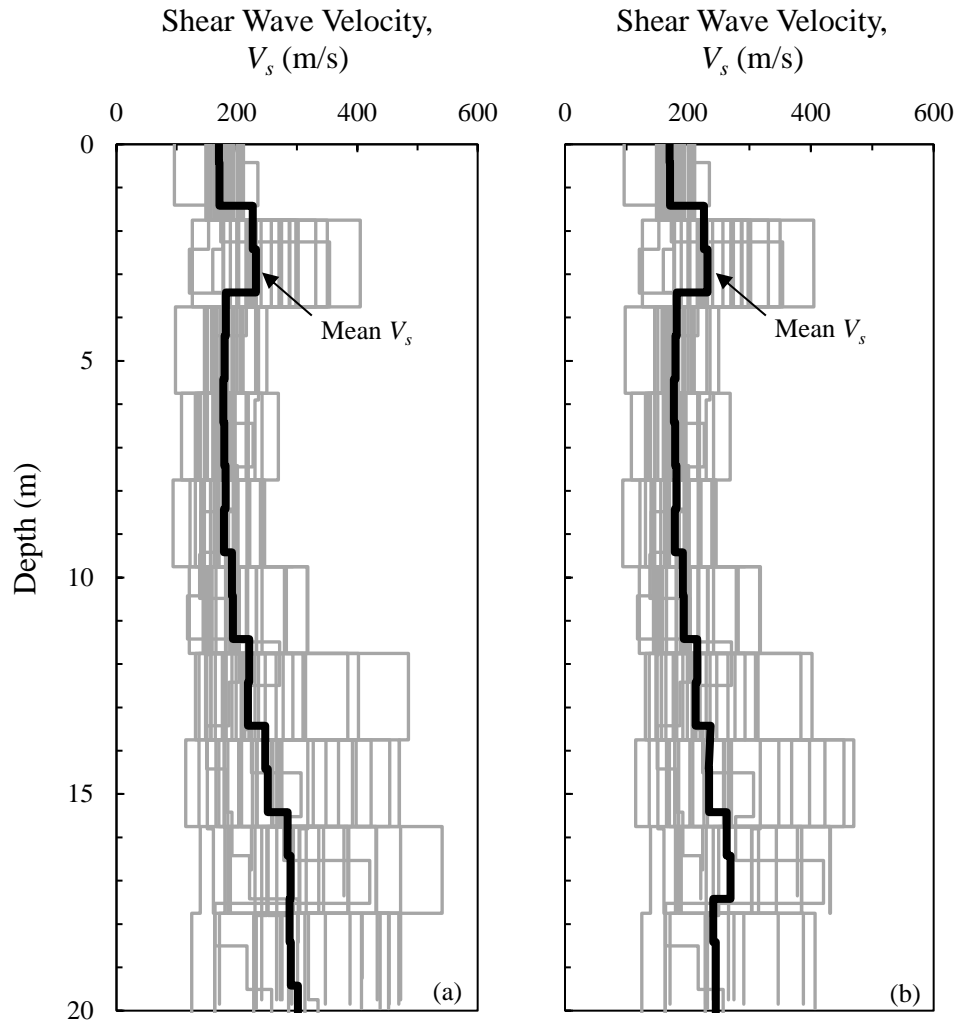


Figure D-1. Composite shear-wave velocity ( $V_s$ ) profiles for all Qhs sites, (a) including entire SCPT profiles, and (b) excluding portions of SCPT profiles in Marl.

Table D-1. Summary of shear wave velocity ( $V_s$ ) measurements above the Cooper Marl for Qhs sites.

Depth Range (m)	No. of $V_s$ Values	Geometric Mean $V_s$ (m/s)	Standard Deviation of $\ln(V_s)$ (m/s)
0 - 0.42	31	173	0.102
0.42 - 1.42	31	174	0.111
1.42 - 2.42	31	229	0.248
2.42 - 3.42	31	237	0.241
3.42 - 4.42	31	181	0.147
4.42 - 5.42	31	180	0.153
5.42 - 6.42	31	177	0.185
6.42 - 7.42	31	178	0.186
7.42 - 8.42	31	181	0.206
8.42 - 9.42	31	180	0.206
9.42 - 10.42	31	194	0.263
10.42 - 11.42	31	193	0.270
11.42 - 12.42	30	213	0.316
12.42 - 13.42	30	213	0.318
13.42 - 14.42	27	235	0.399
14.42 - 15.42	25	232	0.422
15.42 - 16.42	21	262	0.283
16.42 - 17.42	21	264	0.282
17.42 - 18.42	14	246	0.266
18.42 - 20.25	14	246	0.266

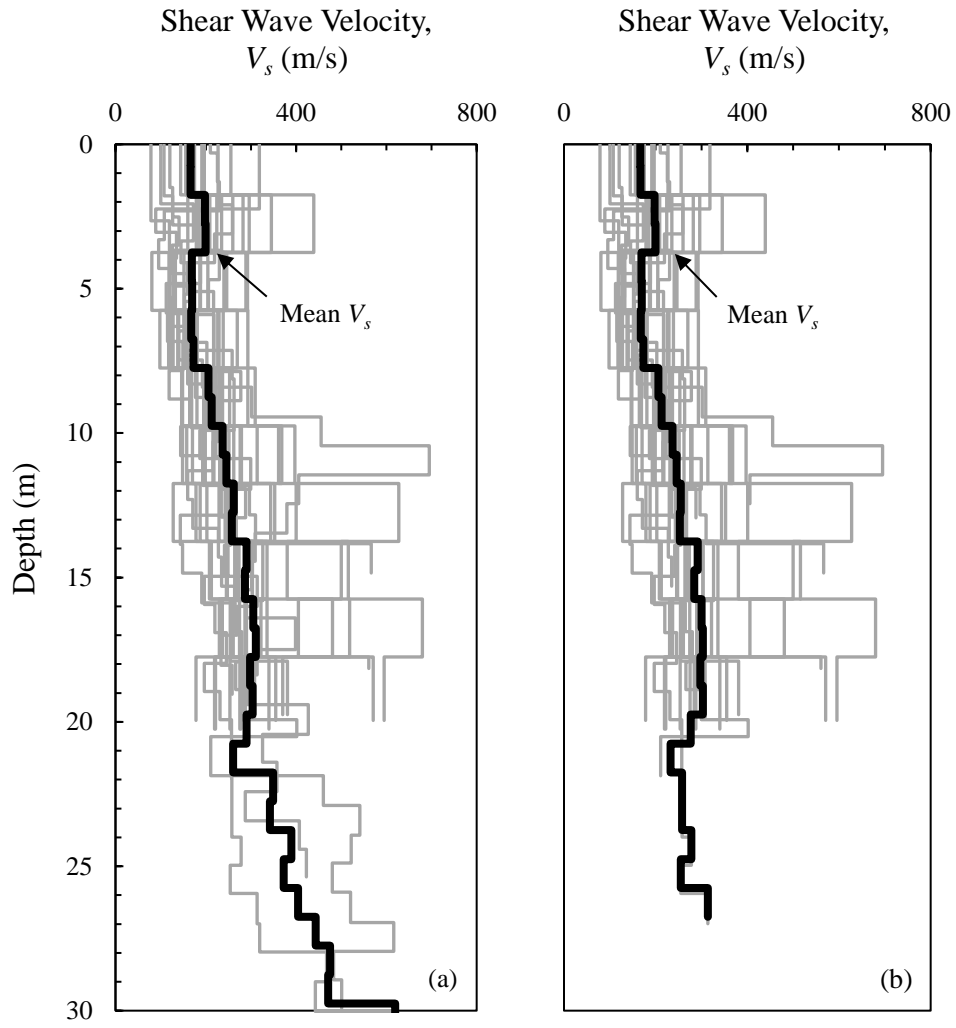


Figure D-2. Composite shear-wave velocity ( $V_s$ ) profiles for all Qsbs sites, (a) including entire SCPT profiles, and (b) excluding portions of SCPT profiles in Marl.

Table D-2. Summary of shear wave velocity ( $V_s$ ) measurements above the Cooper Marl for Qsbs sites.

Depth Range (m)	No. of $V_s$ Values	Geometric Mean $V_s$ (m/s)	Standard Deviation of $\ln(V_s)$ (m/s)
0 - 0.75	24	166	0.082
0.75 - 1.75	24	167	0.082
1.75 - 2.75	24	198	0.127
2.75 - 3.75	24	200	0.117
3.75 - 4.75	24	169	0.095
4.75 - 5.75	24	170	0.093
5.75 - 6.75	24	168	0.081
6.75 - 7.75	24	173	0.082
7.75 - 8.75	23	206	0.050
8.75 - 9.75	23	213	0.043
9.75 - 10.75	23	237	0.104
10.75 - 11.75	23	246	0.179
11.75 - 12.75	20	255	0.142
12.75 - 13.75	20	253	0.148
13.75 - 14.75	20	292	0.116
14.75 - 15.75	17	284	0.097
15.75 - 16.75	16	300	0.134
16.75 - 17.75	16	303	0.128
17.75 - 18.75	15	297	0.141
18.75 - 19.75	15	303	0.131
19.75 - 20.75	7	277	0.054
20.75 - 21.75	2	233	0.019
21.75 - 22.75	1	257	--
22.75 - 23.75	1	257	--
23.75 - 24.75	1	278	--
24.75 - 25.75	1	254	--
25.75 - 26.75	1	314	--

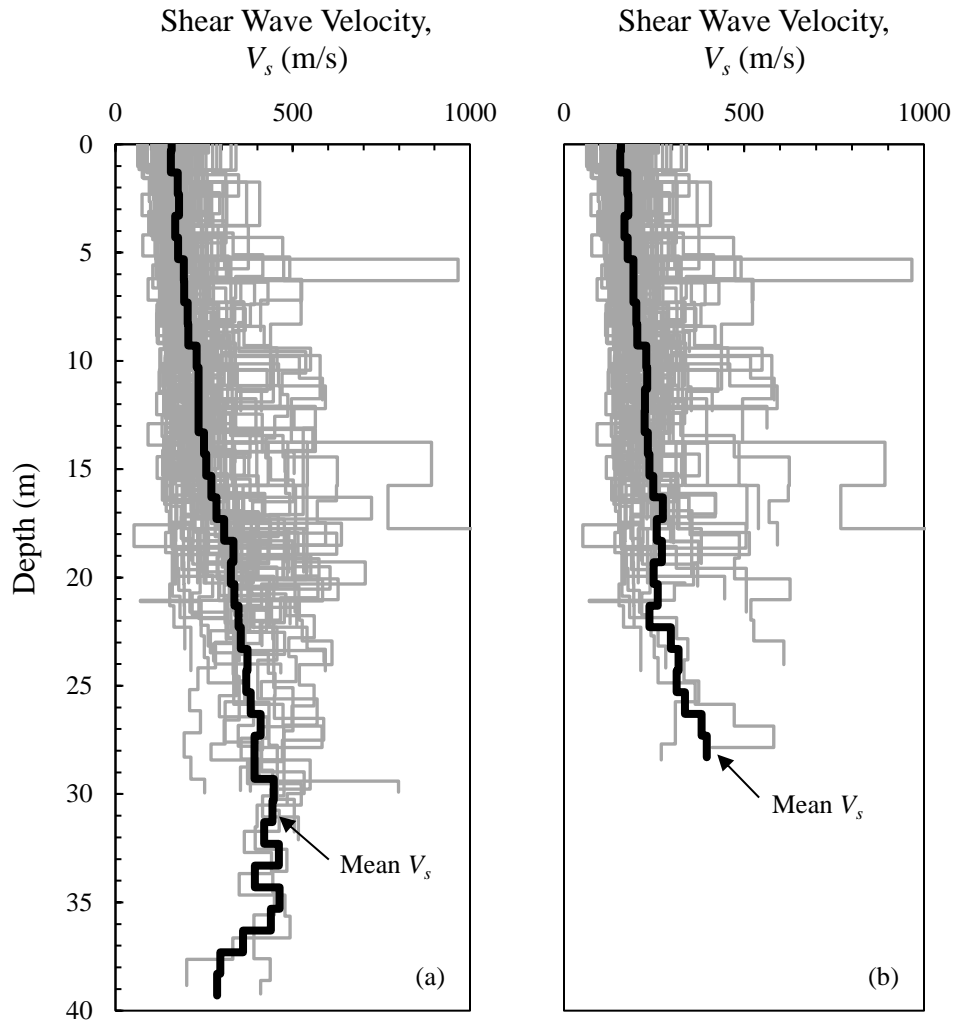


Figure D-3. Composite shear-wave velocity ( $V_s$ ) profiles for all Qws sites, (a) including entire SCPT profiles, and (b) excluding portions of SCPT profiles in Marl.

Table D-3. Summary of shear wave velocity ( $V_s$ ) measurements above the Cooper Marl for Qws sites.

Depth Range (m)	No. of $V_s$ Values	Geometric Mean $V_s$ (m/s)	Standard Deviation of $\ln(V_s)$ (m/s)
0 - 0.3	91	159	0.122
0.3 - 1.3	91	156	0.112
1.3 - 2.3	91	176	0.109
2.3 - 3.3	91	179	0.093
3.3 - 4.3	91	168	0.073
4.3 - 5.3	91	177	0.099
5.3 - 6.3	91	193	0.230
6.3 - 7.3	90	193	0.134
7.3 - 8.3	85	201	0.113
8.3 - 9.3	84	203	0.074
9.3 - 10.3	84	229	0.133
10.3 - 11.3	79	231	0.120
11.3 - 12.3	73	225	0.112
12.3 - 13.3	65	224	0.097
13.3 - 14.3	56	233	0.215
14.3 - 15.3	50	237	0.225
15.3 - 16.3	43	248	0.205
16.3 - 17.3	37	275	0.175
17.3 - 18.3	26	258	0.344
18.3 - 19.3	20	272	0.354
19.3 - 20.3	15	249	0.167
20.3 - 21.3	8	260	0.302
21.3 - 22.3	6	237	0.233
22.3 - 23.3	5	297	0.148
23.3 - 24.3	5	318	0.192
24.3 - 25.3	2	313	0.061
25.3 - 26.3	2	336	0.013
26.3 - 27.3	2	382	0.084
27.3 - 28.3	2	397	0.238

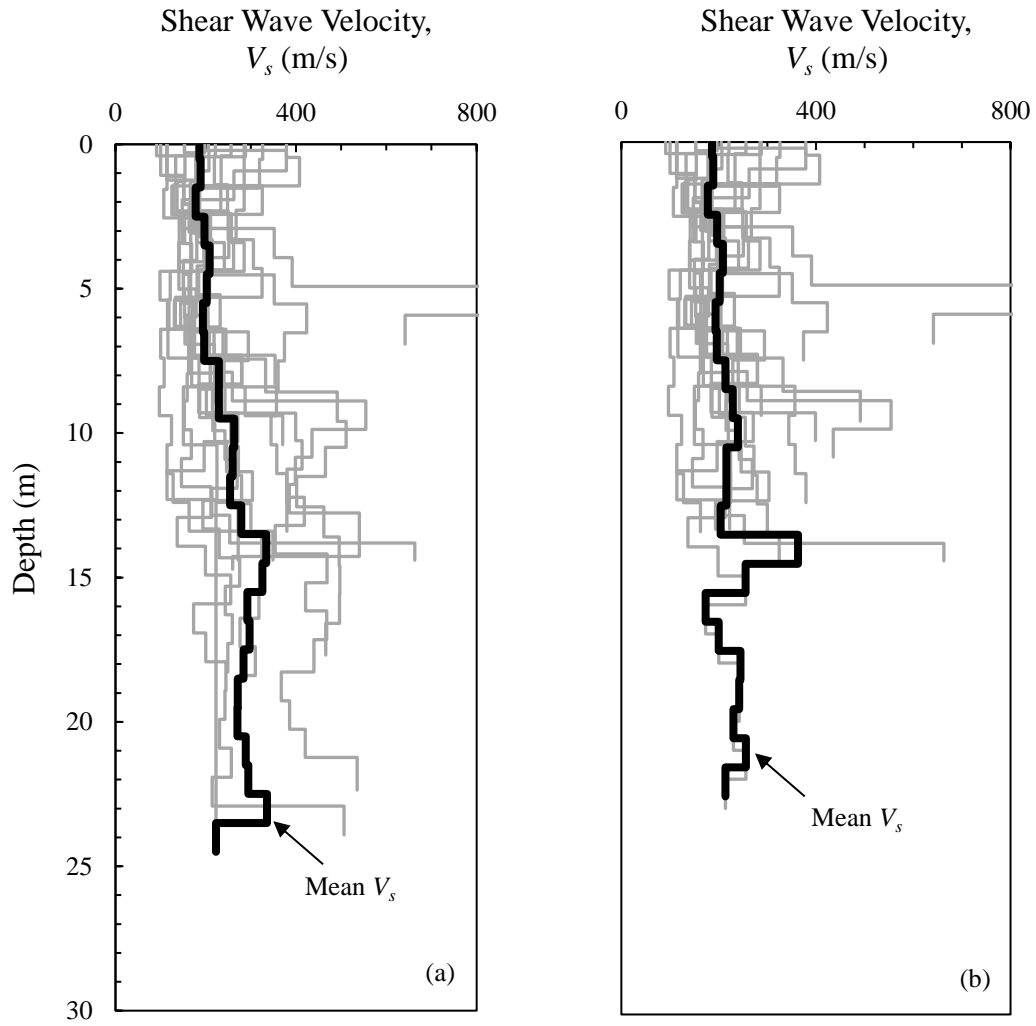


Figure D-4. Composite shear-wave velocity ( $V_s$ ) profiles for all Qwls sites, (a) including entire SCPT profiles, and (b) excluding portions of SCPT profiles in Marl.



Table D-4. Summary of shear wave velocity ( $V_s$ ) measurements above the Cooper Marl for Qwls sites.

Depth Range (m)	No. of $V_s$ Values	Geometric Mean $V_s$ (m/s)	Standard Deviation of $\ln(V_s)$ (m/s)
0 - 0.5	16	186	0.176
0.5 - 1.5	16	189	0.170
1.5 - 2.5	16	178	0.100
2.5 - 3.5	16	197	0.043
3.5 - 4.5	16	208	0.082
4.5 - 5.5	16	202	0.775
5.5 - 6.5	16	194	0.910
6.5 - 7.5	15	196	0.103
7.5 - 8.5	13	214	0.069
8.5 - 9.5	13	229	0.245
9.5 - 10.5	11	240	0.141
10.5 - 11.5	8	216	0.108
11.5 - 12.5	8	216	0.136
12.5 - 13.5	6	204	0.077
13.5 - 14.5	2	363	0.457
14.5 - 15.5	1	255	--
15.5 - 16.5	1	173	--
16.5 - 17.5	1	200	--
17.5 - 18.5	1	245	--
18.5 - 19.5	1	242	--
19.5 - 20.5	1	230	--
20.5 - 21.5	1	256	--
21.5 - 22.5	1	214	--

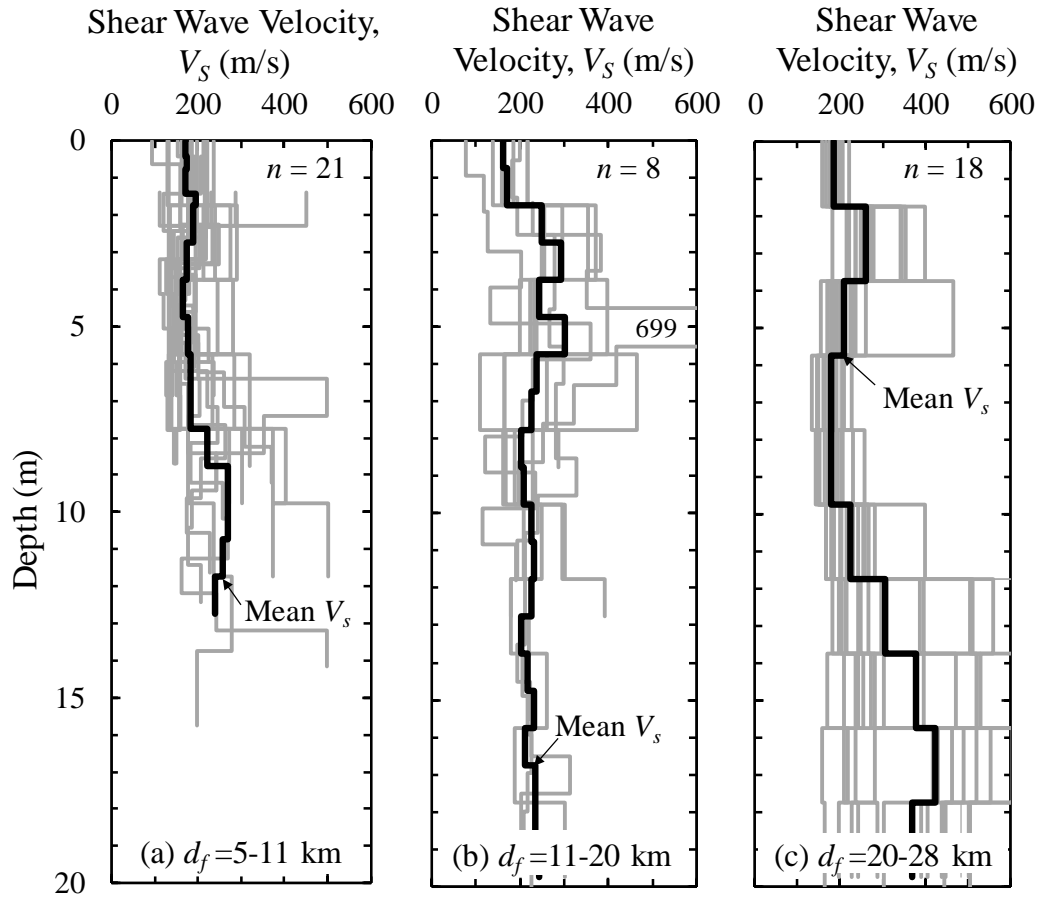


Figure D-5. Composite shear-wave velocity ( $V_s$ ) profiles above the Cooper Marl for Qts sites grouped by distance from Woodstock fault ( $d_f$ ).

Table D-5. Summary of shear wave velocity ( $V_s$ ) measurements above the Cooper Marl for Qts sites grouped by distance from Woodstock fault ( $d_f$ ).

Depth Range (m)	No. of $V_s$ Values	Geometric Mean $V_s$ (m/s)	Standard Deviation of $\ln(V_s)$ (m/s)	Depth Range (m)	No. of $V_s$ Values	Geometric Mean $V_s$ (m/s)	Standard Deviation of $\ln(V_s)$ (m/s)
Distance to Fault, $d_f = 5 - 11$ km				Distance to Fault = $d_f = 20 - 28$ km			
0-0.42	12	171	0.235	0-0.75	18	186	0.080
0.42-0.75	12	175	0.229	1.75-3.75	18	261	0.206
0.75-1.42	12	172	0.234	3.75-5.75	18	209	0.299
1.42-1.75	20	194	0.336	5.75-7.75	18	180	0.133
1.75-2.75	20	187	0.245	7.75-9.75	18	179	0.133
2.75-3.75	21	172	0.251	9.75-11.75	18	225	0.237
3.75-4.75	21	164	0.226	11.75-13.75	18	306	0.456
4.75-5.75	21	177	0.406	13.75-15.75	17	379	0.420
5.75-6.75	18	183	0.349	15.75-17.75	17	424	0.378
6.75-7.75	17	184	0.323	17.75-19.75	16	369	0.368
7.75-8.75	15	221	0.374				
8.75-9.75	8	269	0.257				
9.75-10.75	6	269	0.384				
10.75-11.75	6	257	0.413				
11.75-12.75	3	240	0.120				
Distance to Fault = $d_f = 11 - 20$ km							
0-0.75	7	162	0.270				
0.75-1.75	7	170	0.199				
1.75-2.75	8	248	0.285				
2.75-3.75	8	292	0.204				
3.75-4.75	8	245	0.302				
4.75-5.75	8	300	0.449				
5.75-6.75	8	238	0.425				
6.75-7.75	8	225	0.409				
7.75-8.75	8	203	0.262				
8.75-9.75	7	209	0.242				
9.75-10.75	7	224	0.247				
10.75-11.75	7	232	0.186				
11.75-12.75	5	227	0.326				
12.75-13.75	3	203	0.088				
13.75-14.75	3	218	0.129				
14.75-15.75	3	232	0.083				
15.75-16.75	3	212	0.083				
16.75-17.75	3	233	0.220				
17.75-18.75	3	233	0.191				
18.75-19.75	3	242	0.164				

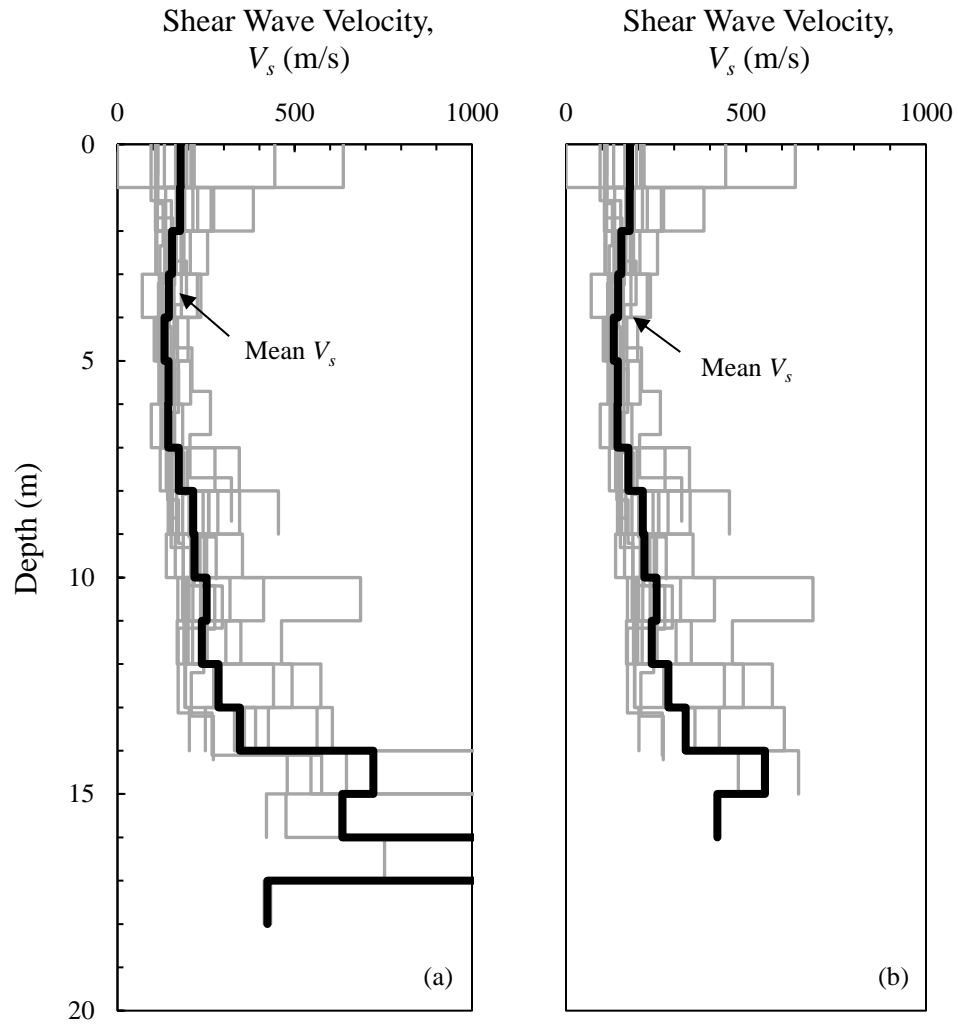


Figure D-6. Composite shear-wave velocity ( $V_s$ ) profiles for all Qps sites, (a) including entire SCPT profiles, and (b) excluding portions of SCPT profiles in Marl.

Table D-6. Summary of shear wave velocity ( $V_s$ ) measurements above the Cooper Marl for Qps sites.

Depth Range (m)	No. of $V_s$ Values	Geometric Mean $V_s$ (m/s)	Standard Deviation of $\ln(V_s)$ (m/s)
0 - 1.0	17	178	0.447
1.0 - 2.0	17	177	0.132
2.0 - 3.0	17	154	0.053
3.0 - 4.0	17	145	0.071
4.0 - 5.0	17	133	0.035
5.0 - 6.0	17	144	0.041
6.0 - 7.0	17	143	0.056
7.0 - 8.0	17	173	0.090
8.0 - 9.0	16	214	0.141
9.0 - 10.0	14	218	0.053
10.0 - 11.0	13	252	0.237
11.0 - 12.0	13	238	0.105
12.0 - 13.0	10	284	0.190
13.0 - 14.0	7	332	0.135
14.0 - 15.0	3	553	0.023
15.0 - 16.0	1	420	--

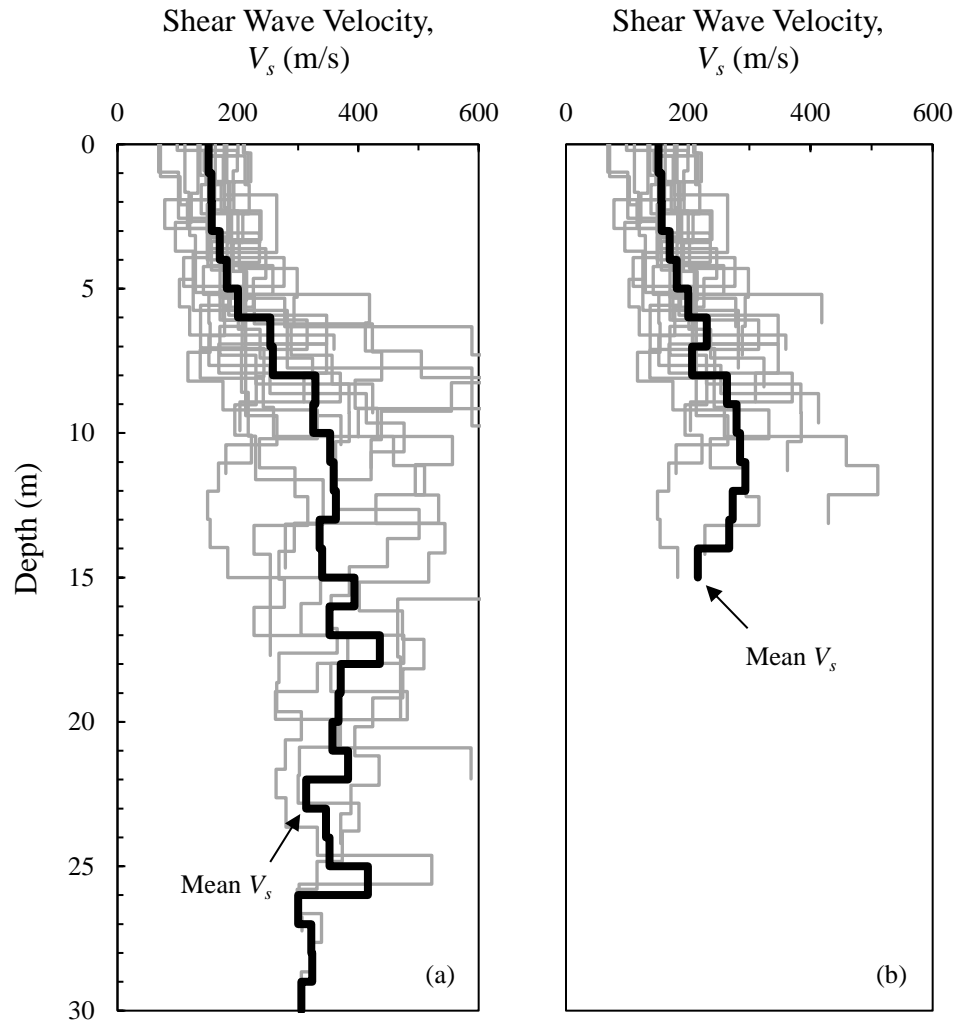


Figure D-7. Composite shear-wave velocity ( $V_s$ ) profiles for all Qsbc sites, (a) including entire SCPT profiles, and (b) excluding portions of SCPT profiles in Marl.

Table D-7. Summary of shear wave velocity ( $V_s$ ) measurements above the Cooper Marl for Qsbc sites.

Depth Range (m)	No. of $V_s$ Values	Geometric Mean $V_s$ (m/s)	Standard Deviation of $\ln(V_s)$ (m/s)
0 - 1.0	16	151	0.080
1.0 - 2.0	16	156	0.044
2.0 - 3.0	16	157	0.097
3.0 - 4.0	16	170	0.053
4.0 - 5.0	16	181	0.086
5.0 - 6.0	16	200	0.115
6.0 - 7.0	14	230	0.101
7.0 - 8.0	11	206	0.102
8.0 - 9.0	8	264	0.073
9.0 - 10.0	7	279	0.086
10.0 - 11.0	5	285	0.122
11.0 - 12.0	3	294	0.250
12.0 - 13.0	3	273	0.201
13.0 - 14.0	3	267	0.373
14.0 - 15.0	2	216	0.051

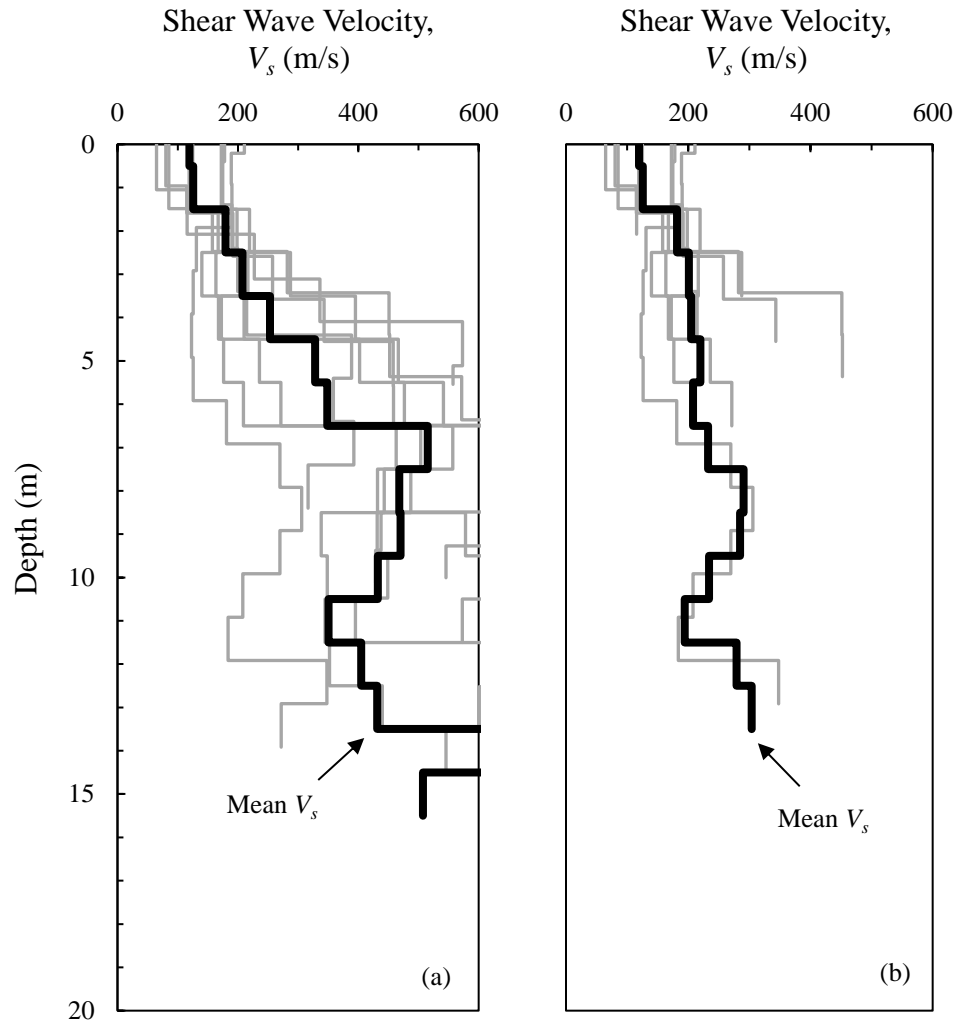


Figure D-8. Composite shear-wave velocity ( $V_s$ ) profiles for all Qwc sites, (a) including entire SCPT profiles, and (b) excluding portions of SCPT profiles in Marl.



Table D-8. Summary of shear wave velocity ( $V_s$ ) measurements above the Cooper Marl for Qwc sites.

Depth Range (m)	No. of $V_s$ Values	Geometric Mean $V_s$ (m/s)	Standard Deviation of $\ln(V_s)$ (m/s)
0 - 0.5	9	119	0.127
0.5 - 1.5	9	126	0.086
1.5 - 2.5	8	182	0.014
2.5 - 3.5	8	201	0.086
3.5 - 4.5	6	205	0.240
4.5 - 5.5	4	220	0.292
5.5 - 6.5	3	208	0.069
6.5 - 7.5	1	233	--
7.5 - 8.5	1	291	--
8.5 - 9.5	1	285	--
9.5 - 10.5	1	234	--
10.5 - 11.5	1	194	--
11.5 - 12.5	1	279	--
12.5 - 13.5	1	304	--

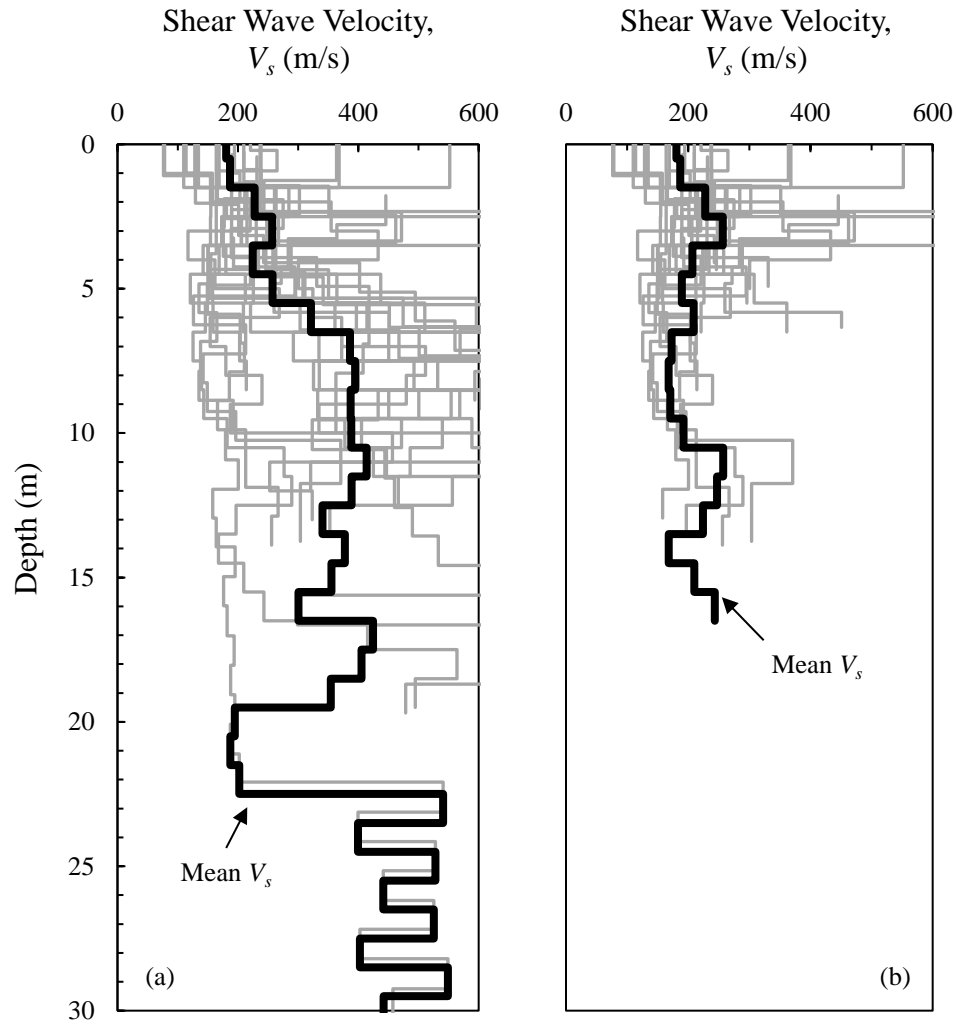


Figure D-9. Composite shear-wave velocity ( $V_s$ ) profiles for all Qtc sites, (a) including entire SCPT profiles, and (b) excluding portions of SCPT profiles in Marl.

Table D-9. Summary of shear wave velocity ( $V_s$ ) measurements above the Cooper Marl for Qtc sites.

Depth Range (m)	No. of $V_s$ Values	Geometric Mean $V_s$ (m/s)	Standard Deviation of $\ln(V_s)$ (m/s)
0 - 0.5	18	181	0.290
0.5 - 1.5	21	187	0.241
1.5 - 2.5	22	228	0.081
2.5 - 3.5	22	257	0.274
3.5 - 4.5	18	207	0.079
4.5 - 5.5	12	190	0.098
5.5 - 6.5	10	209	0.188
6.5 - 7.5	6	173	0.046
7.5 - 8.5	6	168	0.045
8.5 - 9.5	5	171	0.029
9.5 - 10.5	4	192	0.006
10.5 - 11.5	4	257	0.083
11.5 - 12.5	4	247	0.065
12.5 - 13.5	4	224	0.070
13.5 - 14.5	1	168	--
14.5 - 15.5	1	210	--
15.5 - 16.5	1	244	--

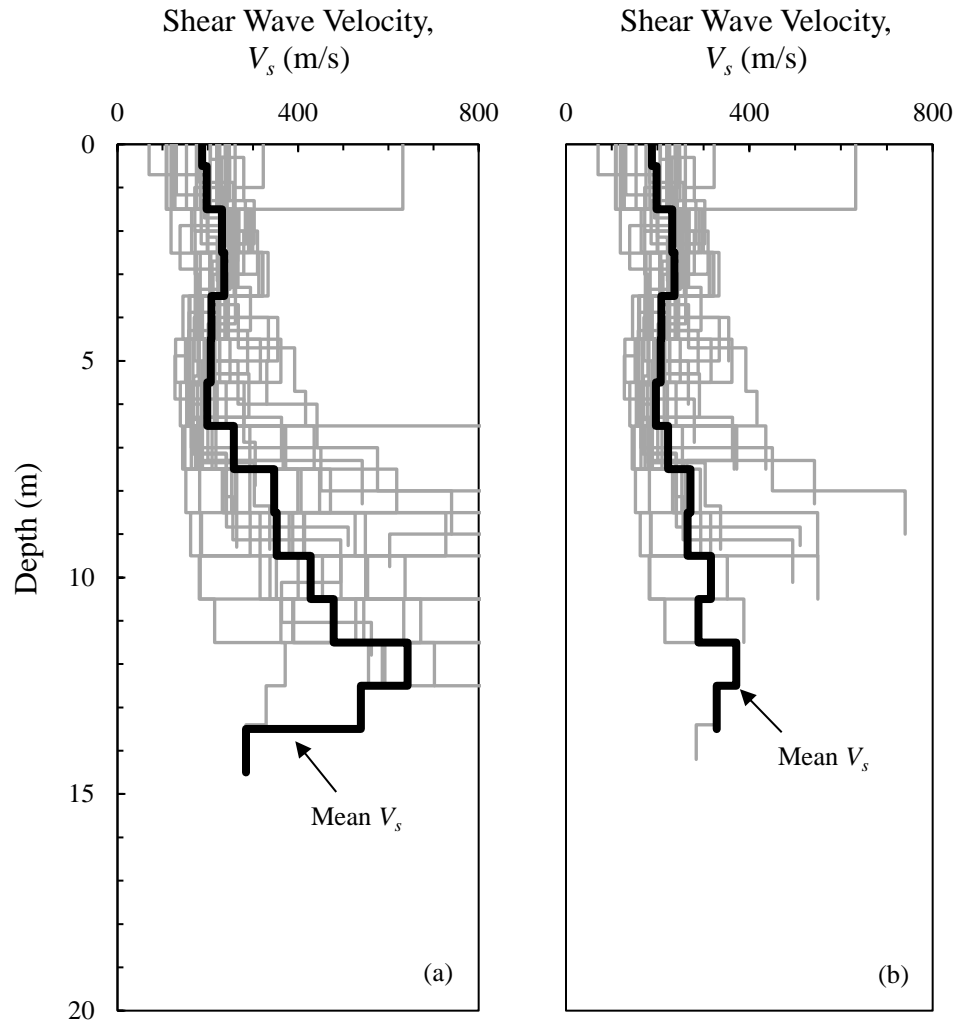


Figure D-10. Composite shear-wave velocity ( $V_s$ ) profiles for all Qlc sites, (a) including entire SCPT profiles, and (b) excluding portions of SCPT profiles in Marl.

Table D-10. Summary of shear wave velocity ( $V_s$ ) measurements above the Cooper Marl for Qlc sites.

Depth Range (m)	No. of $V_s$ Values	Geometric Mean $V_s$ (m/s)	Standard Deviation of $\ln(V_s)$ (m/s)
0 - 0.5	27	187	0.227
0.5 - 1.5	27	198	0.199
1.5 - 2.5	27	232	0.041
2.5 - 3.5	27	236	0.034
3.5 - 4.5	27	208	0.043
4.5 - 5.5	27	207	0.100
5.5 - 6.5	25	196	0.102
6.5 - 7.5	21	222	0.127
7.5 - 8.5	13	271	0.181
8.5 - 9.5	8	265	0.176
9.5 - 10.5	6	316	0.180
10.5 - 11.5	2	289	0.151
11.5 - 12.5	1	372	--
12.5 - 13.5	1	329	--

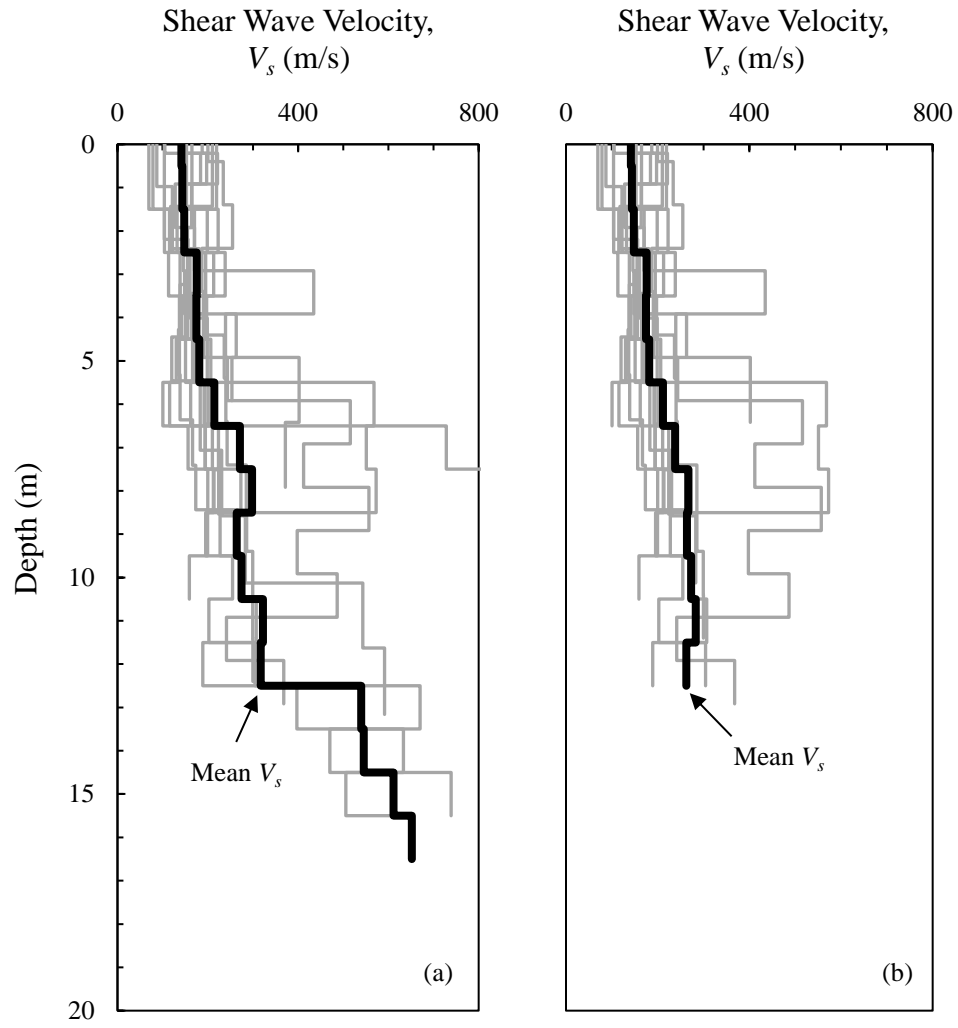


Figure D-11. Composite shear-wave velocity ( $V_s$ ) profiles for all Qpc sites, (a) including entire SCPT profiles, and (b) excluding portions of SCPT profiles in Marl.

Table D-11. Summary of shear wave velocity ( $V_s$ ) measurements above the Cooper Marl for Qpc sites.

Depth Range (m)	No. of $V_s$ Values	Geometric Mean $V_s$ (m/s)	Standard Deviation of $\ln(V_s)$ (m/s)
0 - 0.5	13	142	0.112
0.5 - 1.5	13	144	0.110
1.5 - 2.5	13	148	0.090
2.5 - 3.5	13	176	0.084
3.5 - 4.5	13	175	0.072
4.5 - 5.5	13	181	0.100
5.5 - 6.5	12	211	0.295
6.5 - 7.5	10	238	0.230
7.5 - 8.5	10	266	0.199
8.5 - 9.5	7	264	0.106
9.5 - 10.5	5	273	0.124
10.5 - 11.5	4	283	0.043
11.5 - 12.5	3	263	0.065

## **APPENDIX E**

### **LIQUEFACTION CHARACTERIZATION OF A 200,000-YEAR-OLD BEACH DEPOSIT NEAR CHARLESTON, SOUTH CAROLINA<sup>2</sup>**

---

<sup>2</sup> A similar version of this appendix is contained within Chapter 6 of the Ph.D. Dissertation by Bwambale (2018). Bwambale, B. (2018). “Reducing uncertainty in the assessment of aging effects on soil liquefaction.” *Ph.D. Dissertation*, Clemson University, Clemson, SC (pp. 89 – 121).



## **E.1 Introduction**

The August 31, 1886 Charleston earthquake is the largest historic event ever experienced on the east coast of the United States with significant physical damage to homes and infrastructure (Bollinger 1977; Côté 2006). Much of the damage in the greater Charleston, South Carolina region has been associated with liquefaction-induced ground failures (Dutton 1889). As indicated by Dutton (1889) and Heidari and Andrus (2012), several of the mapped ground failures occurred in the 200,000- to 240,000-year-old Ten Mile Hill beds sand facies (Qts).

Heidari and Andrus (2012) studied the liquefaction potential of Qts deposits as part of a broader liquefaction potential characterization of four major Pleistocene beach sand deposits covering the greater Charleston area. Their study involved an analysis of seismic piezocone penetration measurements at 13 sites within Qts. Eleven of the Qts seismic piezocone sites studied by Heidari and Andrus (2012) are located within a distance of 5 to 15 km from Woodstock fault zone, the assumed source of the 1886 earthquake. Eight of the eleven sites were part of an investigation that targeted areas of liquefaction during the 1886 Charleston earthquake.

The purpose of this chapter is to reevaluate the liquefaction potential of Qts deposits based on seismic piezocone and seismic cone penetration measurements at 46 sites located 5 to 30 km from Woodstock fault. This chapter also includes a back-calculation of an average correction factor to account for the effect of aging processes or diagenesis on liquefaction resistance of Qts, using estimates of peak horizontal ground accelerations for the 1886 earthquake.

## **E.2 Geology and Seismology**

As shown on the surficial geologic map presented in Figure E-1, the Ten Mile Hill beds clean sand facies (Qts) is one of seven dominant surficial Quaternary beach deposits covering the greater Charleston area. Surficial deposits of Qts are mostly found within a nearly 2 to 7 km wide band, extending in the northeast direction parallel to the Atlantic coast, at elevations ranging from 10 to 15 m (Weems and Lemon 1988, 1993). Estimates of the age of Qts vary from 200,000 to 240,000 years. Qts is generally underlain by the Ten Mile Hill beds clayey sand to clay facies and, to a lesser extent, the fossiliferous sand facies of the Ten Mile Hill beds and the Daniel Island beds. Below these Quaternary deposits lay the Tertiary Goose Creek limestone and the Ashley Formation of the Cooper Group, commonly known as Cooper Marl.

Also shown on the map in Figure E-1 is the trace of Woodstock fault zone as inferred by Durá-Gómez and Talwani (2009) from post 1886 Charleston earthquake macroscopic observations, analysis of instrumentally recorded seismic data between 1974 and 2004, and a geomorphic study of displaced river channels. The Woodstock fault zone is a complex system of faults consisting of a nearly 50 km long N30°E oriented, northwest dipping, right-lateral strike slip fault, and three short northwest-southeast striking, inward dipping, reverse faults. The Woodstock fault is divided into two steeply dipping north and south parts by an antidilatational compressional left step near Middleton Place.

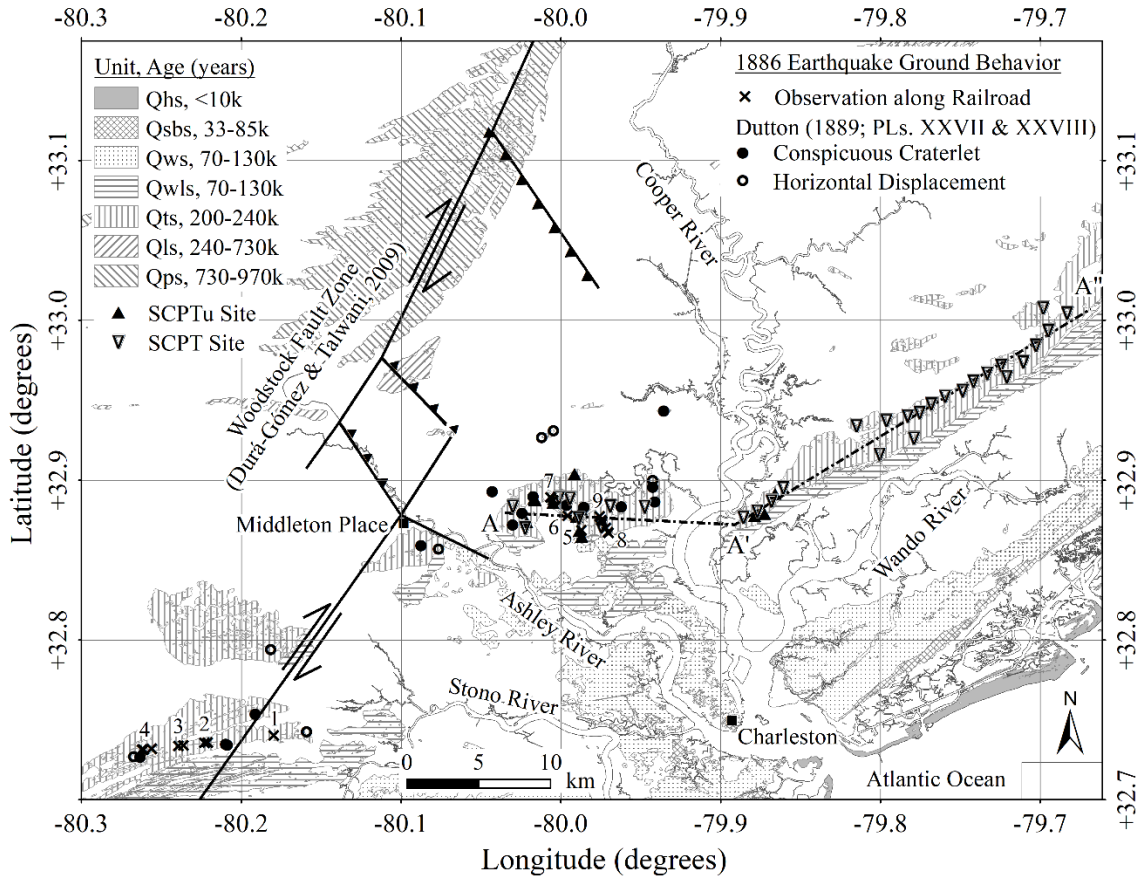


Figure E-1. Map of surficial beach sand deposits in the greater Charleston area and the inferred trace of the Woodstock fault zone (modified from Weems et al. 2014; Heidari and Andrus 2012). Plotted on the map are sites within Qts of conspicuous craterlets, horizontal displacements, areas of observed disturbance along railway lines, and SCPT and SCPTu.

The August 31, 1886 Charleston earthquake has been associated with the Woodstock fault. Extensive ground failures occurred near the fault zone, as well as in surrounding areas. Estimates of moment magnitude ( $M_w$ ) for this earthquake based on the analysis of ground shaking intensity and liquefaction case history data, range between 6.6 and 7.3 (Bakun and Hopper 2004; Hayati and Andrus 2008; Talwani and Gassman 2008; Heidari and Andrus 2010; Cramer and Boyd 2014).

Although Qts is one of the older geologic units, it experienced the most ground failures of the seven dominant beach deposits (Dutton 1889; Heidari and Andrus 2012). Plotted on the map in Figure E-1 are sites of major conspicuous craterlets (symbolized by solid circles) and horizontal ground displacements (symbolized by hollow circles) within Qts deposits mapped by Earle Sloan following the 1886 Charleston earthquake (Dutton 1889). Also shown on the map are locations of ground disturbances along railroads based on field notes by Earle Sloan and W. J. McGee, which are summarized in Table E-1 (Dutton 1889; Peters and Hermann 1986). Presented in Figures E-2 and E-3 are photographs showing ground failures at site numbers 5 and 6, respectively. It is observed that all mapped ground failures in Qts occurred within a distance less than 15 km from the inferred Woodstock fault.

Table E-1. Ground behavior in Qts along railroads during the 1886 Charleston earthquake (adapted from field notes by Earl Sloan and W. J. McGee as cited by Dutton [1889, pp. 283-294, 303-306] and Peters and Hermann [1986, pp. 18-26, 51-55, 62-64]).

Site No.	Mile Point	Latitude (degrees)	Longitude (degrees)	Elev. (m)	Description of Disturbance
<b>Charleston and Savannah Railroad</b>					
1	22.7	32.766956	-80.217870	---	End of continuous sinuous flexures; higher and firmer ground
2	25.0	32.762518	-80.259181	---	North of track 460 m, a 600-m-long fissure occurred with series of craterlets trending S80°W
3	25.11	32.762317	-80.261237	---	Road depressed 150 mm
	25.85	32.760746	-80.274371	---	Road depressed 460 mm over 90 m length
	26.02	32.760491	-80.277544	---	Slight sinuous flexures
4	26.95	32.758675	-80.294186	---	Road undermined by craterlet (2.4 m x 1.8 m and 3 m deep); adjacent ditches blocked with expelled sand from craterlets
	27.23	32.758123	-80.299309	---	Slight strain southward
	27.28	32.758095	-80.300259	---	Slight depression of 100 mm
	---	---	---	---	Disturbances were rare between mile points 27.57 and 28.71
<b>South Carolina Railroad</b>					
5	9.23	32.895391	-80.025498	6.02	Kink in track; train derailed and wrecked to the east; craterlets increasing in size and number
6	10.0	32.904402	-80.033925	7.62	Superstructure jammed to the south; craterlets reach greatest development both in size and number
7	10.85	32.914101	-80.043026	6.05	Track severely distorted to the southeast
	11.01	32.915894	-80.044700	5.81	Roadbed depressed 460 mm under 18 m chord
	11.02	32.915990	-80.044793	5.82	180 mm gap at joint; craterlets
<b>Northeastern Railroad</b>					
8	8.97	32.893700	-80.008483	---	Superstructure shifted 100 mm to the east
	9.0	32.894086	-80.008689	---	Long flexure with 100 mm ordinate to the east
	9.19	32.896686	-80.010039	13.72	Borrow pit excavation 1.8 m deep with many craterlets; water/sand ejected to heights of 4 m
9	9.51	32.900867	-80.012331	---	Fish-plates broken; rails parted 220 mm
	9.57	32.901694	-80.012775	---	Sliding frog (switch) sheared and shifted 200 mm to the south; craterlets abundant
	9.76	32.904114	-80.014075	4.57	Superstructure deflected to the east



Figure E-2. Derailed north-bound locomotive near Ten Mile Hill, mile point 9.23 on the South Carolina Railroad (Dutton 1889).



Figure E-3. View of craterlet at Ten Mile Hill on the South Carolina Railroad. (Photograph from “George L. Cook’s Earthquake Views”; courtesy of the South Caroliniana Library Archives, University of South Carolina, Columbia, South Carolina).

Based on an analysis of information along the railway lines in Table E-1, approximately 8 – 11% of the area covered by Qts along the railway lines experienced moderate to severe surface manifestations of liquefaction, 5 – 8% experienced minor liquefaction-related ground failures, and 83 – 84% did not show any liquefaction surface manifestations. It is assumed that areas within a radius of 80 meters (0.05 mile) from observed craterlets were classified as moderate to severe liquefaction. Areas were classified as minor liquefaction if fissures and depressions were present, and no liquefaction if there were no observed disturbances or craterlets along the railway lines.

Presented in Figure E-4 is a histogram showing distribution of mapped ground failures (Dutton 1889) within Qts deposits relative to Woodstock fault. The ground failures include nine horizontal displacements and fourteen conspicuous craterlets. Although Qts deposits extend to about 40 km from the fault, mapped ground failures occurred only within 15 km from the fault. Also plotted are ground disturbances observed along the three railway lines. The farthest point measured from the fault, on the railway lines within Qts deposits is about 11.4 km, and the combined length of the railway lines is approximately 17.8 km. It is noted that the observed ground failures along the railway lines are within regions where horizontal ground displacements and conspicuous craterlets occurred.

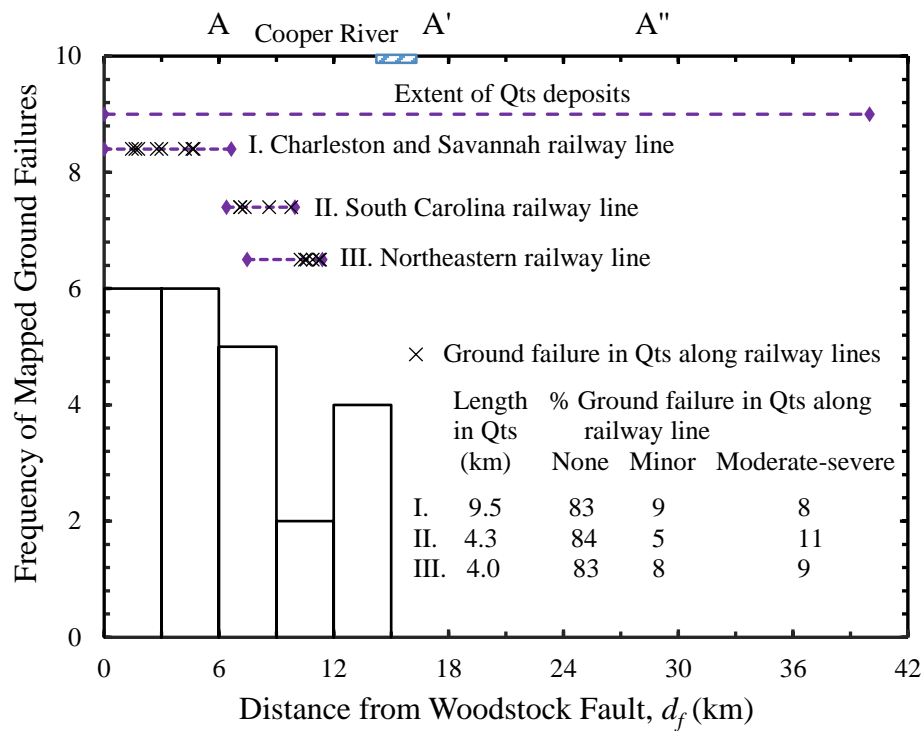


Figure E-4. Frequency of mapped ground failures during the 1886 Charleston earthquake presented in Dutton (1889), relative to Woodstock fault.

### **E.3 Cone Penetration Test Database**

Thirty seismic cone penetration test (SCPT) profiles and 17 seismic piezocone penetration test (SCPTu) profiles are used in this study to characterize the liquefaction probability of Qts deposits. The SCPT profiles are from the United States Geologic Survey online database ([earthquake.usgs.gov/research/cpt/data/charleston/](http://earthquake.usgs.gov/research/cpt/data/charleston/)) compiled by Thomas Holzer and his colleagues. Four of the 17 SCPTu profiles are from the database compiled by Mohanan (2006), and nine from Heidari (2011). The other four SCPTu profiles are from recent project reports by S&ME between March 2005 and March 2011. Locations of the 30 SCPT sites (open triangles) and 17 SCPTu sites (solid triangles) are shown on the map in Figure E-1.

Presented in Figure E-5 is a sample SCPTu profile. The cone tip resistance ( $q_c$ ) in Figure E-5(a) is corrected to account for the influence of pore-water pressure behind the cone. The friction ratio ( $FR$ ) in Figure E-5(b) is the sleeve friction divided by  $q_c$  multiplied by 100%. Shown in Figure E-5(c) are the hydrostatic pressure ( $u_0$ ) and the pore-water pressure ( $u_2$ ) measured by a transducer behind the cone tip. The shear wave velocity ( $V_s$ ) in Figure E-5(d) is based on the Snell's Law refracted ray path method (Kim et al. 2004). The ratio of measured  $V_s$  to estimated  $V_s$  ( $MEVR$ ) in Figure E-5(e) is based on the method recommended by Andrus et al. (2009), where estimated  $V_s$  is determined from normalized  $q_c$  and an empirical relationship for a 6-year-old clean sand deposit. The depth to top of Cooper Marl in Figure E-5(f) is inferred from  $q_c$ ,  $FR$ ,  $u_2$ ,  $V_s$  and  $MEVR$  profiles using the following general criteria: 1)  $q_c$  is fairly constant; 2)  $FR$  is fairly constant and less than 2.0; 3)  $u_2$  is at least 1000 kPa; (4)  $V_s$  is at least 300 m/s; and (5)  $MEVR$  is greater than or equal to 2.0.

The Snell's Law refracted ray path method was employed to calculate (and in some cases re-calculate) values of  $V_s$ , where sufficient information was available for the calculation. Sufficient information was available for all 30 SCPT and many of the SCPTu profiles. Kim et al. (2004) recommended the Snell's law ray path method because the simple straight ray path method can provide unreliable values of  $V_s$ , particularly near the ground surface where a great stiffness contrast exists between two adjacent layers. For the available Qts data, both methods generally give estimates of  $V_s$  that are within 2% of each other below the depth of 3-4 times the source-to-hole offset, depending on the offset distance and  $V_s$  measurement interval depth. Slightly larger differences were observed for deeper layers where greater layer stiffness contrasts exist. Appendix D presents summary  $V_s$  profiles and tables of sites within Qts deposits.

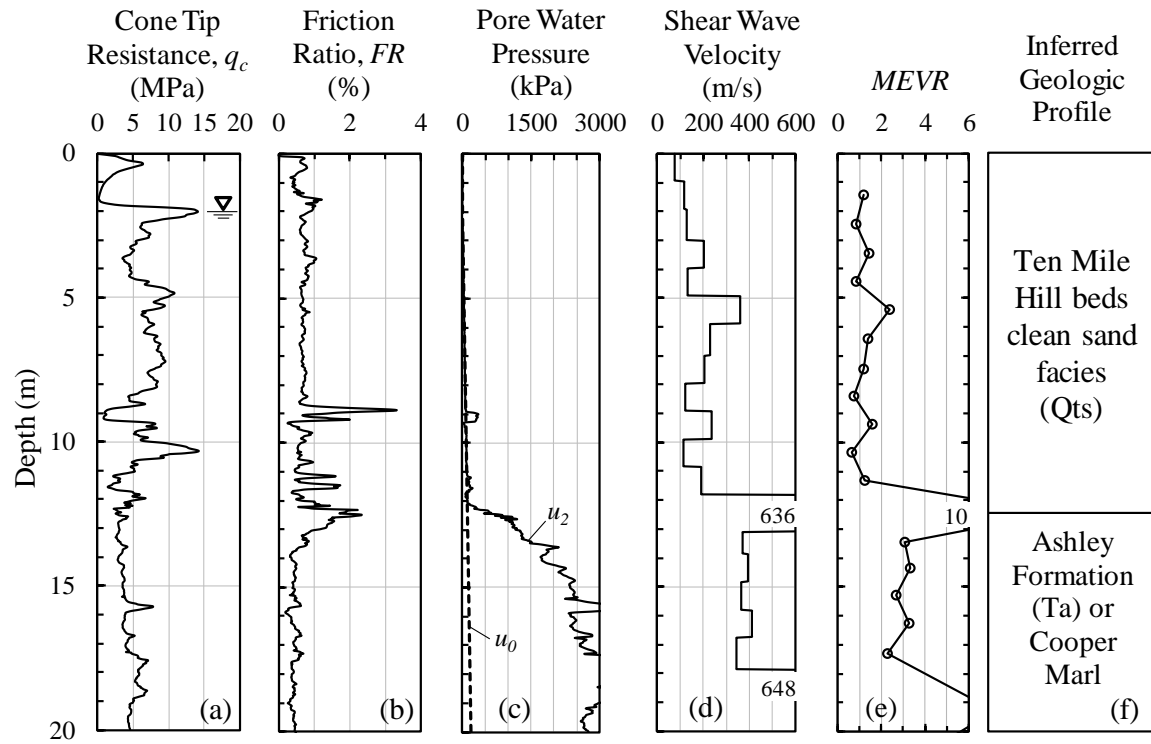


Figure E-5. Example SCPTu for Site No. Qts36.



Figure E-6 shows two-dimensional profiles of the ground surface elevation, the top of Cooper Marl elevation, and the groundwater table elevation along alignment A-A'-A" shown in Figure E-1. Ground surface elevation information was available for 35 of the 47 sites. For the other 12 sites, ground surface elevations were estimated using Google Earth online software (accessed July 2017). Computed elevations of the top of Cooper Marl generally agree with elevations indicated in the geologic cross sections provided in Weems and Lemon (1988, 1993). It can be seen in Figure E-6 that ground surface elevations in Qts range from 9 m to 18 m; groundwater table elevations range from 7 to 12 m, but may be deeper in areas of active pumping; and top of Cooper Marl elevations range from 7 m to 15 m. The net result is a general thickening of Quaternary sediments going from A to A".

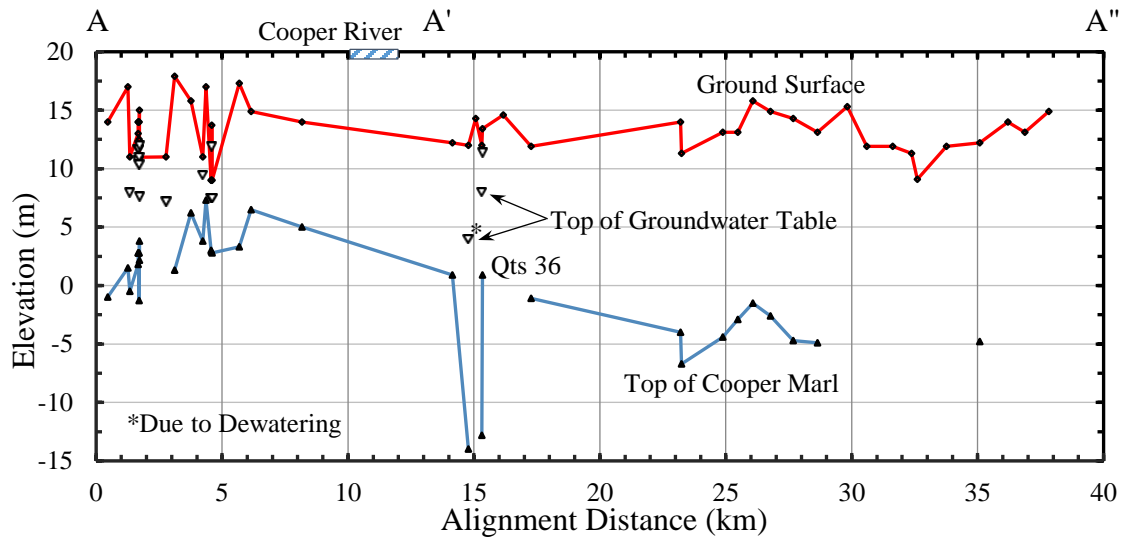


Figure E-6. Variation in elevations of the ground surface, the top of Cooper Marl and the top of groundwater table along the alignment A-A'-A" shown in Figure E.1.

Figure E-7 shows the variation of average *MEVR* for selected Qts layers with distance from Woodstock fault ( $d_f$ ) and depth to center of layer ( $z$ ). The layers were selected using the following criteria: (1) layer is below groundwater table; (2)  $q_c$ ,  $FR$ ,  $V_s$ , and soil behavior type index are fairly constant within the layer; (3) layer is at least 2 m thick; and (4) at least 80% of the  $V_s$  measurement interval is within the selected layer. For sites where enough information was not available to recalculate  $V_s$  using the Snell's law ray path method, layers were selected below 3 m to offset the limitation of poor  $V_s$  estimates in the near surface layers using the straight ray path method. The very small  $R^2$  associated with the best-fit regression line suggests that there is no significant relationship between *MEVR* and distance from Woodstock fault. The relatively strong correlation ( $r^2 = 0.32$ ) obtained with the Heidari and Andrus (2012) data could be the result of bias in the sampling of liquefaction sites and limited data. About 80% of the Heidari and Andrus (2012) data points were obtained from sites where investigations targeted areas of surface manifestations of liquefaction. Thus, it is concluded that no strong correlation exists between *MEVR* and distance from Woodstock fault.



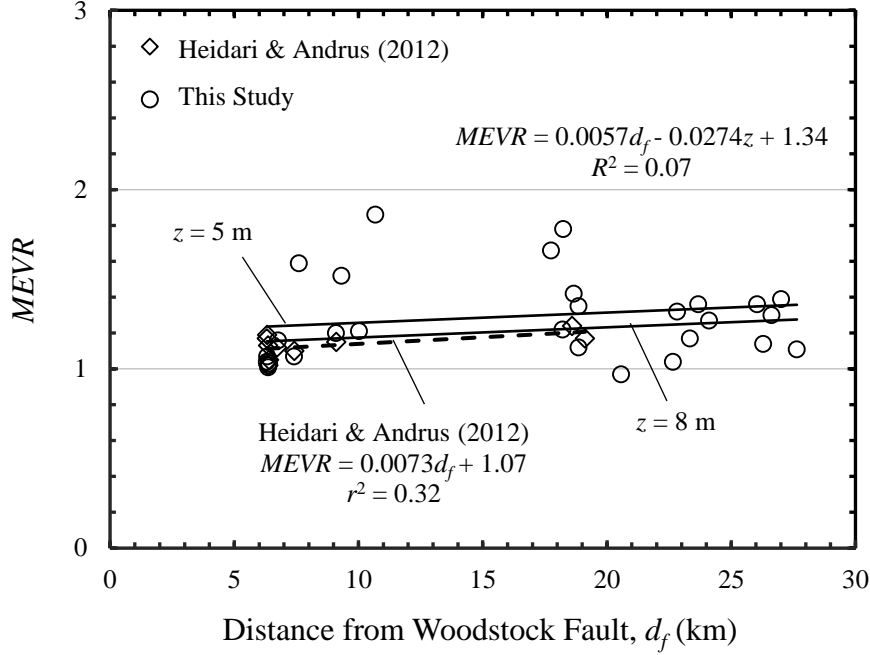


Figure E-7. Average *MEVR* for selected layers versus distance from Woodstock fault ( $d_f$ ) and depth to the center of layer ( $z$ ).

#### **E.4 Liquefaction Susceptibility Assessment**

Liquefaction susceptibility is the relative likelihood a soil would liquefy during intense earthquake shaking. The degree of susceptibility for a given soil depends on several factors, including grain size and plasticity (e.g., Youd and Hoose 1977; Seed and Idriss 1982; Robertson and Wride 1998; Youd et al. 2001; Bray et al. 2004; Boulanger and Idriss 2006), depositional environment and deposit age or degree of diagenesis (e.g., Youd and Hoose 1977; Youd and Perkins 1978; Seed 1979; Hayati and Andrus 2009), groundwater table depth and degree of saturation (e.g., Youd and Hoose 1977; Cox 2006; Okamura et al. 2006; Hatanaka and Masuda 2008; Hossain et al. 2013), and density (e.g., Seed and Idriss 1971; Boulanger and Idriss 2006). Soils that are above the groundwater table or too clay-rich or very dense are generally considered to be non-susceptible to liquefaction.

A comparison of relative overall liquefaction susceptibility between sites within Qts is possible using the liquefaction potential index (*LPI*) and assuming the same amount of ground shaking at all sites. Iwasaki et al. (1982) defined *LPI* by:

$$LPI = \int_0^{20} Fw(z)dz \quad (E.1)$$

where  $F$  is a function of factor of safety ( $FS$ ) given by  $F = 1 - FS$  for  $FS \leq 1$  and  $F = 0$  for  $FS > 1$ ;  $w(z)$  is a depth weighting factor given by  $w(z) = 10 - 0.5z$ ; and  $z$  is depth below the ground surface

in meters. As indicated by Equation E.1,  $LPI$  is a cumulative index that considers layers in the topmost 20 m and the proximity of liquefiable layers to the ground surface.

Figure E-8 shows a summary of the  $LPI$  calculations for SCPTu Qts36 based on  $M_w$  of 7.0 and a peak horizontal ground acceleration ( $a_{max}$ ) of 0.25g. The two profiles shown in Figure E-8(a) are cone tip resistances normalized to an overburden stress of 1 atmosphere ( $q_{c1N}$ ) and corrected for the influence of fines content ( $q_{c1Ncs}$ ) based on the procedures by Youd et al. (2001) and the stress exponent relationship recommended by Robertson (2009). The soil behavior type index ( $I_c$ ) in Figure E-8(b) was determined using the relationships of Robertson and Wride (1998) and the update of Zhang et al. (2002). Soils with  $I_c > 2.6$  are assumed in this study to be too clay-rich to liquefy. The age correction factor ( $K_{DR}$ ) profile shown in Figure E-8(c) is derived from  $MEVR$  [see Figure E-5(e)] and the relationship recommended by Hayati and Andrus (2009), where  $K_{DR} = 1.08^{MEVR - 0.08}$ .

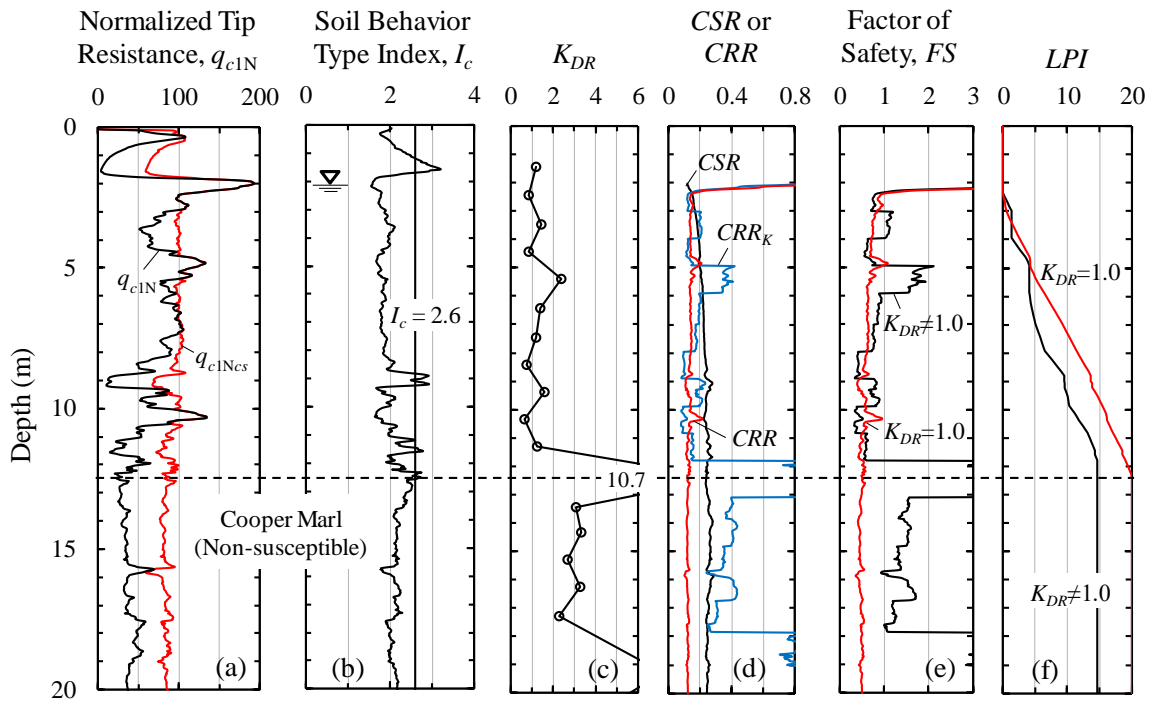


Figure E-8. Example calculation of liquefaction potential index ( $LPI$ ) for SCPTu Site No. Qts36 assuming  $a_{max} = 0.25g$  and  $M_w = 7.0$ .

The cyclic stress ratio ( $CSR$ ) and cyclic resistance ratio ( $CRR$ ) shown in Figure E-8(d) were estimated using the CPT-based triggering procedure of Boulanger and Idriss (2016), assuming the 15% probability of liquefaction curve.  $CRR_K$  is the  $CRR$  multiplied by  $K_{DR}$ . As shown in Figure E-8(e),  $FS$  (or  $CRR/CSR$ ) without  $K_{DR}$  correction is less than 1.0 for most of the profile below the groundwater table, including the Cooper Marl. The Cooper Marl classifies as silty clay to clayey silt, and is generally considered non-susceptible to liquefaction (Li et al. 2007; Hayati and Andrus 2008). With a  $K_{DR}$  correction,  $FS$  is correctly predicted to be above 1.0 within the Cooper Marl.

This observation provides additional strong support for a  $K_{DR}$  correction for accurate prediction of liquefaction behavior.

Figure E-8(f) shows profiles of computed  $LPI$  without  $K_{DR}$  correction (i.e.,  $K_{DR} = 1.0$ ), and with  $K_{DR}$  correction (i.e.,  $K_{DR} \neq 1.0$ ).  $LPI$  for Site Qts36 with the assumed ground shaking is 20.1 without  $K_{DR}$  correction. With  $K_{DR}$  correction,  $LPI$  reduces to 14.7.

Because the Cooper Marl is assumed to be non-susceptible to liquefaction,  $LPI$  is computed down to either the top of Cooper Marl or 20 m depth, whichever is shallower. SCPT measurements at 7 of the 47 sites do not extend into the Cooper Marl or 20 m. For the five sites where SCPT profiles extend within 2 m above the Cooper Marl based on available 1:25,000 scale geologic maps, the missing portion of the data is assumed similar to the last 2 m of the profile for  $LPI$  calculations. Site Qts20, which extends down to 18 m has high  $V_s$  and/or  $MEVR$  values below 14 m, resulting in zero contribution to  $LPI$ . Hence, this site is used in the  $LPI$  calculations as it is. Site Qts41 is not used in the  $LPI$  calculations because there are no  $V_s$  data above 3 m, which makes it difficult to compute  $MEVR$ -based  $K_{DR}$ .

Figure E-9 shows the variation of computed  $LPI$  values based on constant seismic loading with distance from Woodstock fault, the likely source area of the 1886 earthquake. The sites assessed by Heidari and Andrus (2012) are denoted by open triangles, and the remaining sites are denoted by open circles. Overall, the plotted values of  $LPI$  exhibit significant scatter and only a slight decreasing trend with increasing distance from the fault. This result is different from the strong trend exhibited by the sites first considered by Heidari and Andrus (2012), where eleven of the thirteen sites lie within a distance of 5 to 10 km from the fault and eight are the results of investigations that targeted sites of liquefaction in 1886. Another factor contributing to the weak trend with respect to distance to the fault is the thickening of Quaternary sediments at distances from the fault over 15 km (see Figure E-6), which would likely result in higher  $LPI$  values.

Figure E-10 presents the frequency distribution of computed  $LPI$  values, and the probability density function (PDF) derived by assuming  $LPI$  is lognormally distributed. For the plotted data based on the assumed uniform loading, the mean, median and standard deviation range of the  $LPI$  values are 7.4, 7.5, and 2.5-12.3, respectively.

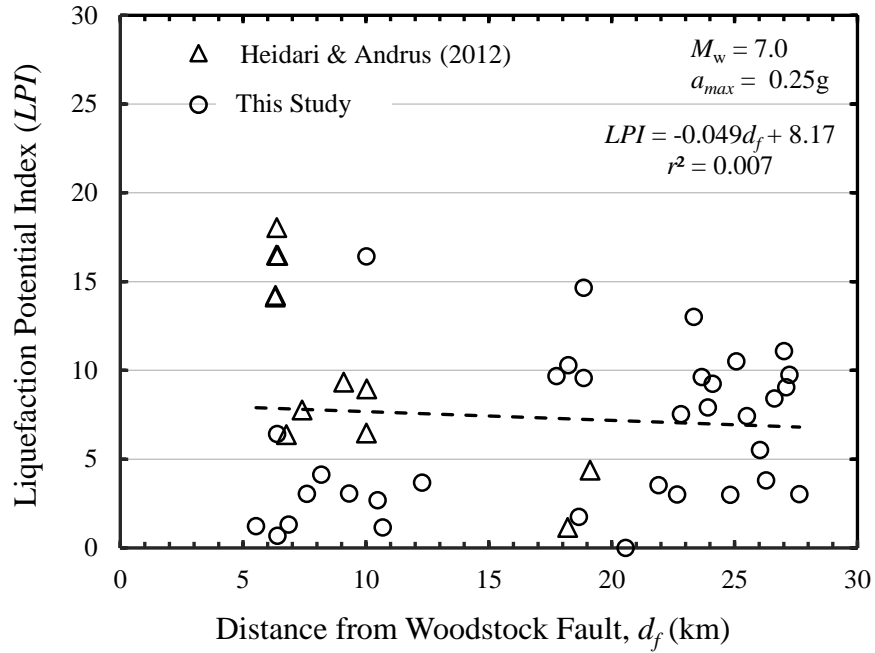


Figure E-9. Variation of  $LPI$  with distance from Woodstock fault for Qts sites assuming  $a_{max} = 0.25g$  and  $M_w = 7.0$ .

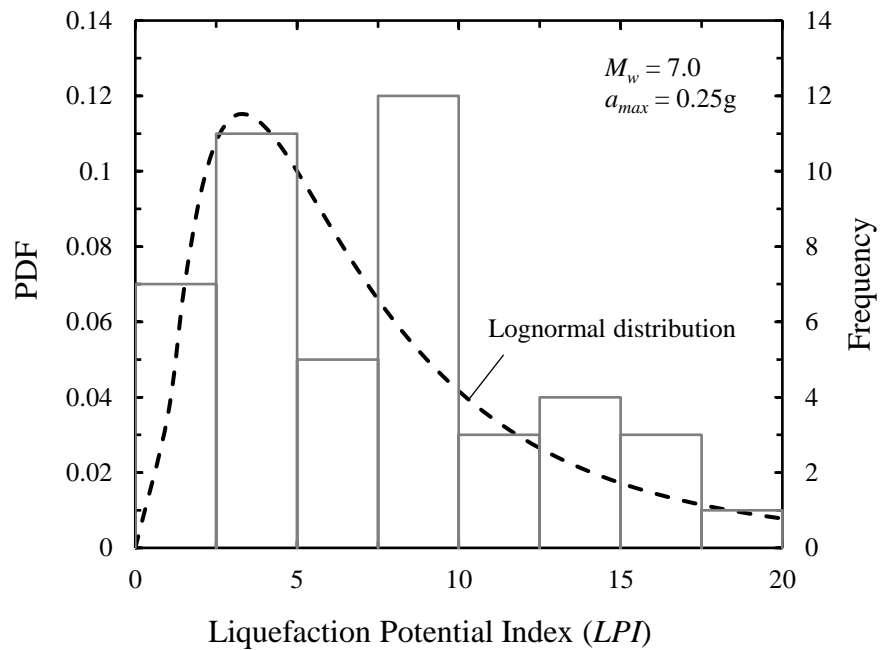


Figure E-10. Distribution of  $LPI$  for Qts assuming  $a_{max} = 0.25g$  and  $M_w = 7.0$ .

## **E.5 Liquefaction Potential Assessment**

Liquefaction potential is the likelihood that triggering of liquefaction will occur in a susceptible soil for a given seismic loading. Liquefaction potential, therefore, depends on the level of earthquake loading, often represented by the cyclic stress ratio ( $CSR$ ), and the site conditions or the soil's ability to resist earthquake loading, often represented by the cyclic resistance ratio ( $CRR$ ). Triggering of liquefaction is assumed to occur when  $CSR$  exceeds  $CRR$  or when factor of safety against liquefaction ( $FS$ ), which is defined as  $CRR$  divided by  $CSR$ , drops below the value of 1.0. Liquefaction potential can be evaluated by linking computed  $FS$  to field observations during earthquakes, such as ejection of liquefied material, ground deformations, or absence of surficial manifestations of liquefaction. Frameworks that relate field observations to  $FS$  exist, including the commonly used liquefaction potential index (Iwasaki et al. 1982), probability of liquefaction (Chen and Juang 2000), liquefaction severity number (van Ballegooy et al. 2012), and the most recently proposed Ishihara-inspired liquefaction potential index (Maurer et al. 2015b). The liquefaction potential index ( $LPI$ ) framework proposed by Iwasaki et al. (1982) is adopted in this study to evaluate liquefaction potential of Qts.

The threshold  $LPI$  separating no liquefaction and liquefaction surface manifestations ( $LPI_t$ ) is often assumed to be 4-6 for sands (e.g., Iwasaki et al. 1982; Toprak and Holzer 2003; Maurer et al. 2015a) and 10.5-15.5 for silts (Maurer et al. 2015a), depending on the liquefaction triggering procedure employed. Based on the triggering procedure by Idriss and Boulanger (2008) and the liquefaction severity criteria for Christchurch developed by Green et al. (2014), Maurer et al. (2015a) reported  $LPI_t$  of 6 for sandy soils (i.e.,  $I_{c10} < 2.05$ ), and 15.5 for predominantly silty soils (i.e.,  $I_{c10} \geq 2.05$ ).  $I_{c10}$  is defined as the average  $I_c$  in the topmost 10 m of the SCPT profile. For Qts sites (based on the top 10 m and above Marl),  $I_{c10}$  ranges between 1.78 and 2.59, with mean of 2.13 and standard deviation of 0.19. Because only discrete values of  $LPI_t$  are available (i.e.,  $LPI_t = 6$  for  $I_{c10} < 2.05$ , and  $LPI_t = 15.5$  for  $I_{c10} \geq 2.05$ ),  $LPI_t$  values of either 6 or 15.5 based on  $I_{c10}$  for each site are averaged to provide a weighted threshold of 12 for Qts.

A very rough initial validation of the  $LPI_t$  of 12 for Qts is possible based on  $a_{max}$  estimates of the 1886 earthquake at Qts sites and reported observed ground behavior during the 1886 earthquake. Figure E-11(a) shows profiles of  $a_{max}$  inferred from the study of Silva et al. (2003) and the results of a hard rock ground motion prediction and a hard rock-to-ground surface SHAKE analysis performed by Professor Chris Cramer at the University of Memphis for this study. The SHAKE analysis values of  $a_{max}$  were estimated based on the southeast segment of Woodstock fault (see Figure E-1) and the ground motion prediction equation suite and weights from the 2014 USGS national seismic hazard mapping project model (Petersen et al. 2014). The median site amplification factors were determined from the soil response models based on mean  $V_s$  profiles for Qts and the South Carolina dynamic soil properties ( $G/G_{max}$  curves) presented in Zhang et al. (2005, 2008). The  $a_{max}$  values based on SHAKE analysis are lower than values based on Silva et al. (2003). This discrepancy is likely a result of differences in the assumed  $V_s$  profiles, attenuation relationships, site response models,  $G/G_{max}$  curves, and earthquake magnitudes.

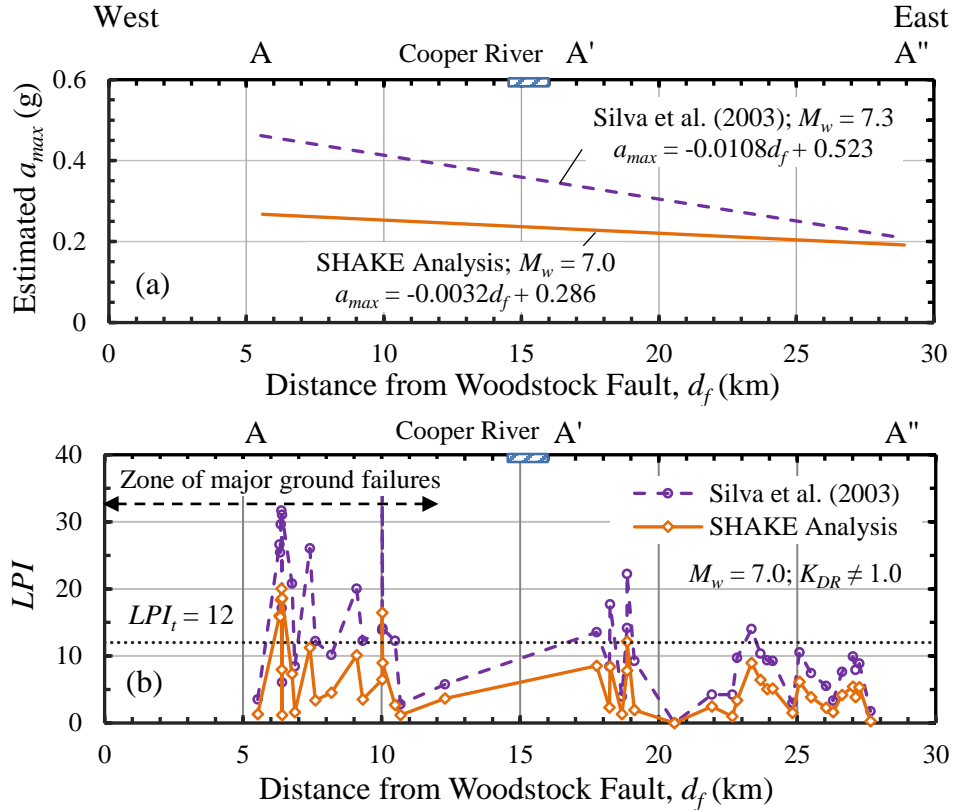


Figure E-11. Variation of: (a) estimated  $a_{max}$ , and (b)  $LPI$  based on liquefaction assessment procedure of Boulanger and Idriss (2016), assuming  $K_{DR} = 1.08MEVR - 0.08$ , with distance from Woodstock fault.

Figure E-11(b) shows profiles of  $LPI$  based on  $a_{max}$  in Figure E-11(a) and the liquefaction triggering procedure of Boulanger and Idriss (2016), assuming the  $MEVR$ -based age correction factors proposed by Hayati and Andrus (2009). Repeating the calculations using the procedure of Idriss and Boulanger (2008) results in  $LPI$  values that are on average 5 – 15% greater than values obtained using the Boulanger and Idriss (2016) procedure. Considering sites on the western side of the Cooper River plotted in Figure E-11(b) (excluding seven targeted sites of liquefaction in 1886), 36% of the sites have  $LPI$  greater 12 based on  $a_{max}$  values from Silva et al. (2003), and 7% of these sites have  $LPI$  greater 12 when  $a_{max}$  values from the SHAKE analysis are considered. Predicted liquefaction based on  $a_{max}$  values from the SHAKE analysis are closer to observed ground behavior during the 1886 earthquake (i.e., 8 – 11% of the area along the railway lines within Qts experienced moderate to severe liquefaction), than predicted liquefaction based on  $a_{max}$  values from Silva et al. (2003).

## E.6 Liquefaction Probability Curves

As proposed by Holzer et al. (2006, 2009), liquefaction potential of a given surficial geologic unit can be assessed in terms of probability of surface manifestations of liquefaction

based on computed  $LPI$  exceeding a threshold  $LPI$  value. The probability that computed  $LPI$  will equal or exceed an assumed threshold value is calculated assuming different earthquake loading scenarios and a liquefaction probability curve is generated by plotting probability as a function of earthquake loading. Holzer et al. (2011) used this approach to develop liquefaction probability curves for fourteen different surficial geologic units within the United States, and Heidari and Andrus (2012) applied a similar approach in their evaluation of the liquefaction potential of four beach sands near Charleston, South Carolina, including Qts, with fewer sites.

Figure E-12 presents liquefaction probability curves for Qts, with and without correction for the effect of diagenesis on liquefaction resistance, based on a weighted threshold  $LPI$  of 12.  $LPI$  values were computed for a given earthquake magnitude and  $a_{max}$  ranging from 0.1 to 0.7g at increments of 0.02g up to 0.3g, and increments of 0.1g thereafter. The process was then repeated for the  $M_w$  range of 5 to 9 at 0.5 increments. The probability of  $LPI \geq 12$  ( $P_{LPI \geq 12}$ ) was calculated assuming  $LPI$  is lognormally distributed. Although it has been argued that the lognormal distribution assumption may not be appropriate for lower  $M_w$  and  $a_{max}$  values where  $LPI$  of zero are obtained (Heidari and Andrus 2012), results indicate that computing probabilities based on experimental cumulative distribution for cases with zero  $LPI$  values does not make any significant difference in the resulting probability curve. Thus, the lognormal distribution was assumed throughout the calculations.

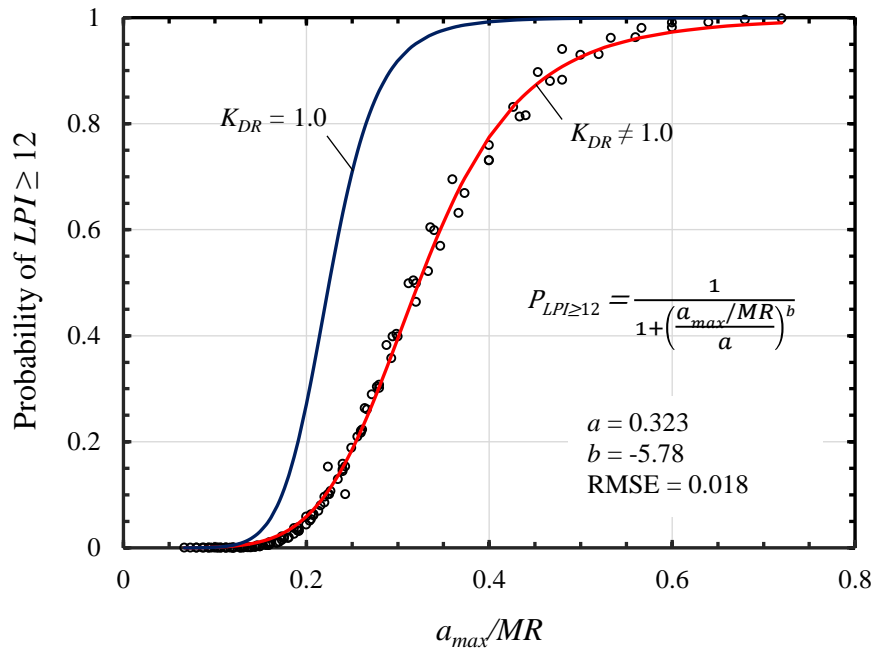


Figure E-12. Liquefaction probability curves for Qts with and without correction for the effect of diagenesis, assuming  $LPI$  values are lognormally distributed, measured groundwater table depths, and a cutoff  $I_c$  of 2.60 for non-susceptible clay-rich soils.

The probability curves plotted in Figure E-12 can be estimated using a two-parameter logistic model:

$$P_{LPI \geq 12} = \frac{1}{1 + \left( \frac{a_{\max}/MR}{a} \right)^b} \quad (\text{E.2})$$

where  $MR$  is the magnitude ratio given by  $7.5/M_w$ ; and coefficients  $a$  and  $b$  are the model parameters. As shown in Figure E-12, significantly greater probabilities are obtained when correction for aging or diagenesis is not applied. In addition, the rate at which probability of liquefaction increases with increasing earthquake loading is higher without aging correction, as shown by the steeper slope of the curve.

Liquefaction probability curves were also developed for Qts varying the depth to top of Cooper Marl ( $C$ ) and the depth to top of groundwater table ( $W$ ). Shown in Figure E-13 are probability curve fittings of Equation E.2, assuming a depth to Marl of 15 m and various depths to the groundwater table. It is observed that liquefaction potential decreases as depth to groundwater table increases. The curves for  $W \leq 2$  m are nearly parallel to each other, with probability increasing at almost the same rate as  $a_{\max}$  increases. However, at greater groundwater table depths (i.e.,  $W > 2$  m), the slope of the probability curves decreases indicating greater reduction in liquefaction potential as  $W$  increases. Similar curves were developed for depths to Marl ranging from 2.5 m to 20 m at 2.5 m increments (see Bwambale 2018, Appendix E). Presented in Table E-2 are the curve fitting parameters for all groups of depth to Marl and groundwater table. These liquefaction probability curves can be used to create a regional probabilistic liquefaction hazard map for Qts.

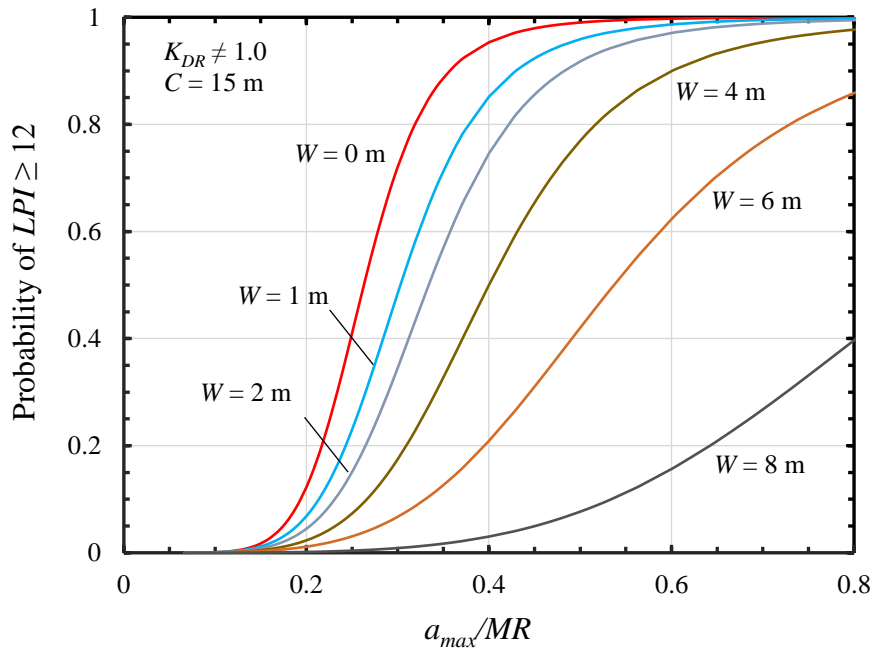


Figure E-13. Liquefaction probability curves assuming depth to top of Cooper Marl ( $C$ ) of 15 m, and depths to groundwater table ( $W$ ) of 0, 1, 2, 4, 6, and 8 m.



Table E-2. Logistic model parameters for fitted liquefaction probability curves.

Depth to Top of Marl, $C$ (m)	Depth to Groundwater Table, $W$ (m)					
	0	1	2	4	6	8
Parameter $a$						
2.5	1.161	NA	NA	NA	NA	NA
5	0.490	0.707	0.978	NA	NA	NA
7.5	0.344	0.445	0.528	0.938	NA	NA
10	0.266	0.319	0.359	0.482	0.912	NA
12.5	0.261	0.305	0.340	0.424	0.598	1.163
15	0.263	0.303	0.334	0.400	0.537	0.880
17.5	0.246	0.277	0.301	0.353	0.445	0.686
20	0.248	0.279	0.303	0.353	0.438	0.673
Parameter $b$						
2.5	-3.34	NA	NA	NA	NA	NA
5	-4.34	-3.98	-3.26	NA	NA	NA
7.5	-5.21	-4.66	-4.14	-3.05	NA	NA
10	-5.49	-5.04	-4.79	-3.99	-2.99	NA
12.5	-6.08	-5.70	-5.49	-4.93	-3.95	-3.11
15	-7.19	-6.29	-5.97	-5.40	-4.52	-3.55
17.5	-8.28	-7.69	-7.66	-7.36	-6.62	-4.50
20	-8.04	-7.39	-7.32	-7.05	-6.52	-4.40

## **E.7 Back-Calculated $K_{DR}$ Based on 1886 Earthquake**

The effect of diagenesis on liquefaction resistance can be quantified by comparing computed  $LPI$  with an estimated threshold  $LPI$  for surface manifestations of liquefaction at sites with known earthquake loading and well documented field observations during an earthquake (e.g., Hayati and Andrus 2008; Heidari and Andrus 2010; Maurer et al. 2014; Bwambale et al. 2017; Bwambale and Andrus 2017). The correction factor for diagenesis ( $K_{DR}$ ) is obtained by adjusting the value applied to  $CRR$  until computed  $LPI$  matches an assumed threshold value.

As indicated in Figures E-1 and E-4, liquefaction-induced ground failures within Qts during the 1886 Charleston earthquake occurred closest to the fault, and none have been reported on the eastern side of the Cooper River. It is therefore assumed that none-to-minor surface manifestations of liquefaction occurred beyond 15 km from the fault during the 1886 earthquake. Thus,  $LPI$  values at sites located on the eastern side of the Cooper River are expected to be less than the estimated threshold separating none-to-minor and moderate-to-severe surface manifestations of liquefaction. The weighted threshold  $LPI$  for Qts based on the  $I_{c10}$ -calibration of Maurer et al. (2015a) is 12.

Figure E-14(b) presents computed  $LPI$  at all Qts sites without correction for the effect of diagenesis. Based on  $a_{max}$  values from Silva et al. (2003), 68% of the sites have  $LPI$  greater than the assumed threshold. Based on  $a_{max}$  from the SHAKE analysis performed for this study, 44% of the sites have  $LPI$  values that exceed the threshold. These findings incorrectly suggest that moderate to severe surface manifestations of liquefaction occurred at the sites during the 1886 earthquake if no diagenesis correction is applied.

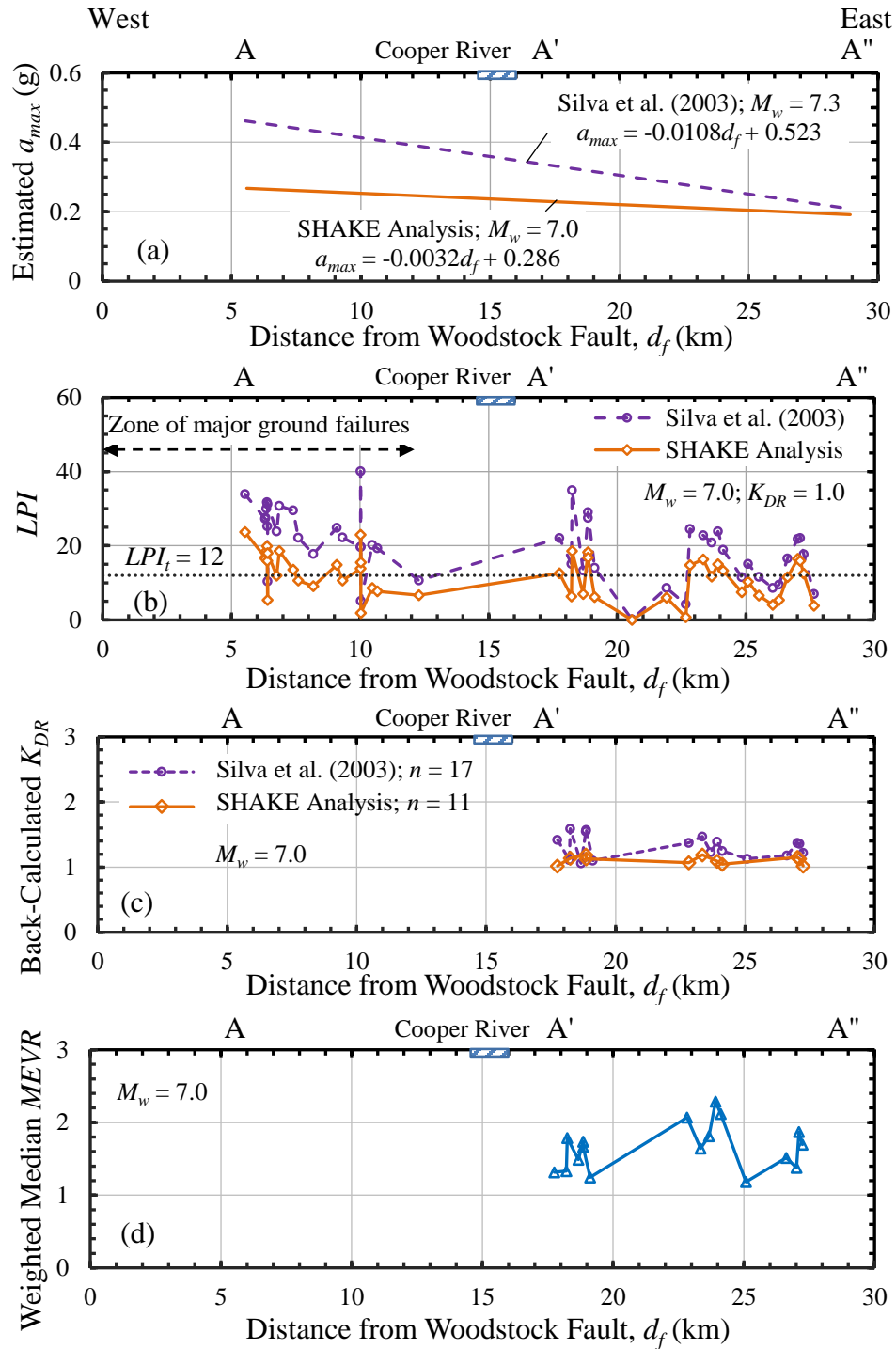


Figure E-14. Variation of: (a) estimated  $a_{max}$ , and (b)  $LPI$  based on liquefaction assessment procedure of Boulanger and Idriss (2016), (c) back-calculated  $K_{DR}$  based on a threshold  $LPI$  of 12, and (d) weighted median  $MEVR$ , with distance from Woodstock fault.

To match predicted liquefaction with field observations,  $K_{DR}$  is back-calculated for sites where liquefaction is over-predicted. The back-calculated  $K_{DR}$  values plotted in Figure E-14(c) range between 1.02 and 1.19, with average of 1.11 and standard deviation of 0.06, assuming  $a_{max}$  from SHAKE analysis. An average  $K_{DR}$  of 1.32 and standard deviation of 0.17 are obtained when  $a_{max}$  values based on Silva et al. (2003) are assumed. It is important to note that this approach estimates the minimum possible  $K_{DR}$  value because  $LPI$  for sites with none-to-minor surface manifestations of liquefaction can be any number less than the assumed threshold value.

Plotted in Figure E-14(d) are weighted median  $MEVR$  values. Median  $MEVR$  at each site is weighted according to relative contribution of each  $V_s$  measurement interval to  $LPI$ . Thus,  $MEVR$  values for layers with zero  $LPI$  are not used to compute median  $MEVR$ . The  $MEVR$  plotted in Figure E-14(d) range between 1.24 and 2.45, with a median value of 1.69.

Figure E-15 shows a comparison of the back-calculated  $K_{DR}$  for Qts with published relationship and data by Hayati and Andrus (2009). The open square represents the  $MEVR$ - $K_{DR}$  data pair based on  $a_{max}$  values from Silva et al. (2003). The open diamond represents the  $MEVR$ - $K_{DR}$  data pair based on  $a_{max}$  values from the SHAKE analysis. Although the Qts points plot below the Hayati and Andrus (2009) relationships, they are within the foreseeable scatter of the data. The  $MEVR$ - $K_{DR}$  data pairs for Qts plotted in Figure E-15 depend on: ability of the  $LPI$  criteria to correctly account for effects of nonliquefiable surface layers, accuracy of the earthquake loading inputs (i.e.,  $M_w$  and  $a_{max}$ ), and the assumed  $LPI$  threshold for surface manifestations of liquefaction.

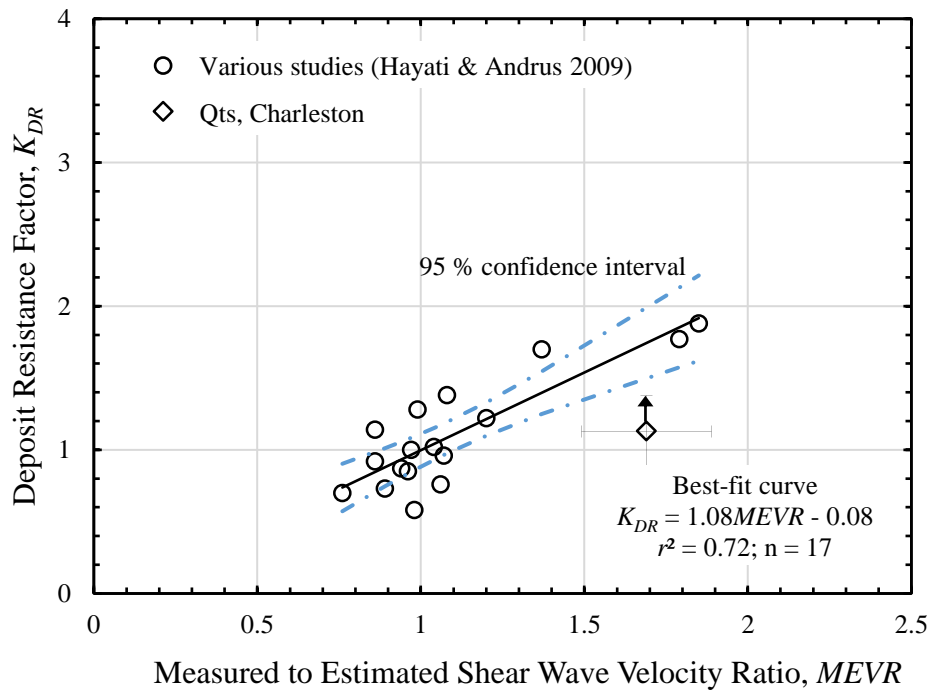


Figure E-15. Back-calculated  $K_{DR}$  for Qts compared with relationship and data by Hayati and Andrus (2009).

## **E.8 Summary**

The liquefaction resistance of the Ten Mile Hill beds surficial beach deposits in the Charleston area was characterized based on seismic cone penetration testing at 46 sites located 5 to 28 km from the Woodstock fault. The Snell's Law refracted ray path method was employed to calculate (and in some cases re-calculate) values of small-strain shear wave velocity ( $V_s$ ), where sufficient information was available for the calculation. Computed ratios of measured to estimated  $V_s$  ( $MEVR$ ) for selected layers, and liquefaction potential index ( $LPI$ ) values computed for all sites showed no strong spatial variation in the liquefaction susceptibility of Qts. This finding is different from the conclusion of Heidari and Andrus (2012) using fewer sites many of which were targeted liquefaction.

Liquefaction potential of Qts was evaluated in terms of liquefaction probability curves, expressed as a function of  $a_{max}/MR$  and a weighted  $LPI$  threshold at which surface manifestations of liquefaction occur. Several probability curves were developed for different depths to the top of Cooper Marl and groundwater table combinations. It was observed that liquefaction potential decreases as depth to the groundwater table increases for a given depth to Cooper Marl.

Without a correction for the influence of diagenesis ( $K_{DR}$ ), liquefaction potential within 15 km of the Woodstock fault where some surface manifestations of liquefaction occurred during the 1886 Charleston earthquake was over predicted. However, predicted liquefaction was consistent with observed ground behavior when the  $MEVR$ -based  $K_{DR}$  correction factors were applied. The average back-calculated  $K_{DR}$  for Qts is within the scatter of the published data.

## APPENDIX F

### LIQUEFACTION PROBABILITY CURVES FOR THREE SURFICIAL SAND DEPOSITS NEAR CHARLESTON, SOUTH CAROLINA<sup>3</sup>

**Joshua D. Gathro<sup>1</sup>, Barnabas Bwambale<sup>2</sup>, Ronald D. Andrus<sup>3</sup>, and Tahereh Heidari<sup>4</sup>**

<sup>1</sup>Glenn Department of Civil Engineering, Clemson University, P.O. Box 340911, Clemson, SC 29634-0911; e-mail: jgathro@clemson.edu

<sup>2</sup>Glenn Department of Civil Engineering, Clemson University, P.O. Box 340911, Clemson, SC 29634-0911; e-mail: bbwamba@clemson.edu

<sup>3</sup>Glenn Department of Civil Engineering, Clemson University, P.O. Box 340911, Clemson, SC 29634-0911; e-mail: randrus@clemson.edu

<sup>4</sup>CH2M, 2020 SW Fourth Avenue, Suite 300, Portland, OR 97201-4973; e-mail: maddie.heidari@ch2m.com

#### Abstract

Liquefaction probability curves for three Quaternary sand deposits near Charleston, South Carolina are derived in this paper. The derivation is based on seismic cone penetration test profiles for 33 sites in the Holocene beach to barrier-island deposits (Qhs); 24 sites in the 33,000- to 85,000-year-old Silver Bluff terrace (Qsbs); and 91 sites in the 70,000- to 130,000-year-old Wando Formation (Qws). Liquefaction potential is expressed in terms of the liquefaction potential index (*LPI*). The effect of aging processes on liquefaction potential is considered through a correction factor based on the ratio of measured shear-wave velocity ( $V_s$ ) to estimated  $V_s$ . The liquefaction probability curves are expressed as functions of peak ground acceleration, magnitude, and probability that *LPI* is greater than or equal to a threshold value for surface manifestation of liquefaction at level ground sites. The results indicate that Qhs exhibits the highest probability for a given level of ground shaking, followed by Qsbs and then Qws.

---

<sup>3</sup> This appendix is included as a publication that was supported by USGS Grant No. G16AP00118. Gathro, J. D., Bwambale, B., Andrus, R. D., Heidari, T. (2018). "Liquefaction probability curves for three surficial sand deposits near Charleston, South Carolina." *5th Geotechnical Earthquake Engineering and Soil Dynamics Conference*, Austin, TX, June 10-13.

## **F.1 Introduction**

The 1886 Charleston, South Carolina earthquake (moment magnitude,  $M_w \sim 7.0$ ) is the largest historic seismic event to have occurred in the eastern United States (Bollinger 1977). Ground shaking was felt over 800 miles away (Nuttli et al. 1986), and damage to infrastructure and homes was equivalent to \$460 million (2006 dollars, Côté 2006). A significant portion of the damage was due to liquefaction-induced ground failure in the Charleston region (Dutton 1889).

A map of the Charleston area is presented in Figure F-1. Included on the map are: 1) the likely source of the 1886 earthquake (Woodstock fault zone), 2) spatial distributions of seven Quaternary beach to barrier island sand deposits, 3) locations of selected 1886 earthquake observed ground behavior in three surficial deposits, and 4) locations of 148 seismic cone penetration tests (designated as SCPT if no pore pressure measurements were made and SCPTu if pore pressure measurements were made) conducted in these three deposits. This number of cone penetration tests is over three times the number Heidari and Andrus (2012) used to characterize the liquefaction probability of these three deposits. The purpose of this paper is to update and verify the liquefaction probability curves for the three deposits using the expanded SCPT dataset.

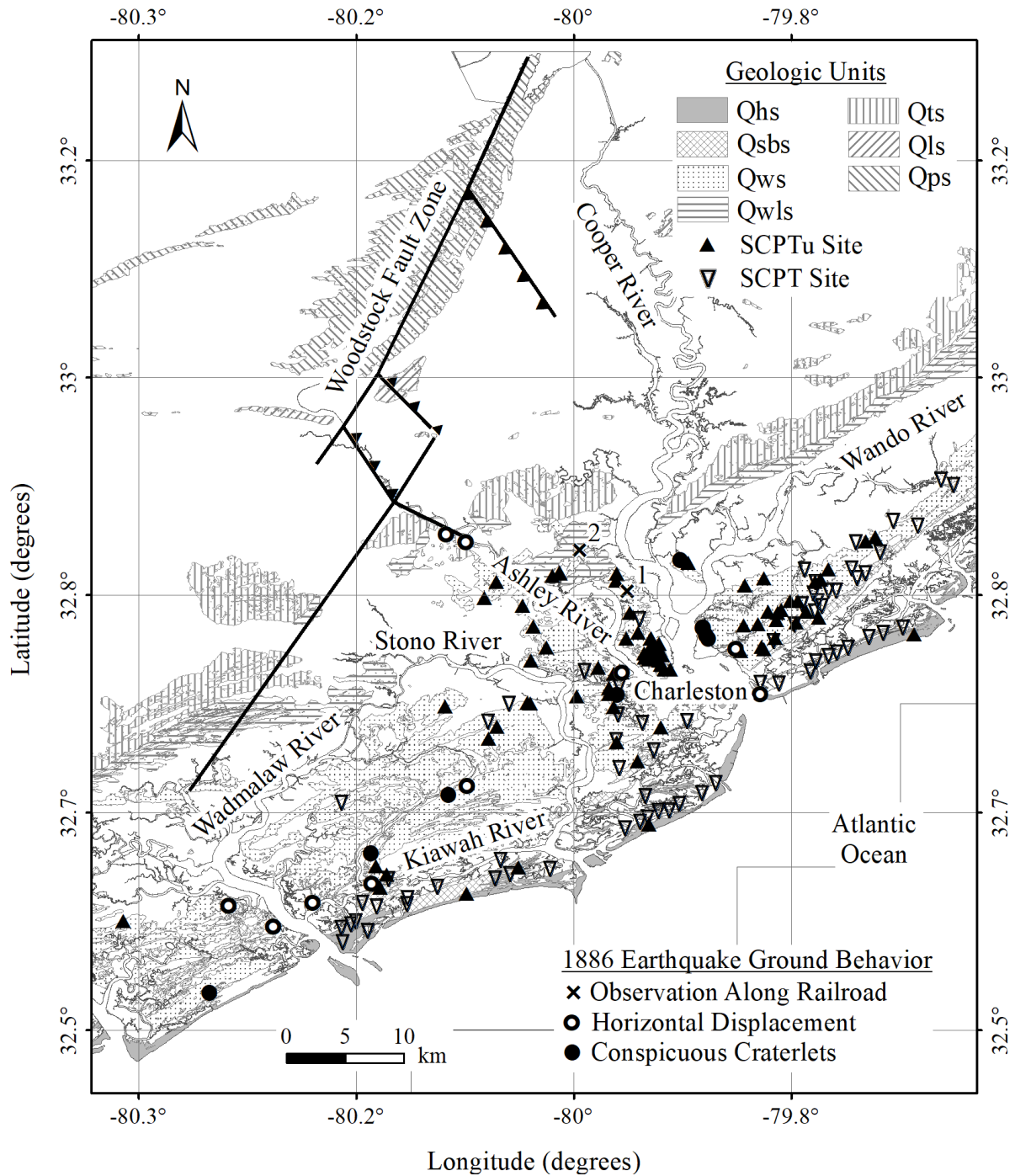


Figure F-1. Map of the Charleston area showing surficial sand deposits (modified from Heidari and Andrus 2012), the Woodstock fault zone (Durá-Gómez and Talwani 2009), mapped sites of ground failures within Qhs, Qsbs and Qws (Dutton 1889, PLs. XXVII & XXVIII; Peters and Hermann 1986), and seismic cone penetration test sites within these three units.



## **F.2 Geology and Seismology**

The Charleston area lies within the lower Coastal Plain physiographic province. The region is generally blanketed with thick Quaternary sediments of sand and clay deposited atop older, Neogene to Paleogene (2.6–66 Ma) stratigraphic units. A dominant Paleogene unit in the subsurface is the Ashley Formation of the Cooper Group, a phosphatic and quartzose calcarenite locally known as the Cooper Marl. The Cooper Marl is generally considered nonsusceptible to liquefaction (Li et al. 2007; Hayati and Andrus 2008). The unconsolidated sedimentary sequences rest on crystalline basement rock, known to be ~800 m below ground surface (Chapman and Talwani 2002).

The youngest three natural sand deposits are: Qhs, Qsbs, and Qws. Qhs is a deposit of Holocene (< 10 ka) beach to barrier-island quartz sand, located in the low-lying region parallel to the coast. Qsbs (33–85 ka) is a beach to barrier-island quartz sand known as the Silver Bluff terrace, often deposited adjacent to Qws. Qws (70–130 ka) is a barrier-island quartz sand facies of the Wando Formation.

As discussed by Durá-Gómez and Talwani (2009), the Woodstock fault is characterized as a right-lateral strike-slip fault oriented N30°E, dipping  $\geq 50^\circ$  northwest. The fault trace was inferred from macroscopic observations, as well as an analysis of instrumentally recorded seismicity (1974–2004) and geomorphic studies of displaced river channels.

Dutton (1889) reported several cases of ground failure that occurred during the 1886 earthquake. The number of mapped occurrences of horizontal displacement were 1, 7, and 3 within Qhs, Qsbs and Qws, respectively; and the number of mapped areas of conspicuous craterlets were 0, 5, and 2, respectively. These observations generally agree with newspaper and other accounts compiled by Hayati and Andrus (2009) and Heidari and Andrus (2010), as well as the field notes by Earl Sloan along the railway lines summarized in Table E-1. Assuming that the field notes by Earl Sloan accurately describe all significant ground behavior, about 10% of the area along the railway lines through Qws experienced moderate to severe liquefaction, 2% experienced minor, and 88% experienced none. Areas within a radius of 80 m from observed craterlets are classified as moderate to severe liquefaction. Areas are classified as minor if fissures and depressions were present within a radius of 80 m, and none if there were no disturbances along the railway lines.

Table F-1. Ground behavior in Qws along railroads during the 1886 Charleston earthquake (adapted from field notes by Earl Sloan and W. J. McGee as cited by Dutton [1889, pp. 283-294, 303-306] and Peters and Hermann [1986, pp. 18-26, 51-55, 62-64]).

Site No.	Surface Geology	Mile Point	Latitude (degrees)	Longitude (degrees)	Elev. (m)	Description of Disturbance
South Carolina Railroad						
1	Qws	3.57	32.835994	-79.959171	4.42	Curve disturbed, several joints well opened; occasional craterlets to mile point 5.0
Northeastern Railroad						
2	Qws	7.0	32.867467	-79.995433	-	Slight depression within short space over culvert
		7.02	32.867750	-79.995464	7.62	Slight sinuous flexure

### F.3 Seismic Cone Penetration Test Data

The 148 SCPT and SCPTu profiles are compiled from various available research and consulting reports. Of the 148 SCPT profiles, 33 plot in Qhs, 24 in Qsbs, and 91 in Qws. Displayed in Figure F-2 is the SCPTu profile for the site designated as Qws85, located on the Charleston Peninsula. The tip resistance ( $q_t$ ), friction ratio ( $FR$ ), and pore water pressure ( $u_2$ ) measurements are shown in Figures F-2a, F-2b and F-2c, respectively. These measurements help distinguish soil behavior type. Typical behavior for sand-like soil includes high  $q_t$  and low  $FR$ , with  $u_2$  approximately equal to the hydrostatic pressure ( $u_0$ ). Clay-like soil alternatively exhibits low  $q_t$  and high  $FR$ , with increased values of excess  $u_2$  as a result of soil remolding and undrained conditions. The increase in shear-wave velocity ( $V_s$ ) to over 300 m/s below 17 m in Figure F-2d is typical of the Cooper Marl. The fairly uniform profiles of  $q_t$ , and  $FR$ , and  $u_2 > 1$  MPa are also typical of the Cooper Marl.

Downhole seismic cone data are often evaluated by means of the direct method or the interval method, where the wave path is assumed to follow a straight line from source to receiver. While the assumption of straight ray path simplifies the calculation, it overlooks the effects of refraction at soil layer boundaries with contrasts in soil stiffness, which may yield a measured  $V_s$  greater or less than the true  $V_s$ . This issue is of greatest concern near the ground surface, where the assumed straight ray path may vary significantly from the true path, depending on the magnitude of horizontal source offset, downhole interval and variation in soil stiffness. Measured  $V_s$  from downhole data can be improved by using the Snell's Law ray path method (Kim et al. 2004). The seismic data utilized in this study have been re-evaluated by means of the Snell's Law ray path method where complete metadata were accessible. For sites with insufficient metadata (< 4% of the sites),  $V_s$  values were used as provided in the geotechnical reports.

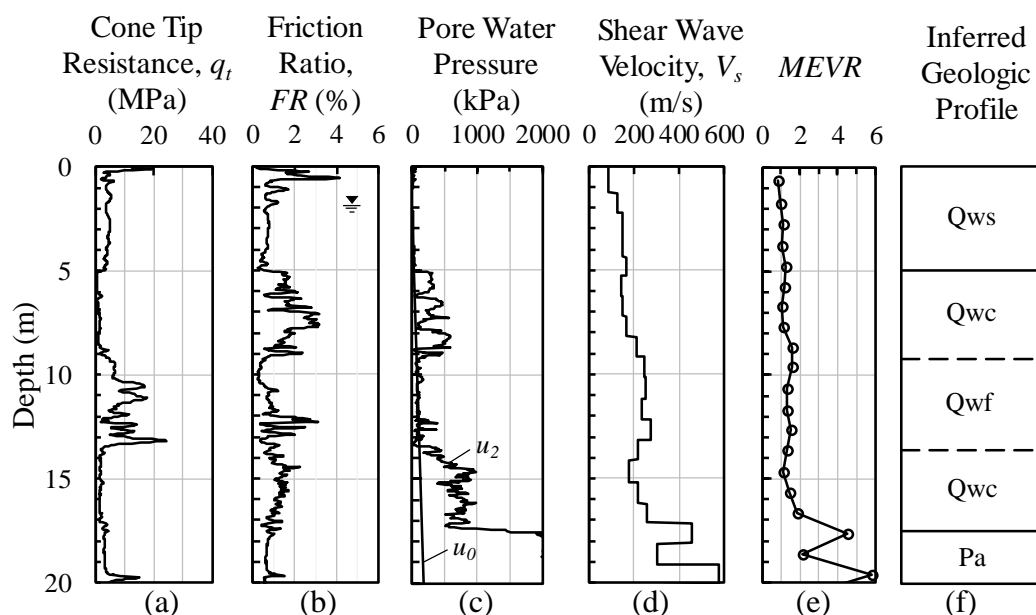


Figure F-2. SCPTu profile and inferred geologic profile for Site Qws85. The inferred geologic profile is based on the SCPTu profile and information available on the USGS Charleston quadrangle geologic map by Weems and Lemon (1993).

#### **F.4 Measured To Estimated Shear Wave Velocity**

The ratio of measured  $V_s$  to estimated  $V_s$  ( $MEVR$ ) is a promising index for quantifying the effects of aging processes on microstructure. Andrus et al. (2009) proposed estimating  $V_s$  based on a  $q_t - V_s$  relationship for uncemented sand deposits that are ~6 years old, which is defined as:

$$V_{s1cs} = 62.6(q_{t1N,cs})^{0.231} \quad (1)$$

where  $V_{s1cs}$  = overburden stress-corrected clean sand-equivalent shear wave velocity;  $q_{t1N,cs}$  = overburden stress-corrected clean sand-equivalent cone tip resistance. Shown in Figure F-2e is the variation in  $MEVR$  versus depth. The plotted values of  $MEVR$  represent the average value over an interval corresponding to the  $V_s$  measurement interval. Plotted values of  $MEVR$  in Figure F-2e increase from around 1.0 near the ground surface to 1.5 at a depth of 16 m. Below 17 m,  $MEVR$  values increase above 2.0, which is typical of the Cooper Marl.

Figure F-3 presents composite plots of  $MEVR$  with depth for the three sand deposits. Values closer to the ground surface show a tighter range, particularly for Qhs and Qsbs, suggesting a lower degree of diagenesis and/or disturbance from strong ground motion during the 1886 earthquake.  $MEVR$  values at depth increase from around 1.0 to over 6.0, suggesting stiffer soil structure.

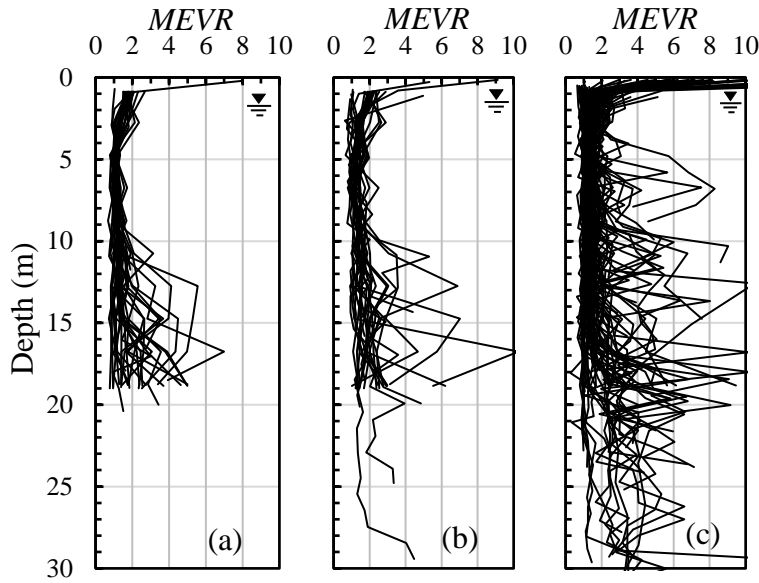


Figure F-3. Composite  $MEVR$  profiles for (a) Qhs, (b) Qsbs, and (c) Qws. Depicted groundwater levels represent average depths within deposits.

#### **F.5 Liquefaction Potential Analysis**

The liquefaction potential index ( $LPI$ ) is used to characterize liquefaction potential at the SCPT and SCPTu sites.  $LPI$  is defined as (Iwasaki et al. 1978):

$$LPI = \int_0^{20m} F \bullet w(z) dz \quad (2)$$

where  $F = 1 - FS$  for  $FS \leq 1$  and 0 for  $FS > 1$  ( $FS$  is factor of safety against liquefaction triggering, defined as the cyclic resistance ratio divided by the cyclic stress ratio);  $z$  is depth below ground surface in meters; and  $w(z)$  is a depth weighting function.  $LPI$  therefore depends on the thickness of liquefiable layers in the top 20 m, their proximity to ground surface, and their associated  $FS$ .

Presented in Figure F-4 are the  $LPI$  calculations for Qws85 assuming peak ground acceleration ( $a_{max}$ ) = 0.25g,  $M_w = 7.0$ , and based on the liquefaction triggering procedure by Boulanger and Idriss (2016). Added to this procedure is the diagenesis correction factor ( $K_{DR}$ ) applied to the cyclic resistance ratio ( $CRR$ ), where  $K_{DR} = 1.08MEVR - 0.08$  (Hayati and Andrus 2009). Plotted in Figures F-4a and F-4b are profiles of normalized tip resistance ( $q_{t1N}$ ) and cone soil behavior type index ( $I_c$ ) versus depth, respectively. Layers with  $I_c > 2.6$  are considered nonsusceptible to liquefaction and are not considered in the calculations. Figure F-4d presents the calculated values of cyclic stress ratio ( $CSR$ ) and  $CRR$  versus depth, with both  $K_{DR} = 1.0$  and  $K_{DR} \neq 1.0$  ( $CRR_K$ ). Figure F-4f indicates that  $LPI$  based on  $K_{DR} = 1.0$  is 17, which incorrectly suggests a greater extent of liquefaction in Qws during the 1886 Charleston earthquake.

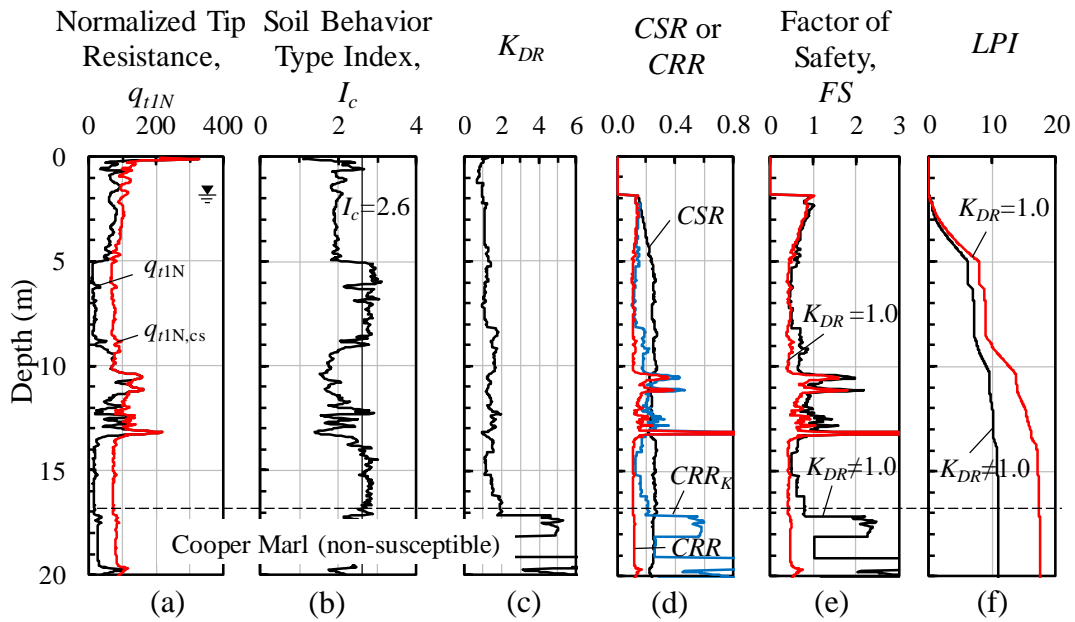


Figure F-4.  $LPI$  calculation for Site Qws85 assuming  $a_{max} = 0.25g$  and  $M_w = 7.0$ .

For the computed  $LPI$  to be considered in this study, SCPT profiles needed to extend to depths  $\geq 20$  m, extend into the nonsusceptible Cooper Marl, or terminate within 2 m (Qhs, Qws) or 3 m (Qsbs) above such depths based on available geologic maps. A 3-m standard for Qsbs was allowed because many of the sites within this unit would otherwise be eliminated. Where cone soundings were terminated 2-3 m above 20 m or Marl, the remaining profile was assumed to be the same as the last 2-3 m. Some profiles were removed from  $LPI$  calculations due to limitations such as:  $V_s$  measurements covering an interval  $> 4$  m; uncertainty in  $u_2$  baseline values; excessive data points with negative sleeve friction; and failure to achieve sufficient test depth. These criteria resulted in a reduced number of sites used in  $LPI$  calculations, providing 30, 22, and 82 profiles for Qhs, Qsbs, and Qws, respectively.

## F.6 Liquefaction Susceptibility Assessment

Overall liquefaction susceptibility is evaluated using  $LPI$ , assuming a constant earthquake loading of  $a_{max} = 0.25g$  and  $M_w = 7.0$ . Although  $a_{max}$  would vary during a seismic event as a function of distance from source, the assumption of  $a_{max} = 0.25g$  is made in order to assess relative susceptibility across the three sand units, including the influence of distance from Woodstock fault ( $d_f$ ). The  $LPI$  results for the constant earthquake loading are presented in Figure F-5.

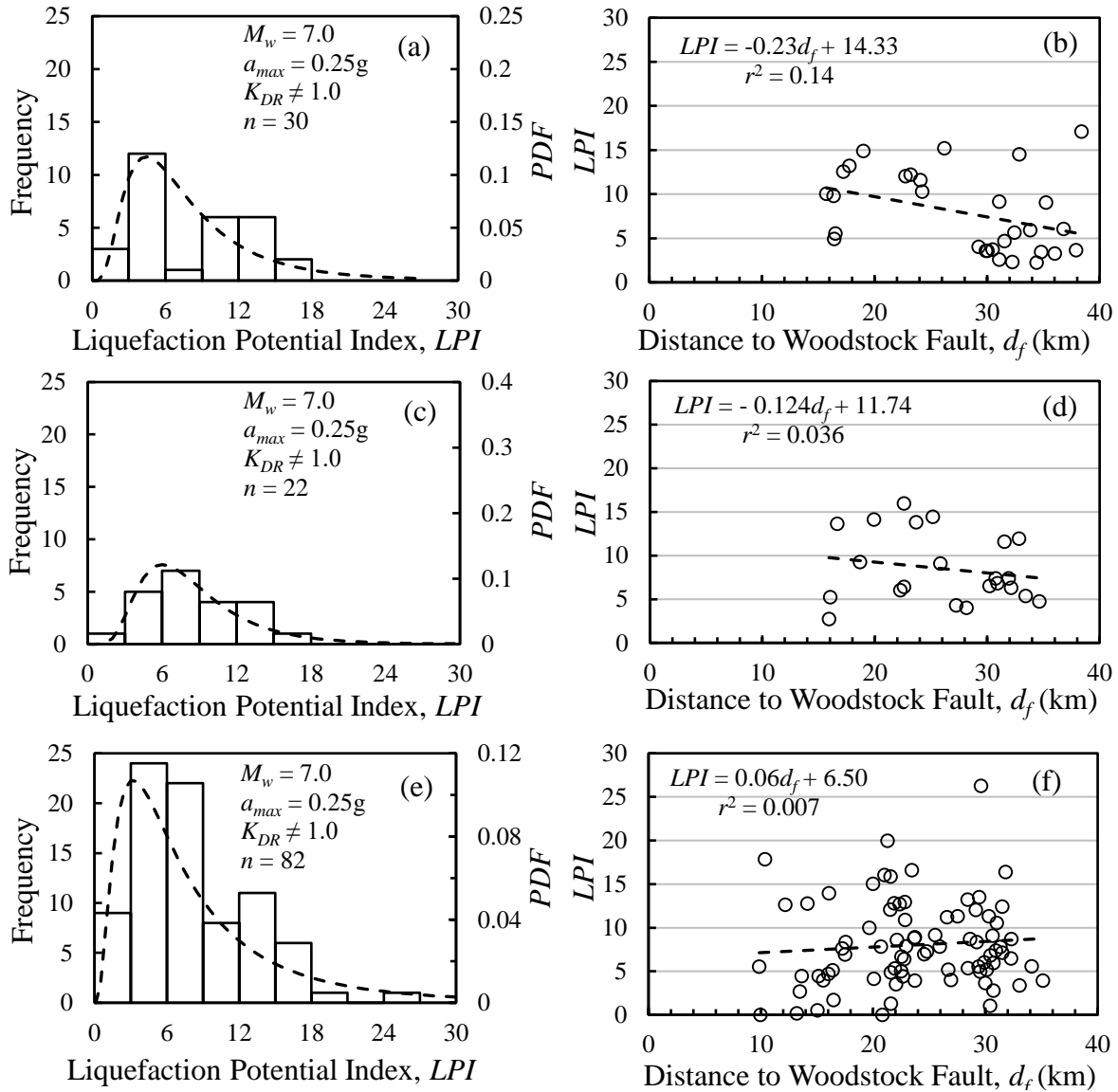


Figure F-5. Probability density function (PDF) and  $LPI$  histogram for (a) Qhs, (c) Qsbs, and (e) Qws. Plot of  $LPI$  versus distance to Woodstock fault for (b) Qhs, (d) Qsbs, and (f) Qws.

Presented in Figures F-5a, F-5c, and F-5e are histograms and probability density functions (PDF) for the computed  $LPI$  values of Qhs, Qsbs, and Qws, respectively, assuming lognormal

distribution and based on constant earthquake loading. The three histograms show greatest frequency for  $LPI$  values between 3 and 15, with right-skewed distributions. The  $PDF$  curves also indicate a slightly higher average  $LPI$  for Qsbs, although the distributions are fairly similar among all three units.

Presented in Figures F-5b, F-5d, and F-5f is the relationship between  $LPI$  and  $d_f$  for Qhs, Qsbs, and Qws, respectively. Heidari and Andrus (2012) suggested that a closer proximity to the seismic source may yield lower  $MEVR$  as a result of increased ground shaking from previous seismicity. However, the plotted data suggest little correlation between distance from Woodstock fault and  $LPI$  for the range of  $d_f$ . This difference in findings may be attributed to the augmented database now included. The overall susceptibility across units appears to be similar.

Presented in Figures F-6a and F-6b are respectively cumulative distribution function ( $CDF$ ) curves and box plots for Qhs, Qsbs, and Qws based on calculated values of  $LPI$ . Figure F-6a shows that all three units have similar  $LPI$ - $CDF$  relationships under the same earthquake loading (i.e.,  $a_{max} = 0.25g$ , and  $M_w = 7.0$ ). The distributions are assumed to be lognormal. Figure F-6b illustrates the range of data obtained in this analysis for each unit. Overall the three units have common ranges, with Qws having the greatest spread of  $LPI$  values. Mean  $LPI$  values are also very similar across units, 7.9 for Qhs, 8.2 for Qsbs, and 7.8 (outlier omitted) for Qws. While each site is grouped based on surface geology, underlying deposits have been formed by and subjected to common geologic processes, which may contribute similarly to liquefaction susceptibility.

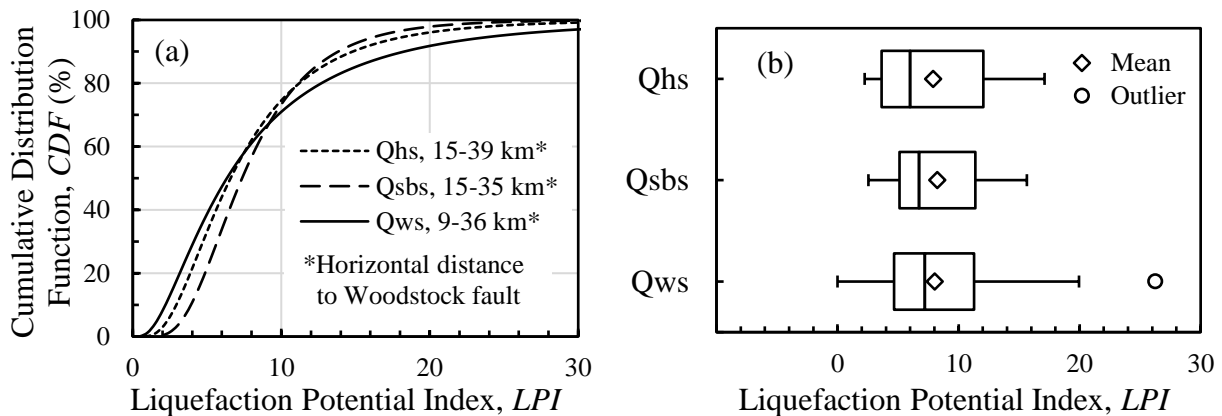


Figure F-6. (a)  $CDF$  curves for  $LPI$  values of Qhs, Qsbs, and Qws, and (b) box and whiskers plots of  $LPI$  values calculated for these units assuming constant earthquake loading.

### **F.7 Liquefaction Probability Curves**

Shown in Figure F-7 are liquefaction probability curves for Qhs, Qsbs, and Qws based on results of  $LPI$  calculations performed on the SCPT profiles by varying  $a_{max}$  between 0.1 and 0.7 g and  $M_w$  between 5 and 9, and assuming the results are lognormally distributed. The basis of the probability curves is derived from the methodology proposed by Holzer et al. (2006) and Rix and Romero-Hudock (2007), with two modifications. First, in place of magnitude scaling factor ( $MSF$ ), the probability curves are constructed from pairs of  $a_{max}$  and magnitude ratio ( $MR$ ), where  $MR = 7.5/M_w$ .  $MR$  is used due to the depth dependence of the  $MSF$  relationship in the Boulanger

and Idriss (2016) procedure. The interval of  $a_{max}$  used is 0.02g between 0.1g and 0.3g, and 0.1g from 0.3g to 0.7g. The interval of  $M_w$  is every 0.5.

The second modification involves the assumed  $LPI$  threshold ( $LPI_t$ ) separating no to minor from moderate to severe surface manifestations of liquefaction. Holzer et al. (2006) and Rix and Romero-Hudock (2007) assumed  $LPI_t = 5$ . Maurer et al. (2015) studied the relationship between surface manifestation of liquefaction and average cone soil behavior type index in the top 10 m ( $I_{c10}$ ) at over 7,000 sites in Christchurch, New Zealand, and found that  $LPI_t = 6$  for sites with  $I_{c10} < 2.05$  and  $LPI_t = 15.5$  for sites with  $I_{c10} \geq 2.05$ . The  $I_{c10}$  values computed for the Charleston area vary greatly within a surface geology and are often well distributed across the  $I_{c10} = 2.05$  boundary. Thus, to better match observed ground behavior, a weighted  $LPI_t$  is used for each unit (i.e., 9 for Qhs, 14 for Qsbs, 13 for Qws).

The probability curves presented in Figure F-7 are defined by:

$$P_{LPI \geq LPI_t} = 1 / (1 + [(a_{max} / MR) / a]^b) \quad (3)$$

where  $a$  and  $b$  are curve-fitting variables. The values of  $(a, b)$  are equal to (0.260, -7.147), (0.314, -7.383), and (0.323, -5.560) for Qhs, Qsbs, and Qws, respectively.

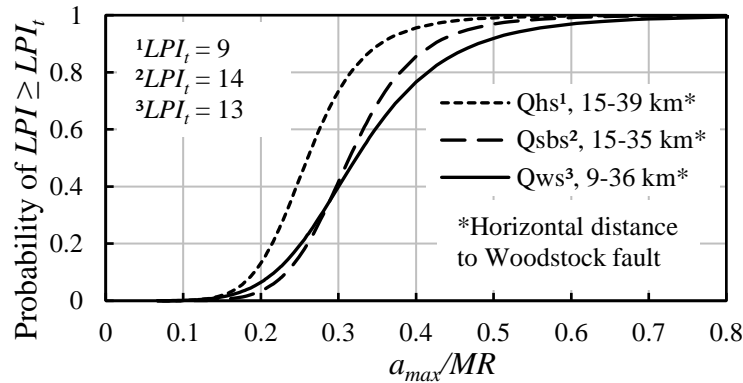


Figure F-7. Liquefaction probability curves for Qhs, Qsbs, and Qws.

## **F.8 Conclusion**

The liquefaction susceptibility of three surficial sand deposits in the Charleston area was characterized using 134 SCPT profiles from sites located 9 to 39 km from the Woodstock fault and assuming a constant level of ground shaking. Computed  $LPI$  values exhibited little to no correlation with distance to the fault. Cumulative distributions of  $LPI$  values for a given shaking level are similar for all three units. Liquefaction probability curves were expressed as a function of  $a_{max}/MR$  and a weighted threshold  $LPI$  at which surface manifestations occur. Qhs exhibited the highest probability of liquefaction, and Qws exhibited the lowest probability. The probability curves may be used to create regional hazard maps, but should not replace site-specific evaluations.

## **F.9 Acknowledgments**

The authors thank the United States Geological Survey (USGS), Department of the Interior, who provided support under Grant No. G16AP00118. The views and conclusions contained in this document are those of the writers and should not be interpreted as necessarily representing the official policies, either expressed or implied, of the United States Government. The authors also thank Billy Camp and Kyle Murrell of S&ME, Inc., Matthew Silveston of Terracon, and Michael Cox of Palmetto In-Situ for their generous assistance with data collection.

## **F.10 References**

- Andrus, R. D., Hayati, H., and Mohanan, N. P. (2009). "Correcting liquefaction resistance for aged sands using measured to estimated velocity ratio." *J. Geotech. and Geoenviron. Eng.*, 135(6), 735–744.
- Bollinger, G. (1977). "Reinterpretation of the intensity data for the 1886 Charleston, South Carolina, earthquake." *Studies Related to the Charleston, South Carolina, Earthquake of 1886: A Preliminary Rep.*, D. W. Rankin, ed., USGS Professional Paper 1028, U.S. Government Printing Office, Washington, DC, 17–32.
- Boulanger, R. W., and Idriss, I. M. (2016). "CPT-based liquefaction triggering procedure." *J. Geotech. Geoenviron. Eng.*, 142(2).
- Chapman, M. C., and Talwani, P., (2002). "Seismic hazard mapping for bridge and highway design." Report to the South Carolina Department of Transportation, Columbia, SC.
- Côté, R. N. (2006). *City of Heroes: The Great Charleston Earthquake of 1886*, Corinthian Books, Mt. Pleasant, SC, 542 p.
- Durá-Gómez, I., and Talwani, P. (2009). "Finding faults in the Charleston area, South Carolina: 1. Seismological data." *Seismol. Research Letters*, 80(5), 883–900.
- Dutton, C. E., (1889). "The Charleston earthquake of August 31, 1886." *Ninth Annual Report of the U.S. Geological Survey 1887-1888*, Washington, D.C., 203-528.
- Hayati, H., and Andrus, R. D. (2008). "Liquefaction potential map of Charleston, South Carolina based on the 1886 earthquake." *J. Geotech. and Geoenviron. Eng.*, 134(6), 815–828.
- Hayati, H., and Andrus, R. D. (2009). "Updated liquefaction resistance correction factors for aged sands." *J. Geotech. and Geoenviron. Eng.*, 135(11), 1683–1692.
- Heidari, T., and Andrus, R. D. (2010). "Mapping Liquefaction Potential of Aged Soil Deposits in Mount Pleasant, South Carolina." *Engineering Geology*, 112(1-4), 1- 12.
- Heidari, T., and Andrus, R. D. (2012). "Liquefaction potential assessment of Pleistocene beach sands near Charleston, South Carolina." *J. Geotech. and Geoenviron. Eng.*, 138(10), 1196-1208.
- Holzer, T. L., Bennett, M. J., Noce, T. E., Padovani, A. C., and Tinsley, J. C. (2006). "Liquefaction hazard mapping with LPI in the greater Oakland, California, area." *Earthquake Spectra*, 22(3), 693–708.
- Iwasaki, T., Tatsuoka, F., Tokida, K.-I., and Yasuda, S. (1978). "A practical method for assessing soil liquefaction potential based on case studies at various sites in Japan." *Proc., 2nd Int. Conf. Microzonation*, National Science Foundation, Washington, DC, 885–896.
- Kim, D. S., Bang, E. S. and Kim, W. C. (2004). "Evaluation of various downhole data reduction methods for obtaining reliable Vs profiles." *Geotechnical Testing Journal*, 27(6), 585–597.



- Li, D. K., Juang, C. H., Andrus, R. D., and Camp, W. M. (2007). "Index properties-based criteria for liquefaction susceptibility of clayey soils: a critical assessment." *J. Geotech. and Geoenviron. Eng.*, 133(1), 110–115.
- Maurer, B. W., Green, R., Cubrinovski, M., and Bradley, B. A. (2015). "Fines-content on liquefaction hazard evaluation in Christchurch, New Zealand." *Soil Dynamics and Earthquake Engineering*, 76: 58-68.
- Nuttli, O. W., Bollinger, G. A., and Herrmann, R. B. (1986). "The 1886 Charleston earthquake—A 1986 perspective." Circular 985, U.S. Geological Survey, Washington, D.C.
- Peters, K. E., and Herrmann, R. B., editors, (1986). *First-Hand Observations of the Charleston Earthquake of August 31, 1886, and other Earthquake Materials, Bulletin 41 of the South Carolina Geological Survey*, Columbia, SC
- Rix, G. J., and Romero-Hudock, S. (2007). "Liquefaction potential mapping in Memphis and Shelby County, Tennessee." Rep. to the U. S. Geological Survey, Denver, CO.
- Weems, R. E., Lemon Jr, E. M., (1993). "Geology of the Cainhoy, Charleston, Fort Moultrie, and North Charleston quadrangles, Charleston and Berkley Counties, South Carolina." *USGS Open-file Report 97-531*. U.S. Geological Survey, Reston, VA.

## **APPENDIX G**

### **DATA SUPPLEMENT**

An electronic data supplement has been prepared and is available from the authors upon request. This data supplement includes cone penetration test data from each site used in the analysis of the six sand units and five clayey units. Also included in the supplement are summary tables of shear wave velocity for each site, providing recorded travel times and interval depths. Within each file, additional metadata is included to provide select details on the project number, location, and site-specific notes.